

Akita University Doctoral Dissertation

**THE EVOLUTION OF MAGMA PLUMBING SYSTEM IN TANGKIL
AND RAJABASA VOLCANOES, INDONESIA**

HASIBUAN, REZA FIRMANSYAH



The evolution of magma plumbing system in Tangkil and Rajabasa volcanoes, Indonesia

A graduate thesis presented for the degree of Doctor of Philosophy

By

Reza Firmansyah Hasibuan

Student ID No. 6517103

Department of Geoscience, Geotechnology, and Material Resource Engineering

資源学

Graduate School of International Resource Sciences

国際資源学

Akita University

秋田大学

2020

Declaration

No part of this dissertation has been submitted beforehand for a degree at any other University. Works included in this dissertation is utterly that of the author, results of study done in Akita University, except where due reference is made in the text to published or unpublished works.

ABSTRACT

Tangkil and Rajabasa volcanoes are neighboring subduction-zone volcanoes located within Sunda volcanic arc on the southeast tip of Sumatra Island, Lampung Province, Indonesia. These volcanoes are situated in the Sunda Strait, where Panaitan Island, Krakatau Island, Sebesi and Sebuku Islands, and the Sukadana basalt plateau form a volcanic lineament. This region is unique in term of its tectonic and volcanic activity.

Tangkil and Rajabasa volcanoes are not well studied compared to other volcanoes in Sunda Strait. The age determination and geochemical analyses of volcanic rocks from the two volcanoes have not been conducted. Detailed observation on mineral textures and zoning patterns, which could reflect the magmatic history for some extents, also has not been done. These data can give a valuable information about volcanic history and evolution of magma plumbing system. Thus, these reasons provide a good opportunity to study Tangkil and Rajabasa volcanoes.

This study introduces a new stratigraphy of lavas, radiometric ages, whole-rock chemistry, detailed observation on mineral textures and zoning, and a new set of mineral chemistry data. Stratigraphic correlation of lavas in the Tangkil-Rajabasa volcanic area is established from field observations, morphological analysis, and K-Ar dating analyses. Detailed petrography and geochemical data of 13 lava units are then integrated with the stratigraphy to show temporal petrological variations. The description of petrological variations by a careful observation on mineral textures, compositional zoning patterns, and mineral assemblages, helps to identify the magmatic processes. The endmember magmas are identified via whole-rock and mineral chemistry, and their *T-P* conditions are estimated using thermobarometry models.

Early stage (> 4.3 Ma) effusives of Tangkil volcano are dacitic to rhyolitic (67-71 wt% SiO₂; Tklf), whereas later (c. 4.3 Ma) rocks are basaltic to basaltic andesite (c. 52 wt% SiO₂; TkIm). Then, it took c. 4.0 Ma to resume volcanic activity at Rajabasa volcano. Lavas of Rajabasa volcano are comparatively younger (c. 0.3 to 0.1 Ma) with composition ranging from basalt to andesite (51-62 wt% SiO₂; Rbs).

The rocks from Tangkil (last Tklf) and most Rajabasa (all Rbs, except for one sample) indicate open system processes. These rocks contain plagioclase and pyroxene phenocrysts that show chemically evolved cores with resorption textures and less evolved mantles or rims. The resorption textures can be formed by processes of heating, hydration, compositional change of ambient magma, or decompression. The multiple zones of dissolution-overgrowth in plagioclase crystal and the fluctuating trend in temporal whole-rock variation suggest that the changes of magmatic condition in T, H₂O, or chemical composition were repetitive.

The chemical variations of Rajabasa are accounted for by the interactions of at least three endmembers: Mg-rich medium-K basalt magma, low-Mg medium-K basalt magma, and high-K andesitic magma. Mg-rich medium-K basalt magma is a primitive magma with high contents of Cr (>250 ppm) and Ni (>114 ppm). The mixing of basalt magmas with andesite magma is indicated by two linear trends in whole-rock chemistry diagrams and supported by chemical modelling performed using MELTS. The felsic endmember magma of Rajabasa is fixed in composition (at ~62 wt% SiO₂; ~2.2 wt% MgO). Tangkil also involves bimodal magma system of basalt and felsic magma. Although the majority of samples from Tangkil do not show evidence of open system magmatic processes, one sample (last Tklf) contain phenocrysts that show disequilibrium features.

The origin of the phenocrysts is determined by core-rim compositional variations of the phenocrysts. Tangkil is divided into series of Tklf, last Tklf, and Tkml; Rajabasa is divided into series of high-Mg basaltic andesite, low-Mg basaltic andesite, andesite, and transitional basalt based on geochemical characteristics. The assemblages of early-formed crystals in an endmember magma are established by finding the mutual chemical equilibrium between series. In accordance with the bulk geochemical results, the compositional variations of phenocrysts in last Tklf, high-Mg basaltic andesite, low-Mg basaltic andesite, and andesite series suggest contributions of various endmember magmas.

The multiple crystallization origins of phenocrysts are also indicated by the variations in T - P estimates obtained by thermobarometry calculation. The last Tklf series shows a distinct of T estimates (934 and 1069 °C), of which the lower temperature is similar with that of Tklf series. The series of high-Mg basalt, low-Mg basalt, and andesite also exhibit a wide range of T within series, but the T estimate of high-Mg basalt magma is averagely higher (1174 °C) than that of low-Mg basalt magma (972 °C) and andesite magma (932 °C). The magma storage region depths beneath Tangkil and Rajabasa are 11 km to 22 km, at mid- to low-crustal levels, whereas high-Mg basalt magma resided in crustal-mantle interface level (*c.* 25 km).

The magmatism in Tangkil was initially sourced from rhyolite magma at mid-crustal level. At later stage, a deeper and hotter basalt magma injected and mixed with the rhyolite magma. Ascent of another unmixed basalt magma occurred at *c.* 4.33 Ma, close before Tangkil volcano ceased its activity. The magmatism in Rajabasa during Upper Pliocene (*c.* 0.3 to 0.1 Ma) was originated from four distinct magmas. During its evolution, the upper mantle-origin high-Mg basalt magma and lower crust-origin low-Mg basalt magma repetitively replenished the middle crust-origin andesite magma. At one occasion, though, a basalt magma ascent and did not mix with the other three magmas.

Keywords: Rajabasa volcano; Tangkil volcano; Sunda Strait; temporal variation; repeating magma recharge; magma evolution; geothermometry.

ACKNOWLEDGEMENTS

I express my sincere gratitude to people who have helped me to finish this dissertation. Firstly, I owe my gratitude to my supervisor, Professor Tsukasa Ohba, who patiently provided continuous supervision and direction with the project, allotting his time for many discussions with me. A significant appreciation is reserved for Dr. Takashi Hoshide who continuously helped me at various stages during my study in Akita, especially his assistance for the operation of XRF and EPMA analysis. Yumi Hayakawa of Akita University is thanked for her continuous technical support. Special thanks to Doctor Mirzam Abdurrachman and Professor Benyamin Sapiie at Institut Teknologi Bandung who supplied important materials and shared their knowledge about volcanoes in Sunda Arc. I am indebted to people from Cugung village, especially Mumu whose assistance made the field observation around Rajabasa safe and possible. I thank my friends from Ouchi Petrology Lab. for involving me in many random discussions about research and life and other friends in Akita who sometimes bring me out to the nature when I am tired with the research. I deeply dedicated this thesis to my Mum and Dad and other family members who always give me love, strength, and motivation.

This work was supported by Japan Society for the Promotion of Science (JSPS) leading program “New Frontier Leader Program for Rare-metals and Resources” of Akita University.

Akita, January 2020

Author,

Reza Firmansyah Hasibuan

TABLE OF CONTENTS

	Page
TITLE PAGE	
ABSTRACT	1
ACKNOWLEDGEMENTS	4
TABLE OF CONTENTS	5
TABLE OF FIGURES	8
LIST OF TABLES	13
CHAPTER I: INTRODUCTION	
1.1 GENERAL INTRODUCTION AND BACKGROUND	15
1.2 PREVIOUS STUDIES ON TANGKIL AND RAJABASA	17
1.3 THESIS AIMS AND OBJECTIVES	18
CHAPTER II: GEOLOGICAL BACKGROUND	
2.1 GEOTECTONIC SETTING	20
2.2 GEOLOGICAL BACKGROUND.....	23
CHAPTER III: SAMPLE SELECTION AND ANALYTICAL TECHNIQUES	
3.1 FIELD SURVEY AND SAMPLE SELECTION	27
3.2 ANALYTICAL TECHNIQUES.....	27
3.2.1 Morphological analysis	27
3.2.2 Microscopic analysis	28

3.2.3	K-Ar isotope dating	28
3.2.3.1	Sample preparation.....	29
3.2.3.2	Potassium analysis.....	29
3.2.3.3	Argon isotope analysis.....	29
3.2.4	X-Ray Fluorescence (XRF).....	30
3.2.5	Scanning Electron Microscope-Energy Dispersive Spectrometer (SEM-EDS)	31
3.2.6	Scanning Electron Microscope-Wavelength Dispersive Spectrometer (SEM-WDS)	31
3.3	INTENSIVE PARAMETERS CALCULATION METHODS	32
	<i>Thermobarometry calculation</i>	33
a)	<i>Plagioclase-hornblende thermobarometer</i>	33
b)	<i>Clinopyroxene-orthopyroxene (two pyroxene pairs) thermobarometer</i>	33
c)	<i>Clinopyroxene-melt thermobarometers</i>	34
d)	<i>Plagioclase-melt hygrometer</i>	34
	<i>Depth calculation</i>	35

CHAPTER IV: RESULT

4.1	GEOLOGY OF TANGKIL AND RAJABASA VOLCANOES	37
4.2	POTASSIUM-ARGON ANALYSIS.....	43
4.3	MAJOR AND TRACE ELEMENT VARIATIONS	43
4.4	TEMPORAL CHEMICAL VARIATIONS	53
4.5	PETROGRAPHY	55
4.5.1	Textures.....	55
	<i>Last Tklf, high-Mg basaltic andesite, low-Mg basaltic andesite, and andesite</i>	55
	<i>Tklf, Tkml, and transitional basalt</i>	62
4.5.2	Mineral chemistry.....	63
	<i>Plagioclase</i>	63
	<i>Pyroxenes</i>	69
	<i>Orthopyroxene mantled by clinopyroxene</i>	71

<i>Olivine</i>	72
<i>Spinel and Fe-Ti oxides</i>	73
<i>Groundmass</i>	74

CHAPTER V: DISCUSSION

5.1 THE VOLCANISM OF TANGKIL AND RAJABASA	76
5.2 OPEN SYSTEM MAGMATIC PROCESS	77
<i>Implications of mineral texture and zoning in plagioclase phenocrysts</i>	77
<i>Implications of mineral texture and zoning in pyroxene phenocrysts</i>	78
<i>Repetitive changes of T, H₂O, or chemical composition</i>	78
<i>Indication of magma mixing</i>	79
<i>Repeating recharges</i>	82
<i>Endmember magmas</i>	82
5.3 THE ORIGIN OF PHENOCRYSTS	86
5.4 MAGMA PLUMBING AND EVOLUTION SYSTEM.....	91

CHAPTER VI: SUMMARY AND CONCLUSIONS

SUMMARY AND CONCLUSIONS	97
-------------------------------	----

REFERENCES	99
-------------------------	-----------

APPENDICES	1111
-------------------------	-------------

TABLE OF FIGURES

<p>Figure 1. Map of the subduction-zone system in Indonesia (Gertisser and Keller, 2003b). Indo-Australian Oceanic Plate is subducting beneath Eurasian Continental Plate (6-7 cm/a). This activity results to magmatism (Sunda Arc), stretching from the Andaman Island to Banda Arc. Active volcanoes (o) and Sunda Strait (□) are shown in the map.22</p>	22
<p>Figure 2. A former geological map of volcanic rocks in southern Lampung, Sumatra by Andi Mangga et al. (1994).23</p>	23
<p>Figure 3. The ASTER image displaying Rajabasa volcano inside the caldera, as well as the NW trend of vents position from Tangkil to Rajabasa. The lower figure is the topographic cross section in this volcanic region, exhibiting the peaks.38</p>	38
<p>Figure 4. Geologic map displaying the distribution of Tangkil and Rajabasa unit lavas. The inset map shows the location of the volcanoes in Sunda Strait region. The labels (e.g. Rbs) indicate unit of lavas.40</p>	40
<p>Figure 5. Lava stratigraphy of Tangkil and Rajabasa volcanoes; B, Basalt; BA, Basaltic andesite; A, Andesite. The ages are shown for 3 lava units, in which Tangkil is an older volcano than Rajabasa. The crossed marks indicate the absence of data, caused by the difficult access, the intense alteration, or the volcanic products other than effusive lava flow or intrusion.41</p>	41
<p>Figure 6. Some representative outcrops in Tangkil (a, b, c) and Rajabasa (d, e) volcanoes.42</p>	42
<p>Figure 7. Rock classification using the scheme of Le Bas et al. (1986) based on total alkalis (Na₂O + K₂O wt%) vs silica (SiO₂ wt%) diagram for Tangkil and Rajabasa volcanic rocks. Except for Rbs 8, the majority of the rocks from Rajabasa plot in the basaltic andesite to andesite fields (circle), whereas rocks from Tangkil plot in two cluster ends (rectangle and triangle)44</p>	44

Figure 8. Phenocryst abundance variations in samples from Tangkil and Rajabasa volcanoes. Modal abundance of 0-5%, 5-10%, and 10-30% are indicated by symbol +, ++, and +++, respectively.....47

Figure 9. (above) Diagram of silica vs K_2O for the sub-division of the subalkaline series (Le Maitre et al., 1989). Rbs and Tklf rocks are plotted in transition from medium-K to high-K, whereas Tkml rocks plotted in medium-K. (below) A discriminating diagram between tholeiitic and calc-alkaline magma series. The separating line (heavy dashed line) is from Miyashiro (1974) which was later modified by Gill (2010).....49

Figure 10. Variation diagrams of SiO_2 (wt.%) vs. selected major and minor elements (ppm) for Tangkil and Rajabasa volcanic rocks.51

Figure 11. Tangkil and Rajabasa volcanic rocks plotted in K_2O vs MgO and Rb vs Cr . The diagrams display two discontinuous trends from Tangkil volcano, which are not parallel with Rajabasa trends. Meanwhile, Rajabasa volcano depicts two trends that converges from high-Mg and low-Mg basalt composition to andesitic composition.52

Figure 12. Temporal chemical variation of Tangkil and Rajabasa volcanic rocks. Total alkalis (Na_2O+K_2O) composition trend complies with silica (SiO_2), whereas CaO , MgO , and Al_2O_3 do not follow silica composition trend. All samples composition for each unit are plotted; continuous lines are running average from all sample in each unit to show the trend of the data.....54

Figure 13. Representative crossed polar microphotographs of: **A)** Euhedral phenocrysts of plagioclase, fresh amphibole, and pyroxene. **B)** Subhedral plagioclase containing cellular zones in the margin of crystals **C)** Plagioclase with complex zoning and iddingsite which altered olivine. **D)** An aggregate of plagioclase phenocrysts and discrete augite crystals. **E)** Orthopyroxene mantled by clinopyroxene rim. Melt inclusions developed in resorption boundary between the 2 phases. **F)** The phenocrysts assemblages in Rbs, containing spongy cellular or sieved plagioclase crystals (type 1) and “clear” plagioclase crystals (type 2).56

Figure 14. Back-scattered electron images of phenocrysts showing textures and compositional differences. **A)** Resorbed core with calcic-rich mantle (light shade) in plagioclase. **B)** The inner growth bands are dissected by calcic-rich plagioclase. **C)** Oscillatory (multiple) zoned plagioclase with transition between growth bands bound by calcic-rich and dissolution surfaces. Sieved zoned near the rim contains melt inclusions. **D)** Progressive normal zoning in clinopyroxene. **E)** Reverse step zoning in clinopyroxene. The transition is marked by abrupt increase in Mg# (rounded dark layer) in mantle. Core is embayed and slightly patchy. **F)** Orthopyroxene mantled by clinopyroxene rim. Darker shade in clinopyroxene reflect higher Mg#.....58

Figure 15. Step reverse zoning shown by plagioclase phenocryst from Rbs samples. Anhedral calcic-poor core (dark shade) mantled by calcic-rich (light shade) plagioclase.59

Figure 16. Multiple zones of dissolution-overgrowth in plagioclase crystals.60

Figure 17. Reverse (spectrum 1) and normal zoning (spectrum 2) exemplified by clinopyroxene phenocrysts in Rbs and last Tklf samples. In spectrum 1, 10 μm wide growth band at rim of crystal is identified, whereas in spectrum 2 c. 20 μm wide of high Mg in core of crystal. Line scan resolution is 512 x 384, map dwell 500 μs , and time/frame 98.3 s.61

Figure 18. An BSEI image showing bimodal compositions in plagioclase (a) and pyroxene (b) phenocrysts from last Tklf samples.65

Figure 19. An BSEI image showing crystal clots in Tklf samples. The clots contain plagioclase (An_{39-55}), enstatite (Mg_{66}), magnetite, and glass.65

Figure 20. Core-rim relationship of An-number [$100 \times \text{Ca}/(\text{Ca}+\text{Na})$] and Mg-number [$100 \times \text{Mg}/(\text{Mg}+\text{Fe})$] in plagioclase and pyroxene phenocrysts in Tangkil samples.....66

Figure 21. Profiles of electron microprobe traverse of plagioclase crystals from Tangkil. The compositions of An-number, TiO_2 , and $\text{FeO}^{(t)}$ are shown. The Tklf contain oscillatory zoning plagioclase with low amplitude.....67

Figure 22. Summary of textural and compositional characteristics in plagioclase crystals from all series.	68
Figure 23. Core-rim relationship of An-number $[100 \times \text{Ca}/(\text{Ca} + \text{Na})]$ and Mg-number $[100 \times \text{Mg}/(\text{Mg} + \text{Fe})]$ in plagioclase and pyroxene phenocrysts in Rajabasa samples. Symbol of triangle (Δ) is for more evolved sample from the series.	70
Figure 24. Core-rim relationship in Mg-number $[100 \times \text{Mg}/(\text{Mg} + \text{Fe})]$ for orthopyroxene mantled by clinopyroxene crystals from three different samples and series in Rajabasa. Orthopyroxene is mostly mantled by more magnesian clinopyroxene.	71
Figure 25. The crystals of orthopyroxene mantled by clinopyroxene as shown in BSEI images. The Mg-number compositional contrast is most evident in high-Mg basaltic andesite samples.	72
Figure 26. Compositional variation of Mg-number $[100 \times \text{Mg}/(\text{Mg} + \text{Fe})]$ vs NiO in olivine phenocrysts in Rajabasa samples. The olivine phenocrysts from high-Mg basaltic andesite are considerably higher in NiO contents compared to other series.	73
Figure 27. The compositions of olivine-hosted microphenocryst spinel in term of $\text{Cr}/(\text{Cr} + \text{Al})$ and their plot in olivine-spinel mantle array (Arai, 1994).	74
Figure 28. The mixing process is indicated by the two linear trends on K_2O vs MgO diagram. The change of magmatic activity from the two mafic endmembers is indicated by the shifting trend.	79
Figure 29. Phase relations of the low-Mg basalt endmember in T - P space calculated with MELTS.	80
Figure 30. Modelling of major elements fractional crystallization with MELTS presented on Harker diagrams for Rajabasa. The parameters used in calculation are described in the text. Lines of fractional crystallization with pressures of 1, 2, and 3 kbar are shown. Samples of 19.02a and I.8.01 were excluded from calculation.	81

- Figure 31.** Textural and compositional characteristics of plagioclase crystals from Tklm samples.....85
- Figure 32.** The schematic diagram of compositional relation between series in Rajabasa used for identification of endmember magmas composition.87
- Figure 33.** This schematic diagram shows resembling values of Mg-number $[100 \times \text{Mg}/(\text{Mg} + \text{Fe})]$ in olivine and pyroxene phenocrysts in Rajabasa samples. Cores of olivine in samples from high-Mg basaltic andesite, low-Mg basaltic andesite, and andesite can be equilibrated with the most magnesian clinopyroxene from the same series. Star symbols correspond to composition of pyroxene groundmass.89
- Figure 34.** The origin of phenocrysts deduced from compositional correlation between series. The bar below represents the scale of anorthite/magnesium-number.....90
- Figure 35.** Schematic illustration of the magma plumbing system beneath Tangkil and Rajabasa volcanoes based on thermobarometry calculation. It shows that the main magma storage region is at mid- to low-crustal level, while only high-Mg basalt magma from Rajabasa resides at upper mantle. The temporal data is also shown.....93
- Figure 36.** The magma plumbing system beneath Krakatau (Dahren et al., 2012) and the plotting of whole-rock composition (Camus et al., 1987; Mandeville et al., 1996a) on TAS diagram.....95

LIST OF TABLES

Table 1. The estimated densities values of crustal rocks beneath Krakatau Volcanic complex, Sunda Strait.	35
Table 2. The result of K-Ar age measurements.....	43
Table 3. Whole rock compositions of Rajabasa (Rbs) and Tangkil (Tkl).....	45
Table 3. Continued	46
Table 4. Different characteristics in lava samples among Tangkil and Rajabasa series.	84
Table 5. Geothermobarometer calculation results for Tangkil and Rajabasa volcanoes.....	92

CHAPTER I

INTRODUCTION

1.1 GENERAL INTRODUCTION AND BACKGROUND

Magma plumbing system has been investigated to understanding the characteristics of magmas beneath a volcano. These characteristics include identification of magmatic processes during magma evolution, magma emplacement depths, magma chamber composition and early-formed crystals. To clarify further about the evolution of magma plumbing system, a complete data set of petrological characteristics and their temporal variations must be employed. This information is thus fundamental to infer magmatic activity or even potential hazard associated with future eruption.

Temporal chemical variations of volcanic rocks from subduction-related volcanoes have been documented in the past decades (e.g. Newhall, 1979; Tsukui, 1985; Camus et al., 1987; Prosser and Carr, 1987; Gertisser and Keller, 2000, 2003a; Amma-Miyasaka and Nakagawa, 2003; Wibowo, 2017) by integrating stratigraphy, isotopic dating, and whole-rock chemistry to understand the magmatic evolution. These works have been able to clarify the dynamics of underlying magmas and geochemical evolution of magma system primarily based on the temporal change in whole-rock chemistry.

In order to study temporal chemical variations, in addition to geochemical data, stratigraphic study and isotope dating analyses are required to establish the stratigraphic order of lava flows. Therefore, in this kind of study, detailed stratigraphy must be established first before discussion of chemical criteria.

The temporal variations as a result of evolution of magmatic systems are detected at various time scales (Newhall, 1979): short-, medium-, and long-term. Short-term variations include variations within a single eruption; for instance, compositional variation or inhomogeneity of volcanic products occurring in a single lava unit in minutes or hours. Medium-term variations, on the other hand, refer to changes within a series of eruptions, generally at time scales ranging from years to thousands of years. The wider temporal range of medium-term variations is significant for portraying magmatic processes within an eruptive sequence. Long-term includes variations that may occur over the entire lifetimes of a volcano or volcanic field, up to tens of million years. Instead of depicting

cyclic volcanic activity, long-term variations conceptually describe different magma source compositions for storage systems beneath the volcano.

The variations in many calc-alkaline volcanic rocks are accounted for by periodic influxes of mafic magma to shallow felsic magmas (e.g. Newhall, 1979 for Mayon, Philippines; Tsukui, 1985 for Daisen, Japan; Camus et al., 1987 for Krakatau, Indonesia; Prosser and Carr, 1987 for Poás volcano, Costa Rica; Gertisser and Keller, 2000, 2003a for Merapi, Indonesia; Amma-Miyasaka and Nakagawa, 2003 for Miyake-Jima, Izu-Mariana Arc; Toya et al., 2005 for Aoso, Japan; Wibowo, 2017 for Sundoro, Indonesia). They suggested that the interplay of magmas emplaced at various depths had contributed to the eruptive processes in those volcanoes. The generation of basaltic andesite (*c.* 56 wt% SiO₂) in Merapi (Gertisser and Keller, 2003a), for instance, is formed by fractional crystallization of parental mafic magma (*c.* 52 wt% SiO₂) during the absence of influxes of less evolved magma from depth. However, in the periods of supply of primitive magmas, the magmas will eventually mix with the residual magma in shallower reservoir and decrease the contents of whole-rock SiO₂.

In previous studies, the evolution of magma systems was mostly discussed on the basis of temporal variations in whole-rock chemistry also with phenocrysts mineral chemistry (e.g. Borgia et al., 1988; Amma-Miyasaka and Nakagawa, 2003; Takahashi and Nakagawa, 2015) and not all were understood by thorough observation of textures, zoning patterns, and assemblages of minerals with temporal chemical variation (e.g. Humphreys et al., 2006, Higgins et al., 2015).

In many Sunda Arc volcanoes, magmatic evolutions have been discussed based on whole-rock and mineral chemistry (e.g. Foden, 1983; Reubi and Nicholls, 2004; Gardner et al., 2012; Dempsey, 2013; Innocenti et al., 2013; Métrich et al., 2017), whereas detailed investigations based on mineral textures are limited (Carn and Pyle, 2001; Wibowo, 2017). The magma plumbing of highly active Krakatau volcanic complex, which is located 20 km to the SW of Tangkil and Rajabasa, was established by employing a suite of thermobarometry models (Dahren et al., 2012). Since magmatic history is reflected in eruptive products for some extents, a thorough observation of mineral textures,

compositional zoning patterns, and mineral assemblages together with temporal chemical variation must also be taken into consideration.

1.2 PREVIOUS STUDIES ON TANGKIL AND RAJABASA

This work is a case study to investigate temporal petrologic variations, including whole-rock chemistry and petrography, in volcanoes that are not well studied, Tangkil and Rajabasa volcanoes, Sumatra. No historical eruptions have ever been recorded in Tangkil and Rajabasa volcanoes, although Rajabasa presently shows active volcanic activity. While almost all previous studies on temporal variation focused on the short-term variations, the study of temporal variations here is limited to the entire lifespan of the volcano (especially for Rajabasa).

Andi Mangga et al. (1994) and Barber et al. (2005) reported that Tangkil and Rajabasa volcanoes are characterized by andesitic volcanic centers. Nazarwin et al. (1994) and Suswati et al. (2001) have conducted geological mapping of Rajabasa volcano on the basis of field observation and remote sensing. Hasibuan (2014) carried out study of fractures distribution on Rajabasa volcano and its relation with the occurrence of geothermal manifestations. Kusumasari (2011) and Darmawan (2015) described the geothermal system beneath Rajabasa volcano (especially in southern flank of volcano) through field observation and water geochemistry of hot spring fluid.

On the other hand, Bronto et al. (2012) reported that Rajabasa volcano erupted basaltic to andesitic lava flows and established the evolution model of Rajabasa volcano based on remote sensing analysis and field geologic work. Bronto et al. (2012), however, did not carry out detailed petrographic works and the identification of endmember magmas has not been discussed. Therefore, the chronological evolution of the magma system was not clear. To understand magma evolution, age determination of lava units and detailed petrological study are necessary. The temporal variations are important to clarify the evolution of magmas beneath Tangkil and Rajabasa.

1.3 THESIS AIMS AND OBJECTIVES

This study aims to provide new insights on the volcanic history and the evolution of magma plumbing system in Tangkil and Rajabasa volcanoes. The lava stratigraphy was established by field observations and geomorphological analysis, supplemented by K-Ar ages. This work also presents new data of whole-rock major and minor elements, and mineral chemistry for rocks from both volcanoes. The stratigraphy, whole-rock chemistry, and petrography data presented in this study are directed to show temporal petrological variations.

The approach in this study involves the description of petrological variations by a careful observation on mineral textures, compositional zoning patterns, and mineral assemblages. This observation helps to identify the magmatic processes in which the minerals have been through during the evolution of magma system. Modelling of major elements with MELTS calculation was also carried out to support idea drawn from whole-rock diagrams. The endmember magmas were identified via whole-rock and mineral chemistry. Then, their intensive parameters (conditions of T - P) were estimated using thermobarometry models. This estimation clarifies the magma storage regions beneath Tangkil and Rajabasa volcanoes.

CHAPTER II

GEOLOGICAL BACKGROUND

2.1 GEOTECTONIC SETTING

Several subduction-zone systems are related to the activity of active volcanoes in Indonesia, namely the Sunda, Sangihe, Halmahera, and Banda volcanic arc systems (figure 1). The Sunda volcanic arc system is related to current subduction of the Indo-Australian Oceanic Plate beneath the Eurasian Continental Plate with a convergence rate of $6\text{--}7\text{ cm a}^{-1}$ (McCaffrey, 1991; Hall, 2009). The Sunda Arc is an active volcanic belt and one of the largest volcanic belts on Earth as it stretches over 5600 km from the Andaman Islands in the northwest to Banda Arc in the east (figure 1).

The Sunda Strait is a unique volcanic region in Sunda Arc as it is a transitional zone between the Java perpendicular and Sumatra oblique subductions (e.g. Huchon and Le Pichon, 1984; Malod et al., 1995; Barber et al., 2005) (figure 1). The oceanic lithosphere subducting obliquely beneath Sumatra is younger than 100 Ma (Katili, 1975), whereas that subducting almost perpendicular beneath Java and eastern Sunda arc is comparatively older (Hamilton, 1979; Widiyantoro and van der Hilst, 1996, 1997). There is also a volcanic alignment across the Sunda Strait, that runs through from Panaitan Island, via Krakatau Island, the Sebesi and Sebeku Islands, Tangkil and Rajabasa volcanoes, to the Sukadana basalt plateau from SSW to NNE (figures 1 and 4). This volcanic alignment lies almost perpendicular to the Java Trench. Tangkil and Rajabasa volcanoes are neighbors, where Rajabasa volcano is adjacent to Tangkil volcano to NW. Tangkil and Rajabasa volcanoes are situated ~ 300 km northeast of the Java Trench, while the most front volcanic area in Sunda Strait, Panaitan Island, is situated ~ 170 km northeast of the Java trench.

The Sunda Strait is tectonically complex (e.g. Ninkovich, 1976). It is an area of extensive faulting and rifting. In addition to the N-S compressional force related to the subduction in the southern regime, the strait has undergone an extension as a result of clockwise rotation of Sumatra relative to Java since late Cenozoic (Nishimura et al., 1986; Harjono et al., 1991). Nishimura and Harjono (1992) informed that the crust in the Sunda Strait is as thick as ~ 20 km compared to 25-30 km in the Sumatra Island and West Java. As reported by Jarrard (1986), the rotational movement is associated with the change of

the convergence angle from nearly orthogonal (12°) in front of Java to oblique (57°) in front of Sumatra. The Sukadana basalt plateau, which is relatively located at back-arc of Sumatra, was identified as MORB-type basalts, grew up at 0.8-1.2 Ma (Nishimura and Harjono, 1992). This geodynamic complexity has formed one of the most active tectonic and volcanic regions in Indonesia (Huchon and Le Pichon, 1984).

The Sumatra Fault System (Semangko) is an active and major strike-slip dextral fault zone that extends NW-SE from Andaman Sea to Sunda Strait (e.g. Barber et al., 2005) (figure 4). This fault does not pass the Sunda Strait, but it ends between Sumatra and Java in a normal faults zone associated with subsidence (Huchon and Le Pichon, 1984). This fault, which is also known as Central Sumatra Fault, was thought present to accommodates the oblique subduction. In addition to the clockwise rotation of Sumatra relative to Java, Huchon and Le Pichon (1984) also suggested that the northwestward displacement of a Sumatra fore-arc sliver plate along the Sumatra Fault System generated the transtensional tectonic regime in the Sunda Strait.

Lampung Fault is the local manifestation of Semangko Fault in the study area. The previous geological map (figure 2) and the topographic map (figure 3) show dominant NW-SE linear structures on Tangkil and Rajabasa volcanoes. Accordingly, Suswati et al. (2001) have also suggested that a strike-slip fault system has developed in Rajabasa volcanic area. The geothermal manifestations (solfatara and fumarole) in the northern flank of Rajabasa volcano are controlled by these structures (Suswati et al., 2001). Therefore, in addition to the slab subduction in the southern margin, the volcanism of Tangkil and Rajabasa volcanoes have been affected by the Sumatra Fault System.

These observations indicate that Tangkil and Rajabasa volcanoes are built on a region with a complex tectonic setting where compression results from slab subduction and extension results from clockwise rotation of Sumatra relative to Java.

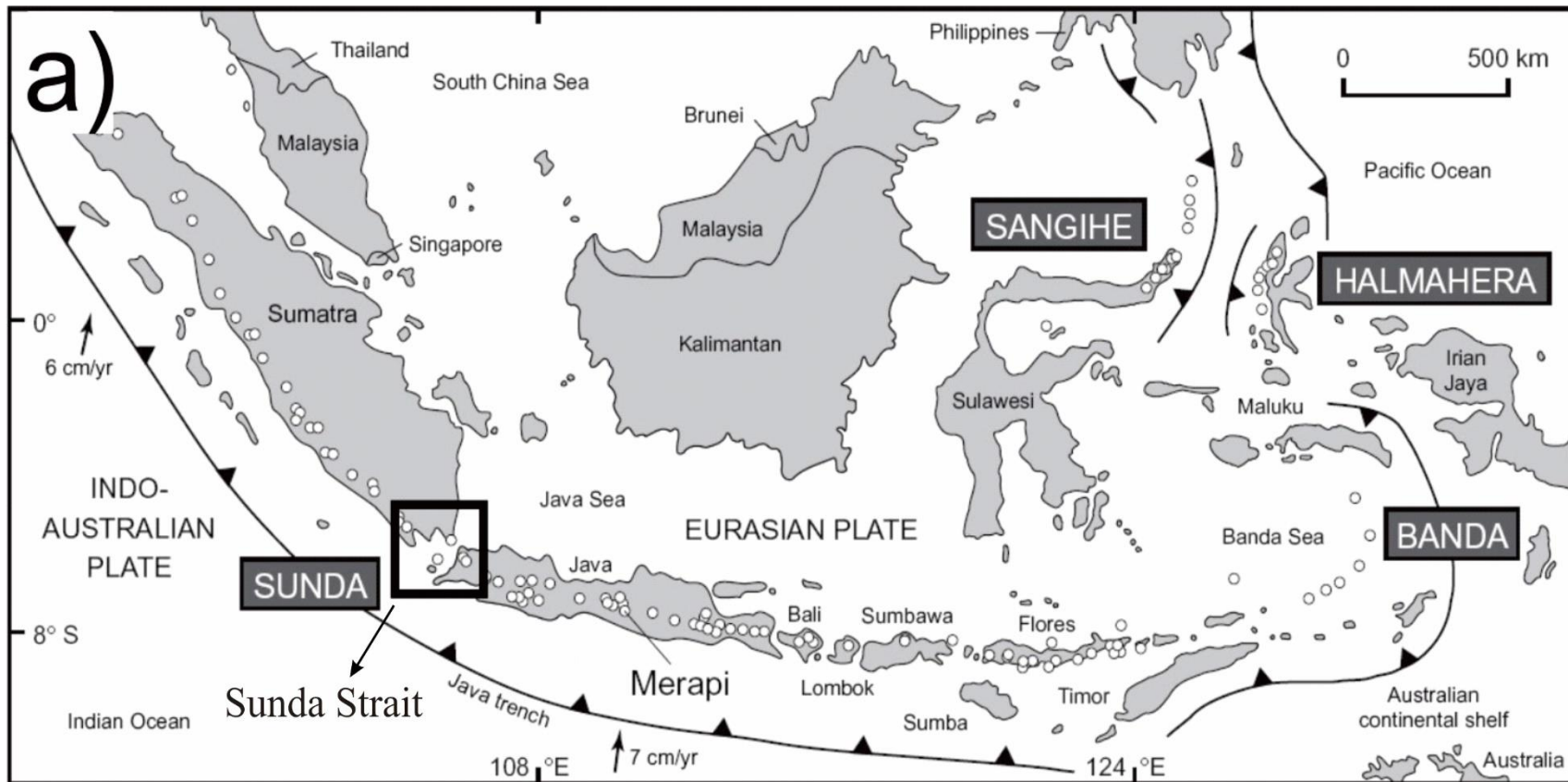


Figure 1. Map of the subduction-zone system in Indonesia (Gertisser and Keller, 2003b). Indo-Australian Oceanic Plate is subducting beneath Eurasian Continental Plate (6-7 cm/a). This activity results to magmatism (Sunda Arc), stretching from the Andaman Island to Banda Arc. Active volcanoes (o) and Sunda Strait (□) are shown in the map.

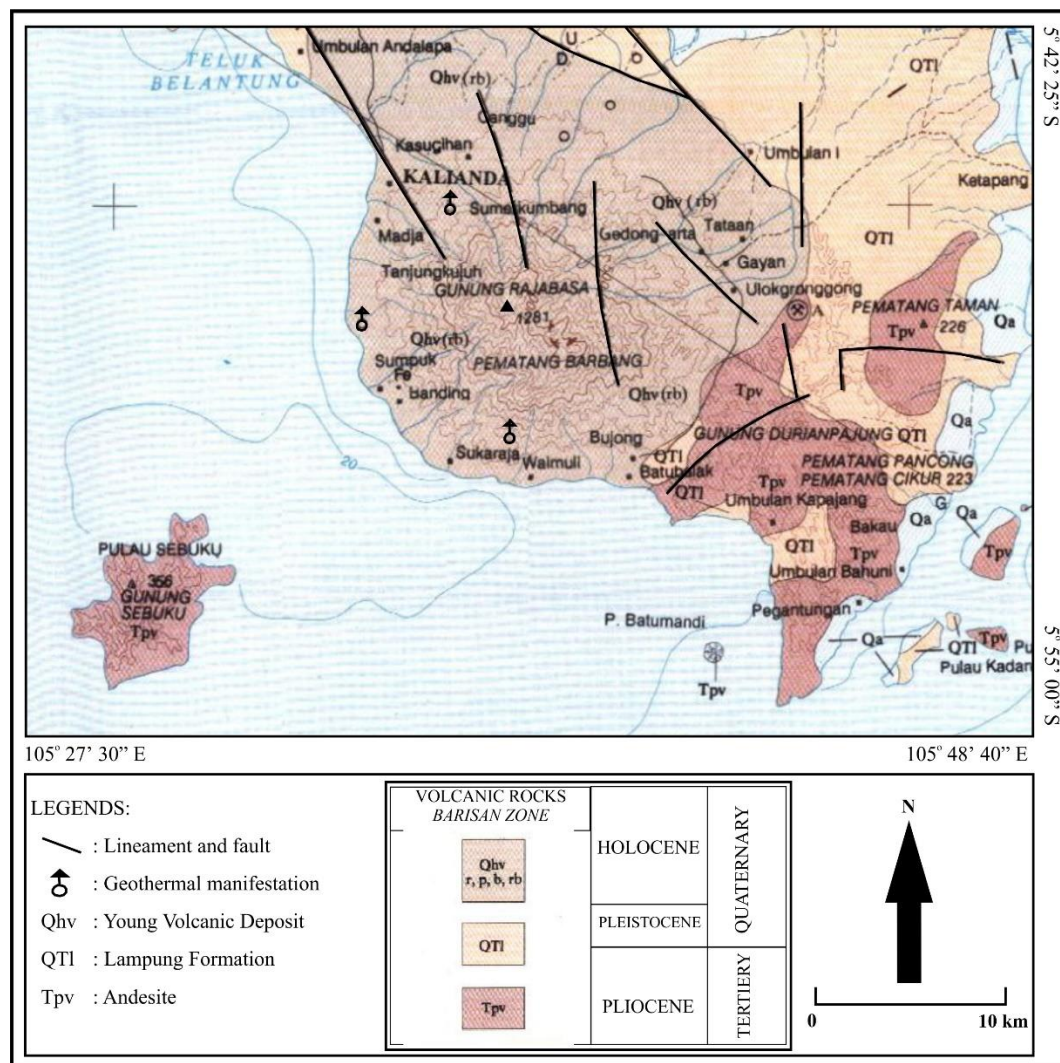


Figure 2. A former geological map of volcanic rocks in southern Lampung, Sumatra by Andi Mangga et al. (1994).

2.2 GEOLOGICAL BACKGROUND

Volcanoes in Indonesia are classified into type A, B, and C based on the intensity or historical eruptions. Volcanoes where a magmatic eruption took place after the year 1600 are categorized as type A. Type B is for volcanoes that have no eruption history after 1600, but still show volcanic activity, such as solfatara. Type C includes volcanoes whose eruption history is unknown. Despite of the absence of historical eruptions in Tangkil, the remnants of the ancient volcanic edifices are still visible. Rajabasa is a dormant volcano,

but some volcanic activity, such as fumarole, solfatara, and hot springs, are still manifested on this volcano. According to this classification system, Tangkil is classified as type C, whereas Rajabasa as type B volcanoes.

Andi Mangga et al. (1994) established a geological map named “Peta Geologi Lembar Tanjung Karang, Sumatra” (figure 2). That map describes Rajabasa and its vicinity as volcanic products from Pliocene to Holocene. They divided the volcanic products into three big groups: andesite formation (Tpv), Lampung tuffs (QTI), and young volcanic deposits (Qhv) in order from oldest to youngest.

There is no detailed geologic study regarding volcanic activities in Tangkil volcano yet as the original lava geomorphology has been lost by erosion (figure 3). In the geological map by Andi Mangga et al. (1994) (figure 2), Tangkil volcanic products are described as the Tertiary andesite lava (Tpv). The volcanic products from Tangkil volcano are distributed from the southeast of Rajabasa volcano to the Bakauheni seaport in the southeast. The deposits from Tangkil volcano are overlain by later pyroclastic fall deposits, which are named as Lampung tuffs (van Bemmelen, 1949; Andi Mangga et al., 1994). According to Nishimura (1980) and Nishimura et al. (1984, 1986), Lampung tuffs were spewed at the southern end of Semangko fault at 1 ± 0.2 Ma to 0.09 ± 0.01 Ma. Lampung tuffs were described by Andi Mangga et al. (1994) as pumiceous tuffs, rhyolitic tuffs, or sandy tuffs, erupted in the late Pliocene to Pleistocene.

Lava morphology is well preserved on Rajabasa volcano so that studies of lava stratigraphy can be established by observing the overlapping lava morphologies. Andi Mangga et al. (1994) (figure 2) described Rajabasa volcano as Young Volcanic Deposits (Qhv), dominated by andesite-basalt lava. Volcanic rocks of Rajabasa overlie the Lampung Tuffs.

Bronto et al., (2012) established the evolution of Rajabasa volcano as follows: construction of the Pre-Rajabasa composite cone, destruction of the Pre-Rajabasa cone by a huge eruption leaving the 25-km-diameter Pre-Rajabasa caldera (figure 3), and the construction of the Rajabasa cone inside the Pre-Rajabasa caldera. The volcanic rocks of

Pre-Rajabasa cone are not exposed because of erosion. The ridge of Pre-Rajabasa caldera, however, can be recognized on *c.* 5 km outward from the northern and eastern base of Rajabasa volcano by an arc-shaped ridge (figure 3). All the existing lava inside the ridge belong to Rajabasa volcano formed after the collapse of Pre-Rajabasa caldera.

CHAPTER III

SAMPLE SELECTION AND ANALYTICAL TECHNIQUES

3.1 FIELD SURVEY AND SAMPLE SELECTION

In this study, a total of 26 fresh lava and dyke samples were collected for Tangkil and Rajabasa volcanoes. The sample number and distribution are shown in figure 3. The detailed localities and description of these samples are given in appendix (A: location and description of samples). The sampling covers two units from Tangkil volcano and eleven units from Rajabasa volcano. Exposure of fresh volcanic rocks is limited by thick vegetation. For this reason, some lava units from Rajabasa volcano were not able to be sampled (Rbs 3, Rbs 4, Rbs 5, Rbs 12, Rbs 13, Rbs 14, and Rbs 17).

In addition, field survey to Krakatau Islands and Sebesi Island were done and a total of 13 lavas and pyroclastics from both volcanoes were collected. Especially for Sebesi Island, the exposure of fresh volcanic rock is very limited. The existence of exposure in the southern coast of the Sebesi Island must be associated with Krakatau 1883's eruption origin. The Krakatau and Sebesi are the two most nearby volcanoes from Tangkil and Rajabasa to the SSW, therefore this additional data might be useful in later discussion to show spatial variations.

Thin sections and rock powder were prepared from each sample for petrography and whole-rock chemical analysis. Polished thin sections were also prepared for electron microprobe analysis.

3.2 ANALYTICAL TECHNIQUES

3.2.1 Morphological analysis

A morphological analysis of Rajabasa volcano was carried out on the basis of the digital elevation model and a satellite image. This analysis was done to determine the stratigraphic correlation of lava units. Here, Light Detection and Ranging (LiDAR; only available for Rajabasa volcano) and Advanced Spaceborne Thermal Emission and Reflection Radiometer (ASTER) (figure 3) data were used to delineate each eruptive/flow unit, lineaments, and areal morphology by utilizing Geographic Information System (GIS)

and Global Mapper software. The LiDAR data was obtained from Hasibuan (2014) and DEM (ASTER) data is open access provided by U.S. Department of the Interior, USGS.

This analysis can provide the recognition and localization of the main volcanic features (e.g. Norini et al., 2004). As lava lobe geomorphology is well preserved, the sequence of lava was established based on the geomorphological analysis, as well as the relationship observed at exposures. Field observation is an important stage to ascertain order from morphological analysis.

3.2.2 Microscopic analysis

Textural and petrographic observation were carried out using Nikon Eclipse E600 POL microscope, at Department of Earth Science and Technology, Akita University.

This analysis requires thin section of the rock samples. The collected samples were cut in one side, polished, and fitted into slide glass. Epoxy resin was used to mount the samples onto slide glass. Then another side of chip sample was cut with secondary cutter. The side of chip sample that has been cut then was polished gradually with #150 up to #6000 in powder size. Agate plate was used to polish the sample with #6000 powder. For samples that contain vesicles or pores, they were at first molded using mixture of two resins, “Shuzai” as the main resin and “Kokazai” as the curing agent, with ratio of 3:1. The bubbles inside the sample were sucked up by putting it in the vacuum box. Then the following steps are the same with the previous treatment.

3.2.3 K-Ar isotope dating

Three lava samples were selected for K-Ar isotope dating; one basaltic lava sample from Tangkil volcano, and two andesitic lava samples from the youngest and oldest lava flow units of Rajabasa volcano. These ages were presumed by the new geological map. The analysis was carried out at Hiruzen Institute for Geology and Chronology Corp.,

Okayama, Japan. This analysis refers to Yagi (2006) for sample preparation, Nagao et al. (1984) for potassium analysis, and Itaya et al. (1991); Nagao and Itaya (1988); Nier (1950); Steiger and Jager (1977) for the Argon isotope analysis. According to the references, detailed of the methods are described in the following:

3.2.3.1 Sample preparation

The rock samples are thinly cut into about five millimeters in thickness by using a rock cutting machine, and then they were washed and dried in an oven (70°C). The samples were crushed by an iron mortar and sieved to obtain 60-80 mesh size fractions (*c.* 187-250 µm). The fraction was dispersed in distilled water using an ultrasonic bath and rinsed to remove fine particles on the surface of the grains and then dried in an oven (70°C). Iron fragments contaminated in the crushing, very strong magnetic and non-magnetic minerals in the fraction were excluded with a hand magnet and an isodynamic magnetic separator. Mineral separation follows the method reported by Yagi (2006).

3.2.3.2 Potassium analysis

The groundmass samples (*c.* 100 mg) were decomposed by mixture acid solution of HNO₃ and HF teflon beaker for about 12 hours. In addition, it was evaporated and dried on hot plate, and then hydrochloric acid solution of them was created. Qualitative analysis of potassium was carried out by flame photometry using a 2000 ppm Cs buffer. The analysis was performed twice or more to confirm the reproducibility of the sample. An average value of multiple runs was used for a calculation of age. Analysis of potassium and their errors follow the method reported by Nagao et al. (1984).

3.2.3.3 Argon isotope analysis

The groundmass samples of known weight (*c.* 1 gram) were wrapped in thin aluminum foil and put into a sample holder consisting of a pyrex-glass tube with 11 branches, and then they were heated at 180-200°C by ribbon and mantle heater for about 72 hours to emit adsorption gas in a vacuum. Then, the sample gas was extracted by carrying out heating dissolution in the Mo crucible for 30 minutes at about 1500°C by

tantalum (Ta) heater was mixed together the calibrated argon 38 spike (called isotopic dilution method) in ultra-high vacuum line.

Purified argon gas was analyzed on a 15 cm radius sector type mass spectrometer with a single collector by an isotopic dilution method using an argon 38 spike (called “HIRU”, Itaya et al., 1991). Calculations of the age and its error follow the methods described by Nagao et al. (1984) and Nagao and Itaya (1988). The decay constants for ^{40}K to ^{40}Ar and ^{40}Ca , and ^{40}K content in potassium used in the calculation of age follow those after Steiger and Jäger (1977): $0.581 \times 10^{-10}/\text{year}$, $4.962 \times 10^{-10}/\text{year}$ and 1.167×10^{-4} , respectively. The errors for the obtained ages are at the two-sigma confidence level.

3.2.4 X-Ray Fluorescence (XRF)

Whole-rock chemical compositions were determined with X-ray fluorescence analysis (ZSX Primus II, Rigaku Co. installed at Akita University) using glass bead method. The powder samples were prepared by grinding in agate mill. The powder samples were furnace at 900°C to release water and sulphur contents as well as to determine LOI. Then, the sample powders were prepared with an alkali flux, with proportion 3g of Merck Spectromelt®A10 ($\text{Li}_2\text{B}_4\text{O}_7$), 1g of Merck Spectromelt®A20 (LiBO_2), and 0.8g of powder sample. The dilution ratio of glass bead is 5 : 1 (flux of a mixture of $\text{Li}_2\text{B}_4\text{O}_7$ and LiBO_2 : rock). An exact mixture measurement is necessary for calibration to internal standard Li. After grinding the mixtures using agate mortar and pestle, they were fused at 1150°C to make glass beads.

Compositions of ten major elements (Si, Ti, Al, Fe, Mn, Mg, Ca, Na, K, and P) and nine minor elements (Ba, Zr, Rb, Sr, Nb, Cr, Ni, Y, and V) were determined by matrix-corrected calibration curves obtained from the measurements of 15 samples of GSJ (Geological Survey of Japan) Igneous Rock Series.

3.2.5 Scanning Electron Microscope-Energy Dispersive Spectrometer (SEM-EDS)

Back-scattered electron images (BSEI) were captured with the scanning electron microscope (SEM: JSM-6610LV, JEOL Co.) and line-scanning analysis of individual minerals were carried out using energy-dispersive X-ray spectroscopy (EDS: INCA X-act, Oxford Instruments) at Akita University. The conditions of this analysis were set at: an acceleration voltage of 15 kV, a probe current of 2.2 nA, and working distance of 10 mm.

3.2.6 Scanning Electron Microscope-Wavelength Dispersive Spectrometer (SEM-WDS)

The composition of phenocrysts and groundmasses are mainly obtained through this quantitative analysis. For electron probe micro-analysis (this analysis also known as EPMA), six samples from Tangkil and eight samples from Rajabasa were observed. The thin sections were polished until #6000 on agate plate and with diamond paste (1 μ m and $\frac{1}{4}$ μ m). The polished specimens were then coated on surface with carbon with thickness of 20-25 μ m.

Back-scattered electron images (BSEI) and microprobe analysis were performed in several sessions using JEOL WDS electron microprobe JXA 8800 and JXA 8230, installed at Akita University at Department of Earth Science and Technology. The conditions for this quantitative analysis were set at 15 kV for accelerating voltage, 20 nA for beam current, 2-15 μ m for probe diameter, 10-20 s for peak counting times, and oxide & ZAF for correction method.

Probe diameter of 2-5 μ m were usually used for phenocryst (all 5 μ m for plagioclase), while defocused beam (5-15 μ m) used for glass and whole-rock groundmass analysis. The cores and rims of phenocrysts were analysed separately. Cores were selected based on zoning textures, usually the most inner part of crystal; rims were located at a few microns inside the crystal peripheries. Mantle was identified as a part of crystal between core and rim.

For silicate mineral analysis, synthetic minerals of eminent compositions that were used as standard are jadeite for Si and Na, rutile for Ti, corundum for Al, chromium oxide for Cr, hematite for Fe, manganosite for Mn, periclase for Mg, wollastonite for Ca, and KTiPO_4 for K.

Element condition of WDS measurement with JXA 8800 was ordered in: Channel 1 (TAP crystal) for Si and Al; Channel 2 (PETJ crystal) for K, Ca, and Ti; Channel 3 (LIF crystal) for Fe, Cr, and Mn; and Channel 4 (TAP crystal) for Na and Mg, whereas analysis with JXA 8230 was ordered in: Channel 1 (TAPH crystal) for Na and Mg; Channel 2 (TAP crystal) for Si and Al; Channel 3 (LIF crystal) for Ti and Cr; Channel 4 (LIFH crystal) for Mn, Fe, and Ni; and Channel 5 (PETH crystal) for K and Ca. Element of Na was analysed in the first sequence to minimize Na loss during analysis.

For oxide mineral analysis, vanadium for V, KTiPO_4 for P, and the rest standards follow the silicate minerals. For this analysis, element condition of WDS measurement with JXA 8230 was rearranged and ordered in: Channel 1 (TAPH crystal) for Na and Mg; Channel 2 (TAP crystal) for Si and Al; Channel 3 (PETJ crystal) for K, Ca, and P; Channel 4 (LIFH crystal) for Mn, Fe, and Cr; Channel 5 (LIFH crystal) for Ti, V, and Ni. The complete result of this analysis for a total of 14 polished specimens is given in appendix (D: mineral chemistry).

3.3 INTENSIVE PARAMETERS CALCULATION METHODS

The calculation methods to estimate the temperatures and pressures in each series are chosen by the existing equilibrium mineral assemblages. Equilibrium mineral pairs should be established first before their T - P estimates are determined. Each series has different equilibrium mineral assemblages, so the thermobarometry models used for calculation may be different by series. In the estimation of T - P values, the accurate results could be only acquired by finding the appropriate equilibrium mineral or melt compositions.

Thermobarometry calculation

In the estimation of T - P values, the calculation employed models of two pyroxene pairs (Putirka, 2008; Brey and Kohler, 1990), clinopyroxene-melt (Putirka, 2008; Neave and Putirka, 2017), olivine-melt (Putirka et. al., 2007), single clinopyroxene (Putirka, 2008), and plagioclase-hornblende (Holland and Blundy, 1994). The selected thermobarometry model, mineral pairs used, and their estimate results are listed in table 5 in discussion.

The mineral-melt equilibrium tests are commonly fulfilled by exchange coefficients of elements (Longpré et al., 2008; Barker et al., 2009). The equilibrium test of pyroxenes- or olivine-based thermobarometers was performed by comparing the observed Fe-Mg exchange coefficient ($K_D(\text{Fe-Mg})$) between minerals or mineral and melt with a constant value. Only mineral pairs with $K_D(\text{Fe-Mg})$ values falling within equilibrium range were considered reliable and used to draw interpretation. More detailed information for some models are given below.

a) Plagioclase-hornblende thermobarometer

This thermobarometry calculation was used for rocks from Tangkil (Tklf). An adjacent pair of hornblende rim and plagioclase rim compositions were used for this model. To determine the structural formula of hornblende, estimation of Fe^{2+} and Fe^{3+} contents were done with method by Holland and Blundy (1994). Temperatures are calculated by the HB1, HB2, and BH. The values used in this study is ones from HB2, which refers to Holland and Blundy hornblende-plagioclase thermometry calibration reaction $\text{endite} + \text{albite} = \text{richterite} + \text{anorthite}$. The HB2 values are also preferred by Anderson (1996) as it is more appropriate to compute for pressure and temperatures.

b) Clinopyroxene-orthopyroxene (two pyroxene pairs) thermobarometer

In this study, model of two-pyroxene based thermometers by Putirka (2008) in most cases was used to estimate temperature and pressure. An adjacent of clinopyroxene-

orthopyroxene are the ideal pairs for calculation. The new global regression which based on the partitioning of enstatite + ferrosilite between clinopyroxene and orthopyroxene has increased calculation precision. For pressure estimation, eqn. 39 was preferred in which the T used as input so thus the precision is greatly increased. It is also implied by superior value of standard errors of estimate (SEE) of ± 38 °C [eqn. 37] and ± 2.8 kbar. The equilibrium test of pairs used in the calculations using Fe-Mg exchange coefficient, where the equilibrium value ($K_{d[\text{Fe-Mg}]}$) of only 1.09 ± 0.14 were used. Two-pyroxene pairs whose $K_{d[\text{Fe-Mg}]}$ values out of 1.09 ± 0.14 were eliminated. Model by Brey and Kohler (1990) was used for comparison. Their thermometer model [BKN] is based on some forms of enstatite-diopside partitioning. The SEE for this model is ± 50 °C.

c) *Clinopyroxene-melt thermobarometers*

This thermobarometry calculation was usually chosen for samples that do not precipitate equilibrium pairs of both ortho- and clino-pyroxene phenocrysts. Two models are applied based on clinopyroxene-melt equilibria, Putirka (2008) and Neave and Putirka (2017), which the former model has been used frequently in the last decade. Barometer in Putirka (2008) is based on the Al partitioning between clinopyroxene and melt. The SEE for anhydrous system in this model are ± 45 °C [eqn. 34], ± 58 °C [eqn. 32d] and ± 2.9 kbar [eqn. 31], ± 3.1 kbar [eqn. 32a]. A new barometer model of Neave and Putirka (2017) was calibrated from experimental data in a wider barometric range to improve the accuracy of jadeite into clinopyroxene and comes with a SEE of ± 1.4 kbar. The temperatures in this model were calculated in concert with eqn. 33 from Putirka (2008). The equilibrium test between clinopyroxene and a coexisting liquid for the two models is made by comparing observed and predicted values for Fe-Mg exchange, which should be 0.27 ± 0.03 .

d) *Plagioclase-melt hygrometer*

The melt H₂O was additionally calculated using Waters and Lange (2015) with plagioclase-melt hygrometers. This calculation needs input of temperature and pressure. Temperature and pressure were determined from mineral pairs, and the results are used for hygrometer calculation. Plagioclase phenocrysts from Rbs samples do not contain glass melt inclusion (if any, it is so tiny and inappropriate for microprobe analysis).

Groundmass in Tangkil samples contain glass. The glass composition paired with adjacent plagioclase rim composition is applicable for the calculation. The estimate H₂O values using this mineral-melt pairs, however, represent the conditions during latest crystallization or pre-eruptive stage.

Depth calculation

Calculation of depths was obtained by converting pressure (kbar) to depth (km) using densities of the respective stratigraphic units beneath Sunda Strait from Kopp et. al. (2001) (table 1). This study was carried out by a seismic line over the Java trench, ending only *c.* 30 km SW of Tangkil and Rajabasa. The accumulative depth of crustal lithologic units by Harjono et. al. (1989) (table 1) was also taken into consideration in calculation. Since the block faulting of basement and crustal thinning were estimated to have a total extension of 50-100 km over the strait (Diament et al., 1992; Malod and Kemal, 1996; Susilohadi et al., 2009), the stratigraphic units and their accumulative depths were presumed to continue underneath Tangkil and Rajabasa.

Table 1. *The estimated densities values of crustal rocks beneath Krakatau Volcanic complex, Sunda Strait (after Dahren et al., 2012).*

Inferred rock types	Depth (km) (Harjono et al., 1989)	Density (g/cm ³) (Kopp et al., 2001)
Sedimentary layers	0-4	2.32 (2.23-2.4)
Granitoids	4-9	2.8
Diorite or gabbro	9-22	2.95
Mantle	>22	3.37

CHAPTER IV

RESULT

4.1 GEOLOGY OF TANGKIL AND RAJABASA VOLCANOES

Volcanic centers of Tangkil and Rajabasa volcanoes are aligned along a SE-NW direction, over a distance of *c.* 11 km. The boundary between Tangkil volcanic products and Rajabasa volcanic products is located on the flat plain along the northwestern base of Tangkil volcano (Semanak village) where the Lampung tuffs are distributed. Lampung tuffs overlie the volcanic products of Tangkil and are overlain by volcanic products of Rajabasa.

Tangkil and Rajabasa volcanoes have different degrees of erosion. Tangkil volcano has lost its original morphology and thus it is regarded as the remnant of an old volcanic edifice (figure 3). Geomorphology of the volcano is a hill with slopes of 5° to 35° . Tangkil volcano is originally a composite volcano that consists of lava and lahar deposits. Rajabasa volcano is a steep-sided volcano with radial slopes of more than 20° . Rajabasa volcano is a composite volcano, composed of dominant lava, tuff, volcanic breccia, and lahar deposits. Rajabasa volcano consists of two main volcanic cones (figure 3): Rajabasa cone and Balerang cone. The younger eruption center of Rajabasa cone is located in the NW of the older eruption center of Balerang cone. Bronto et al. (2012) suggested the two volcanic cones were formed by the movement of eruption centers from SE to NW. Two horseshoe-shaped depressions on the northern and western flanks of the Balerang cone indicate the occurrence of sector collapses or landslides.

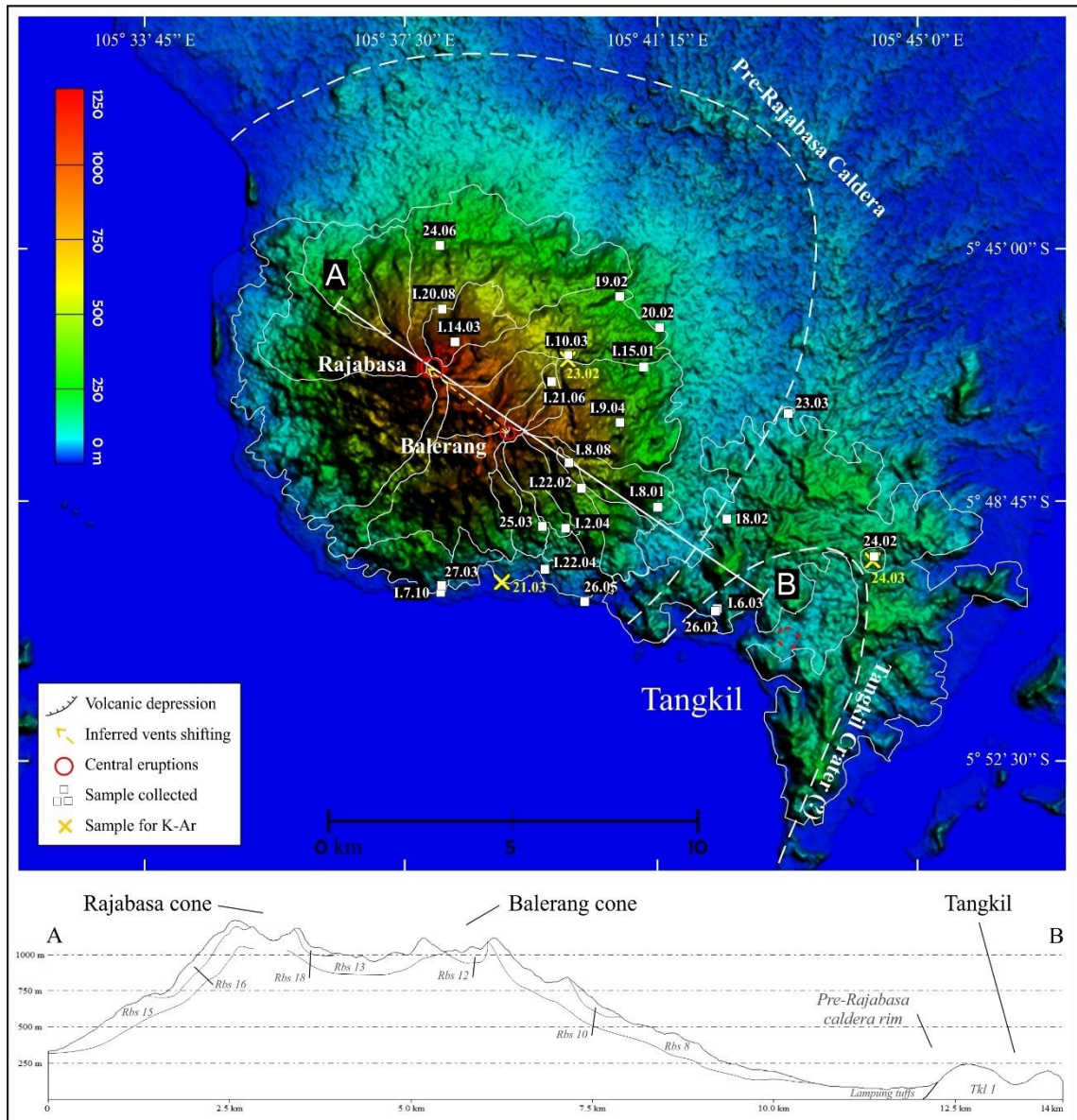


Figure 3. The ASTER image displaying Rajabasa volcano inside the caldera, as well as the NW trend of vents position from Tangkil to Rajabasa. The lower figure is the topographic cross section in this volcanic region, exhibiting the peaks.

A new geologic map and a lava stratigraphy of Tangkil and Rajabasa volcanoes are shown in figures 4 and 5. Tkl 1 from Tangkil volcano is the oldest unit in the area, which was later overlain by Tkl 2. The Tkl 1 is dominated by dacite lava. On the other hand, the Tkl 2 is dominated by basaltic rocks. The deposits of Tangkil volcano were overlain by Lampung tuffs. The earliest lavas of Rajabasa, Rbs 1 and Rbs 2, overlie the Lampung Tuffs. There are some units drawn in a parallel age because the stratigraphic orders of which another unit overlies the direct contact cannot be determined (Rbs 1 and Rbs 2, Rbs 7 and Rbs 8, Rbs 9 and Rbs 10) and they are regarded as concurrent products.

The lava in the southern and eastern flanks of Rajabasa volcano (Rbs 1 up to Rbs 12) were derived from the central vent of Balerang cone. The lava units from Balerang cone are dominated by andesite, accompanying minor basaltic andesite (Rbs 8) and basalt (Rbs 2) lavas. On the other hand, the basaltic andesite and andesite lavas on the northern and western flanks (Rbs 13 up to Rbs 18) were derived from the younger central vent of Rajabasa cone. The youngest andesite lava (Rbs 18) flowed to the eastern flank, into the horseshoe-shaped depressions of the older volcanic cone.

Field occurrences of the volcanic rocks from Tangkil and Rajabasa are lava, scoria deposit, and a dyke (figure 6). Volcanic rocks of Tangkil are widely distributed in Bakauheni and dominated by dacitic to rhyolitic lavas. The lavas are mostly blocky, and cooling joints (platy and columnar) are distinct in some lava units. All the lavas are more than 6 m thick. The felsic rocks are light grey in color and show porphyritic to aphanitic glassy textures. The basaltic rocks (Tkl 2 in figure 5) occur as strombolian scoria deposit and a dyke that intruded the dacitic lava (Tkl 1 in figure 5). In contrast to the felsic rocks, the basaltic rocks are distributed locally in Sidoluhur village. Scoria deposit and dyke have thicknesses more than 15 m and 30 m, respectively. The scoria clasts are brownish and vesicular.

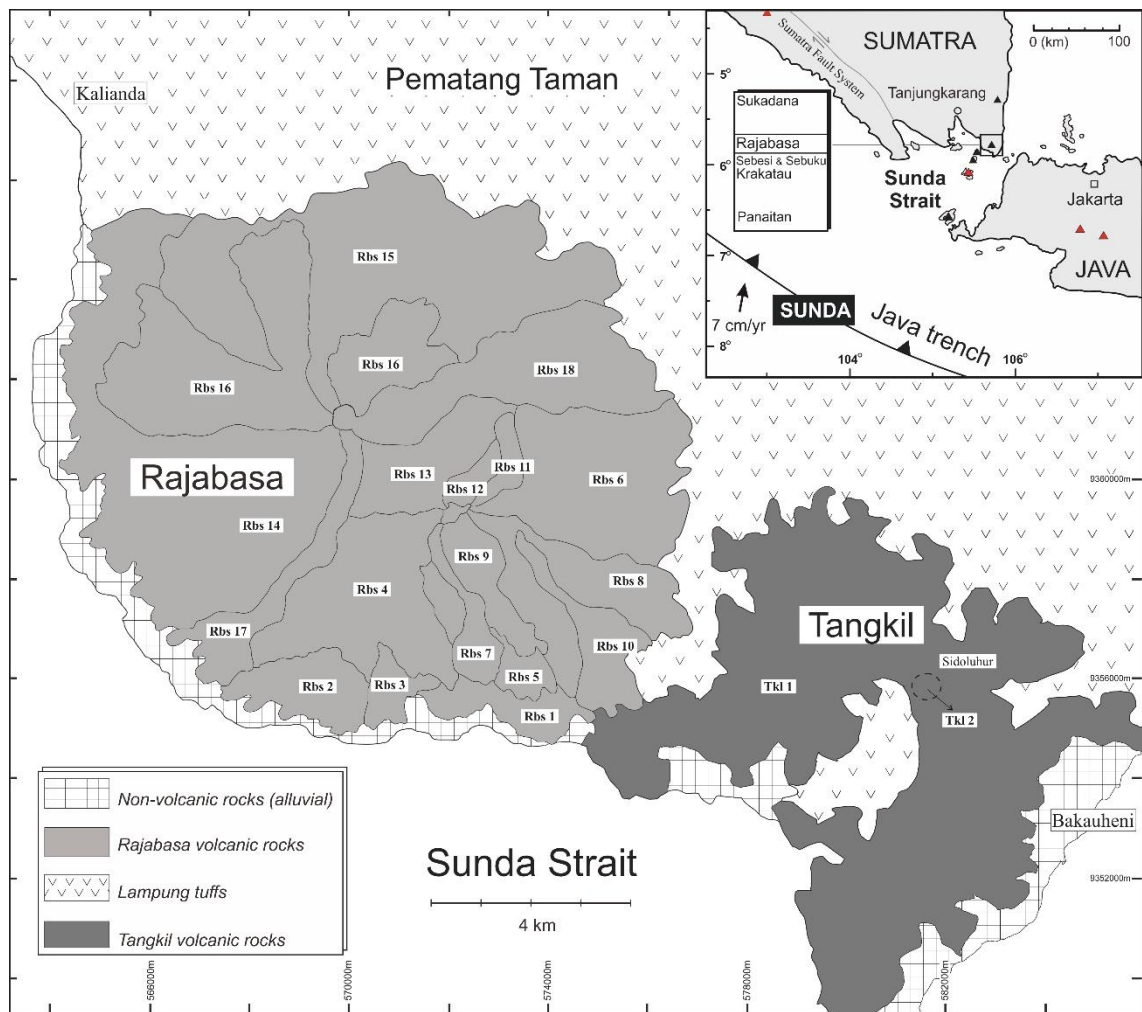


Figure 4. Geologic map displaying the distribution of Tangkil and Rajabasa unit lavas. The inset map shows the location of the volcanoes in Sunda Strait region. The labels (e.g. Rbs) indicate unit of lavas.

On the other hand, volcanic rocks of Rajabasa are dominated by basaltic andesite to andesite lavas. Most of the lavas are massive and dense, and some are autobrecciated and vesicular on the exterior. The thicknesses of lava range from a few meters to more than 50 m. The lavas are all porphyritic and have similar characteristics in groundmass color and phenocryst size but varying in phenocryst assemblages. The rocks are light to dark grey in color and contain phenocrysts with up to 4.3 mm in size. Variations of phenocryst assemblages are described further in petrography section.

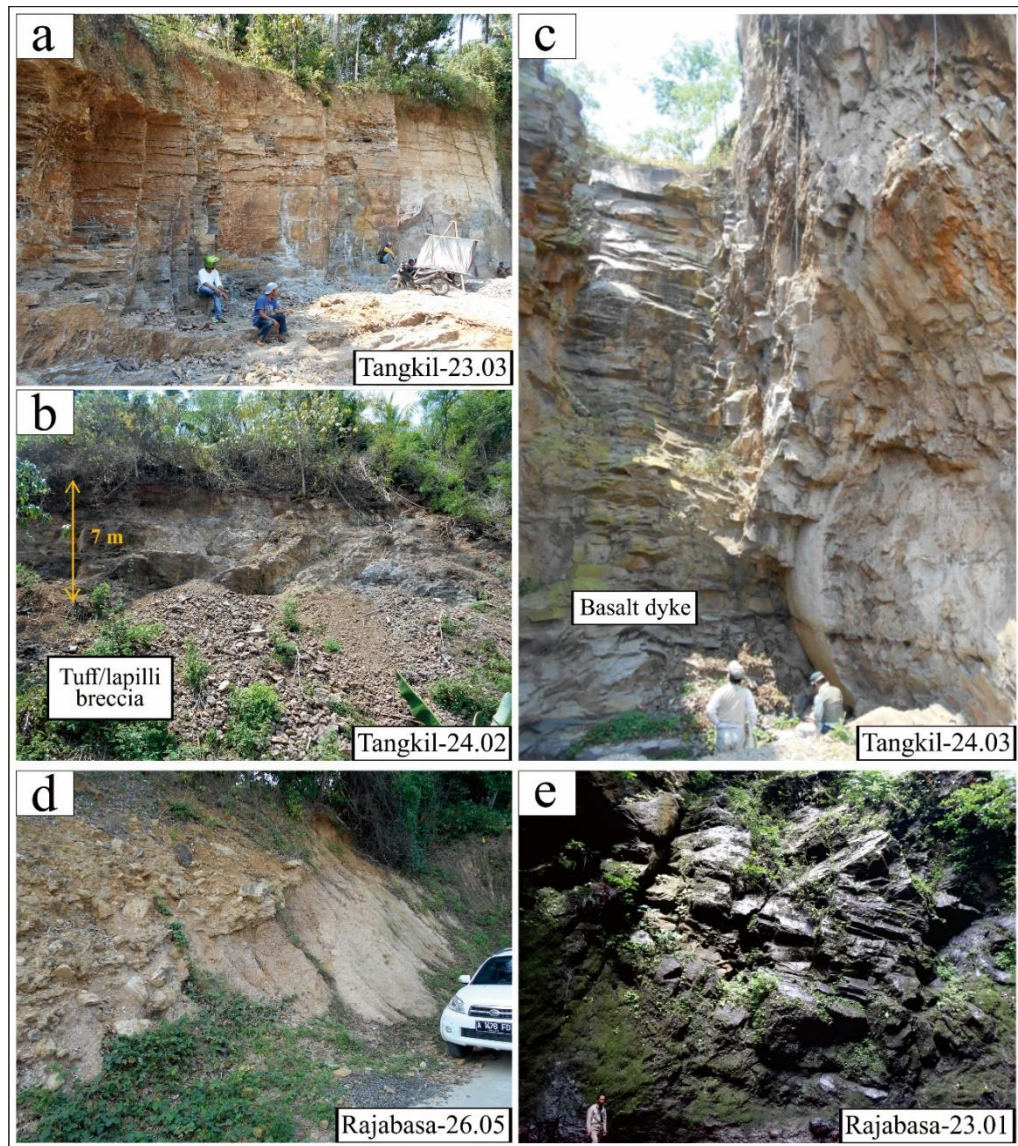


Figure 6. Some representative outcrops in Tangkil (a, b, c) and Rajabasa (d, e) volcanoes.

4.2 POTASSIUM-ARGON ANALYSIS

The results of potassium-argon (K-Ar) dating are shown in Table 2. The K-Ar age of the basalt from unit Tkl 2 of Tangkil volcano (sample 24.03 in Table 2) is *c.* 4.3 Ma (Pliocene). Samples from the oldest (Rbs 1) and the youngest (Rbs 18) lava units from Rajabasa volcano (21.03 & 23.02 in Table 2) were dated at *c.* 0.3 and *c.* 0.1 Ma, respectively. The result indicates that Rajabasa volcano is as young as Upper Pleistocene. The more detailed results of potassium analysis and K-Ar dating of these samples are given in appendix (B: K-Ar dating results).

Table 2. The result of K-Ar age measurement with an error of 2% for potassium analysis (more than 0.2 wt.%). Sample no. 24.03 is representative for Tangkil volcano, while sample no. 21.03 and 23.02 are for Rajabasa volcano. The term of “rad.⁴⁰Ar”, “non-rad.⁴⁰Ar”, and “STP” states for radiogenic argon 40, non-radiogenic argon 40 (atmospheric argon 40), and conditions of 0°C and 1 atm, respectively.

Sample No. (rock type)	Mineral (mesh size)	K content (wt.%)	Rad. ⁴⁰ Ar (10 ⁻⁸ cc STP/g)	Non-rad. ⁴⁰ Ar (%)	K-Ar age (Ma)	Age
23.02 (andesite)	groundmass (#60-80)	2.273 ± 0.045	1.07 ± 0.38	95.6	0.12 ± 0.04	Upper Pleistocene
21.03 (andesite)	groundmass (#60-80)	2.664 ± 0.053	3.16 ± 0.15	70.6	0.31 ± 0.02	Upper Pleistocene
24.03 (basalt)	groundmass (#60-80)	0.782 ± 0.016	13.16 ± 0.41	61.3	4.33 ± 0.16	Pliocene

4.3 MAJOR AND TRACE ELEMENT VARIATIONS

The studied samples of this volcanic area exhibit a large variation in SiO₂ (51-71 wt%) (figure 7). The compositional ranges of Na₂O, K₂O, and MgO are 2.8-5.4 wt%, 0.61-3.0 wt%, and 0.1-7.1 wt%, respectively (Table 3).

The variations of MgO and SiO₂ are roughly correlated with the mafic phenocryst assemblages (figure 8). Phenocryst assemblages of high-SiO₂ and low-MgO lavas from the Tkl 1 is pl + opx + opq ± cpx ± hbl. On the other hand, that of the low-SiO₂ lavas from the Tkl 2 is pl + ol + opq. The least magnesian samples from Rajabasa (Rbs 1 & Rbs 11 in Table 3) contain phenocryst of pl + opx + cpx + opq + bt + hbl, and the phenocryst assemblage of the most magnesian samples (Rbs 2 & Rbs 8) is pl + opx + cpx + opq + ol ± spl. Spinel occurs in Rbs 2, Rb 6, and Rbs 18. Only andesitic samples with SiO₂ above c. 60 wt% contain biotite and hornblende. The occurrence of olivine in Rajabasa is not correlated with whole rock composition as olivine is lacking in some andesite samples (Rbs 1, 7, 9, & 11) but present in more evolved samples (Rbs 10 & Rbs 18) with biotite and hornblende. Olivine crystals in samples with SiO₂ <56 wt% and MgO ≥6 wt% (Rbs 2 & Rbs 8) are up to 1.9 mm in size and prevalent, whereas the olivine in samples with SiO₂ >56 wt% is < 0.7 mm in size and sporadic. Basaltic andesite from Rbs 2 is higher in MgO than that of basalt from Rbs 8. Compared to the less magnesian samples, the high MgO samples have more clinopyroxene than orthopyroxene.

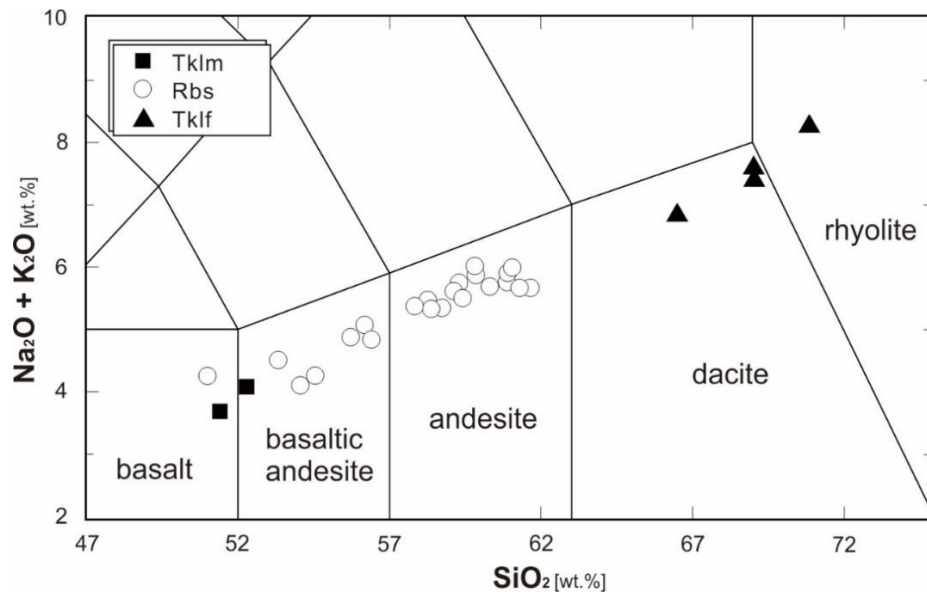


Figure 7. Rock classification using the scheme of Le Bas et al. (1986) based on total alkalis (Na₂O + K₂O wt%) vs silica (SiO₂ wt%) diagram for Tangkil and Rajabasa volcanic rocks. Except for Rbs 8, the majority of the rocks from Rajabasa plot in the basaltic andesite to andesite fields (circle), whereas rocks from Tangkil plot in two cluster ends (rectangle and triangle)

Table 3. Whole rock compositions of Rajabasa (Rbs) and Tangkil (Tkl).

Unit	Rbs 1				Rbs 2		Rbs 6		Rbs 7	Rbs 8	Rbs 9	Rbs 10	
Sample	26.05a	26.05b	21.03	I.22.04	27.03	I.7.10	I.9.04	I.15.01	25.03	I.8.01	I.2.04	I.22.02	I.8.08
<i>Major elements (wt %)</i>													
SiO ₂	59.86	59.30	60.89	61.30	54.54	54.09	59.12	59.43	59.81	51.06	58.39	57.86	60.34
TiO ₂	0.84	0.85	0.81	0.74	0.85	0.80	0.87	0.72	0.83	1.10	0.82	0.96	0.82
Al ₂ O ₃	17.65	17.38	16.81	17.02	16.68	16.82	17.66	17.27	17.21	18.86	17.89	17.56	17.27
FeO*	6.18	6.90	7.23	6.26	7.12	7.56	7.03	6.58	6.96	9.12	7.38	7.84	6.70
MnO	0.12	0.14	0.15	0.13	0.20	0.15	0.15	0.14	0.14	0.18	0.15	0.15	0.14
MgO	2.90	3.08	2.65	2.90	6.12	7.11	3.01	3.39	2.68	5.94	3.09	3.21	2.88
CaO	6.36	6.39	5.50	5.80	10.03	9.14	6.27	6.80	6.06	9.14	6.68	6.78	5.95
Na ₂ O	3.63	3.59	3.37	3.27	2.85	2.79	3.42	3.28	3.81	3.15	3.43	3.53	3.23
K ₂ O	2.25	2.16	2.40	2.40	1.40	1.34	2.21	2.22	2.19	1.12	1.92	1.85	2.45
P ₂ O ₅	0.22	0.21	0.20	0.18	0.19	0.19	0.26	0.17	0.30	0.35	0.24	0.24	0.22
L.O.I.	0.55	0.88	1.65	1.42	0	0.23	0.98	0.93	0.43	1.48	0.91	0.56	1.41
H ₂ O (-)	0.29	0.35	0.71	0.28	0	0.04	0.15	0.18	0.27	0.17	0.12	0.22	0.19
<i>Trace elements (ppm)</i>													
Rb	71	66	79	82	42	40	67	75	68	24	66	55	75
Ba	387	368	432	451	258	283	397	372	401	298	383	319	347
Sr	479	473	416	397	448	412	431	411	493	592	489	470	426
Zr	140	135	138	149	100	100	151	129	160	114	128	133	147
Nb	5	4	5	23	5	19	22	24	7	28	26	14	30
Y	24	22	27	29	36	22	25	23	34	26	27	27	31
Cr	11	13	11	14	250	245	10	30	13	37	7	6	6
Ni	10	10	8	5	114	96	4	13	10	21	2	3	3
V	170	171	164	154	217	210	182	174	146	227	164	206	168

Table 3. Continued

Unit	Rbs 11	Rbs 15	Rbs 16		Rbs 18					Late stage Tangkil Tkl 2/ Tklm			Early stage Tangkil Tkl 1/ Tklf		
Sample	I.21.06	24.06	I.14.03	I.20.08	19.02a (xenolith)	19.02b	I.10.03	23.02	20.02	24.02	24.03	23.03	26.02	I.6.03	18.02
<i>Major elements (wt %)</i>															
SiO ₂	61.67	56.18	55.78	56.42	53.35	61.05	58.70	58.27	60.93	51.41	52.28	66.52	69.03	69.01	70.88
TiO ₂	0.70	0.89	0.94	0.85	1.16	0.78	0.74	0.78	0.76	1.15	1.29	0.54	0.70	0.65	0.56
Al ₂ O ₃	16.93	17.96	18.41	18.14	18.48	16.41	17.67	17.07	16.70	20.06	19.86	15.88	16.11	16.12	16.00
FeO*	6.11	8.09	7.97	8.03	8.46	6.39	6.76	7.00	6.27	9.39	9.41	4.02	3.20	3.27	2.58
MnO	0.14	0.16	0.16	0.16	0.15	0.14	0.14	0.15	0.14	0.16	0.15	0.09	0.09	0.11	0.03
MgO	2.75	3.87	3.74	3.96	4.14	2.89	3.65	4.07	2.83	3.52	2.89	1.83	0.51	0.65	0.14
CaO	5.87	7.57	7.91	7.37	9.56	6.18	6.83	7.03	6.31	10.39	9.78	4.17	2.59	2.63	1.48
Na ₂ O	3.13	3.48	3.15	3.31	3.27	3.55	3.20	3.36	3.50	3.08	3.28	4.13	4.57	4.51	5.35
K ₂ O	2.52	1.59	1.74	1.54	1.24	2.44	2.16	2.11	2.41	0.61	0.80	2.72	3.04	2.88	2.93
P ₂ O ₅	0.18	0.22	0.20	0.23	0.18	0.16	0.16	0.16	0.15	0.23	0.26	0.11	0.16	0.17	0.05
L.O.I.	1.08	0.68	0.80	0.64	0.09	0.66	0.77	0.39	0.56	0.78	1.13	1.55	3.04	2.88	2.22
H ₂ O (-)	0.14	0.28	0.10	0.15	0.20	0.18	0.13	0.30	0.15	0.31	0.46	0.66	0.42	0.23	1.10
<i>Trace elements (ppm)</i>															
Rb	81	44	54	46	23	80	72	68	80	12	24	88	77	74	78
Ba	427	299	287	265	232	422	338	355	397	160	191	386	421	394	493
Sr	411	508	474	474	596	415	409	438	421	489	476	249	244	237	203
Zr	141	117	114	116	83	126	129	128	125	102	127	190	313	310	286
Nb	23	3	23	28	3	4	21	4	3	4	4	5	11	36	8
Y	62	22	27	22	22	22	21	22	21	26	29	23	46	45	30
Cr	9	19	13	14	23	11	32	39	13	41	31	30	10	0	6
Ni	4	14	4	10	10	10	10	18	9	15	10	23	11	5	11
V	157	235	227	211	305	161	185	186	199	262	284	99	39	12	12

The data is normalized to 100% with volatile-free basis.

*Total iron as FeO.

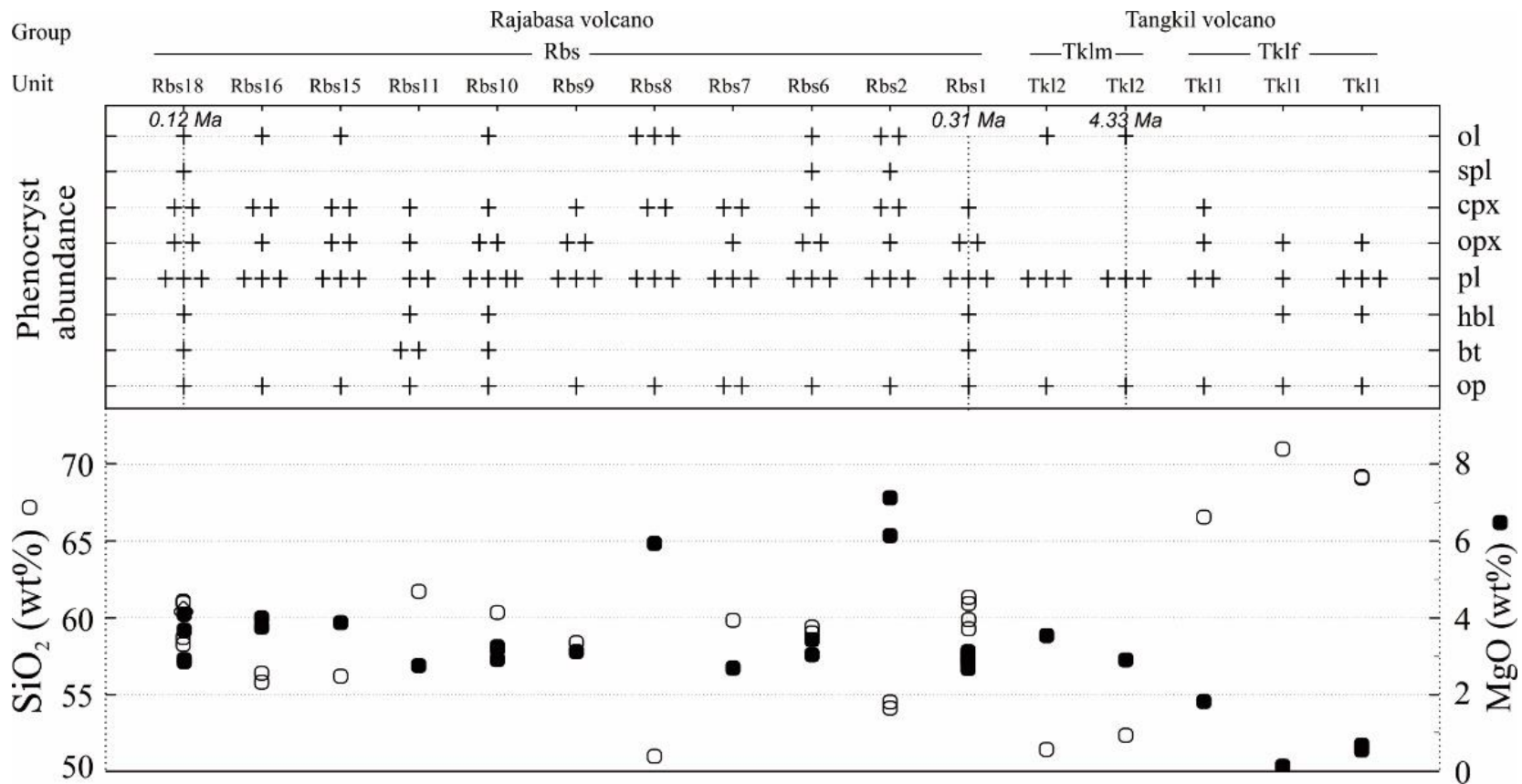


Figure 8. Phenocryst abundance variations in samples from Tangkil and Rajabasa volcanoes. Modal abundance of 0-5%, 5-10%, and 10-30% are indicated by symbol +, ++, and +++, respectively.

Volcanic rocks from Tangkil are classified as medium-K basalt (51-52 wt% SiO₂; Tk_{lm}) and medium- to high-K dacite to rhyolite (67-71 wt% SiO₂; Tk_{lf}), whereas those from Rajabasa are basalt, basaltic andesite, and andesite (51-62 wt% SiO₂; R_{bs}) (figures 7 & 9). The high-SiO₂ samples of R_{bs} are classified as high-K andesite, whereas the low-SiO₂ lavas are either medium-K basalt or basaltic andesite.

Tk_{lf} and Tk_{lm} show discontinuous, separated iron-enrichment trends on the modified Miyashiro diagram (FeO^t/(FeO^t+MgO) vs SiO₂) (figure 9) (Miyashiro, 1974; Gill, 2010). The extrapolations of the trends do not cross as they are subparallel. The two samples from Tk_{lm} show an iron-enrichment which is typical of tholeiitic basalt. Tk_{lf} displays an iron-enrichment trend parallel to the basalt trend and crosses the boundary between calc-alkaline and tholeiitic fields.

R_{bs} show two different trends; one is near-constant FeO^t/(FeO^t+MgO), and the other is a steep iron-enrichment trend. Two samples that are the mafic end of the steep iron-enrichment trend are olivine-rich basaltic andesite samples (R_{bs} 2). The high-silica samples of R_{bs} cluster at an andesite composition, at which the two trends converge.

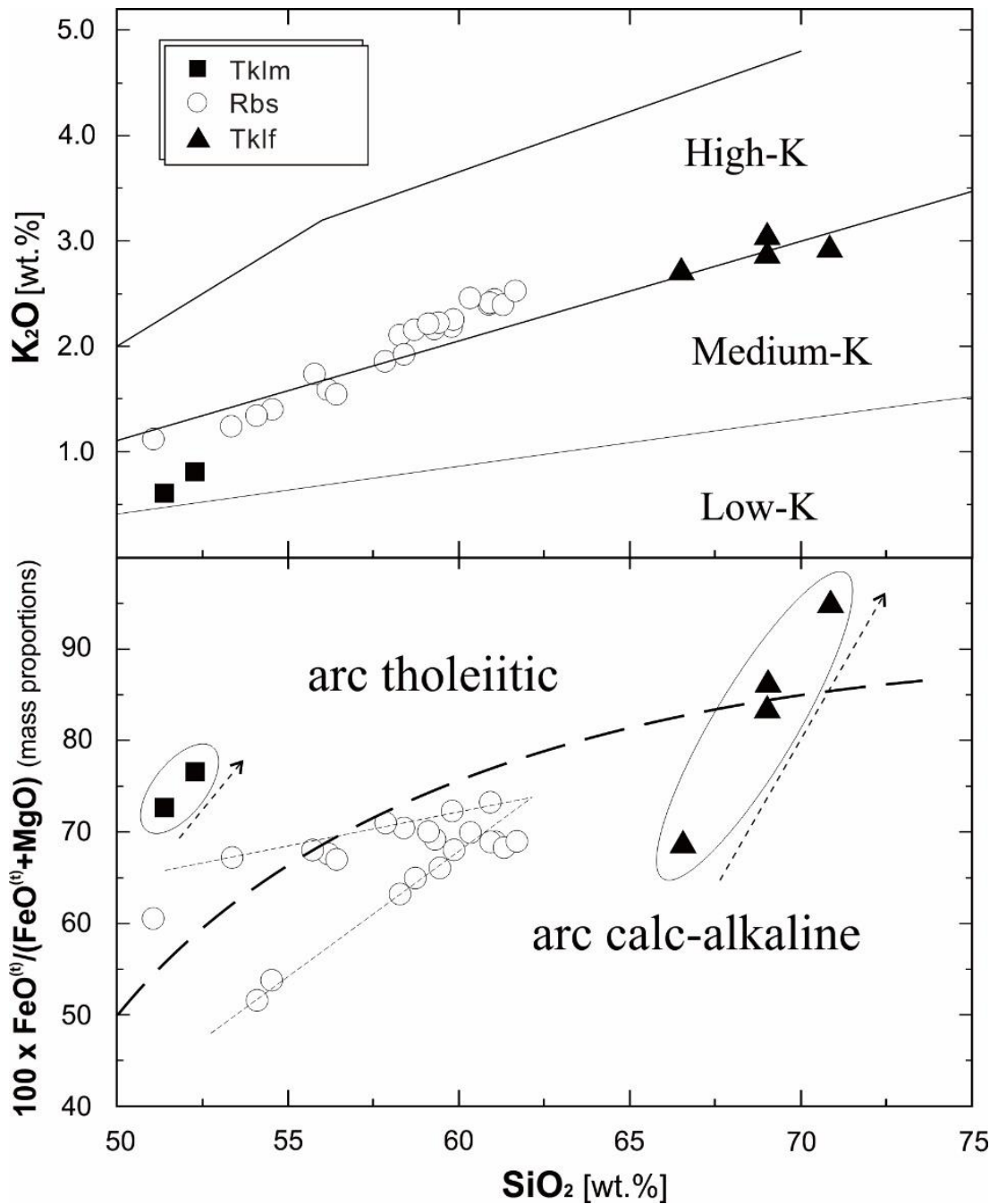


Figure 9. (above) Diagram of silica vs K_2O for the sub-division of the subalkaline series (Le Maitre et al., 1989). Rbs and Tklf rocks are plotted in transition from medium-K to high-K, whereas Tklm rocks plotted in medium-K. (below) A discriminating diagram between tholeiitic and calc-alkaline magma series. The separating line (heavy dashed line) is from Miyashiro (1974) which was later modified by Gill (2010).

Variation diagrams of selected major and minor elements vs. SiO_2 are shown in figure 10. Rocks from Tklf show clear negative correlation of SiO_2 with $\text{FeO}^{(t)}$, MgO , CaO , and Sr and positive correlation with alkali and Ba. The last Tklf sample show the lowest TiO_2 content in the series. On the diagrams of TiO_2 , MgO , Al_2O_3 vs SiO_2 , Tklf trend is not continuous with Tkml trend. Rocks from Tkml show positive silica correlation with TiO_2 and negative silica correlation with MgO , CaO , and Al_2O_3 . Tkml samples are lower in MgO than the basalt samples of Rajabasa. Rocks from Rajabasa show positive correlations in alkali, Rb, Ba, and Zr and negative correlations in TiO_2 , $\text{FeO}^{(t)}$, MgO , CaO , Al_2O_3 , and Sr against silica.

The silica-variation plots of MgO , Al_2O_3 , and Sr show two different trends which converge at *c.* 62 wt% SiO_2 . Two olivine-rich basaltic andesite (Rbs 2) plot at the high- MgO end of the trend on MgO vs. SiO_2 diagram. In addition, they plot off lower the other trend of TiO_2 , $\text{FeO}^{(t)}$, Al_2O_3 , and Sr . Except for these basaltic andesite samples, Ni and Cr are as low as 8-23 ppm and 6-41 ppm, respectively. These two samples are extraordinarily high in Ni (*c.* 95 - 114 ppm) and Cr (*c.* 250 ppm), which are higher than those of basalt samples from Rbs and Tkml.

The contents of Ni and Cr from the last Tklf sample (67 wt% SiO_2) are the highest in the series. Furthermore, the content of Ni is slightly higher than samples of Tkml and Rbs except for the two high- MgO samples from Rbs 2. On the diagrams of K_2O vs MgO and Rb vs Cr, two linear trends of Rbs converge at *c.* 2.7 wt% K_2O at the lowest MgO of 2.2 wt% and at *c.* 83 ppm Rb at the lowest Cr of 5 ppm (figure 11).

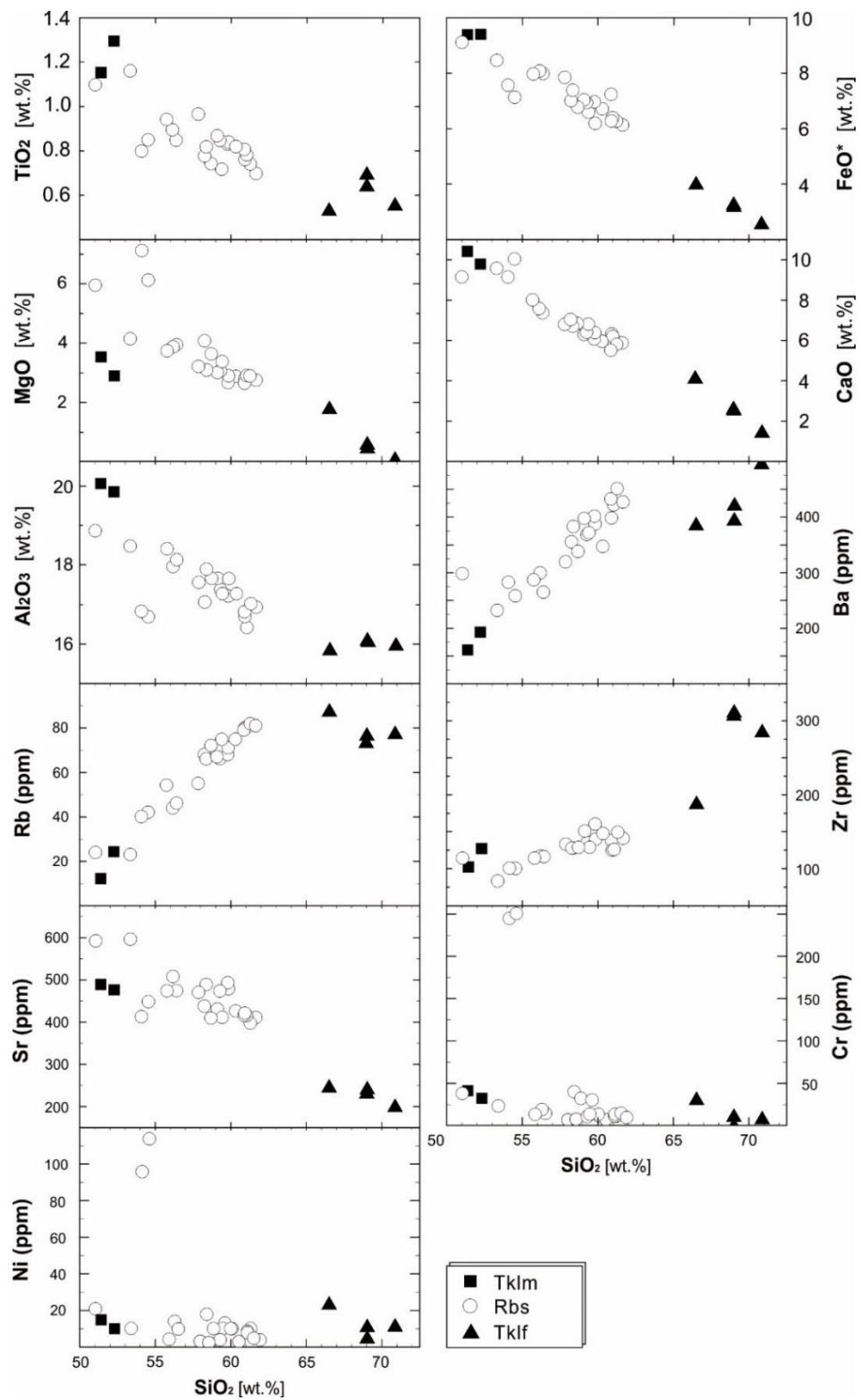


Figure 10. Variation diagrams of SiO_2 (wt.%) vs. selected major and minor elements (ppm) for Tangkil and Rajabasa volcanic rocks.

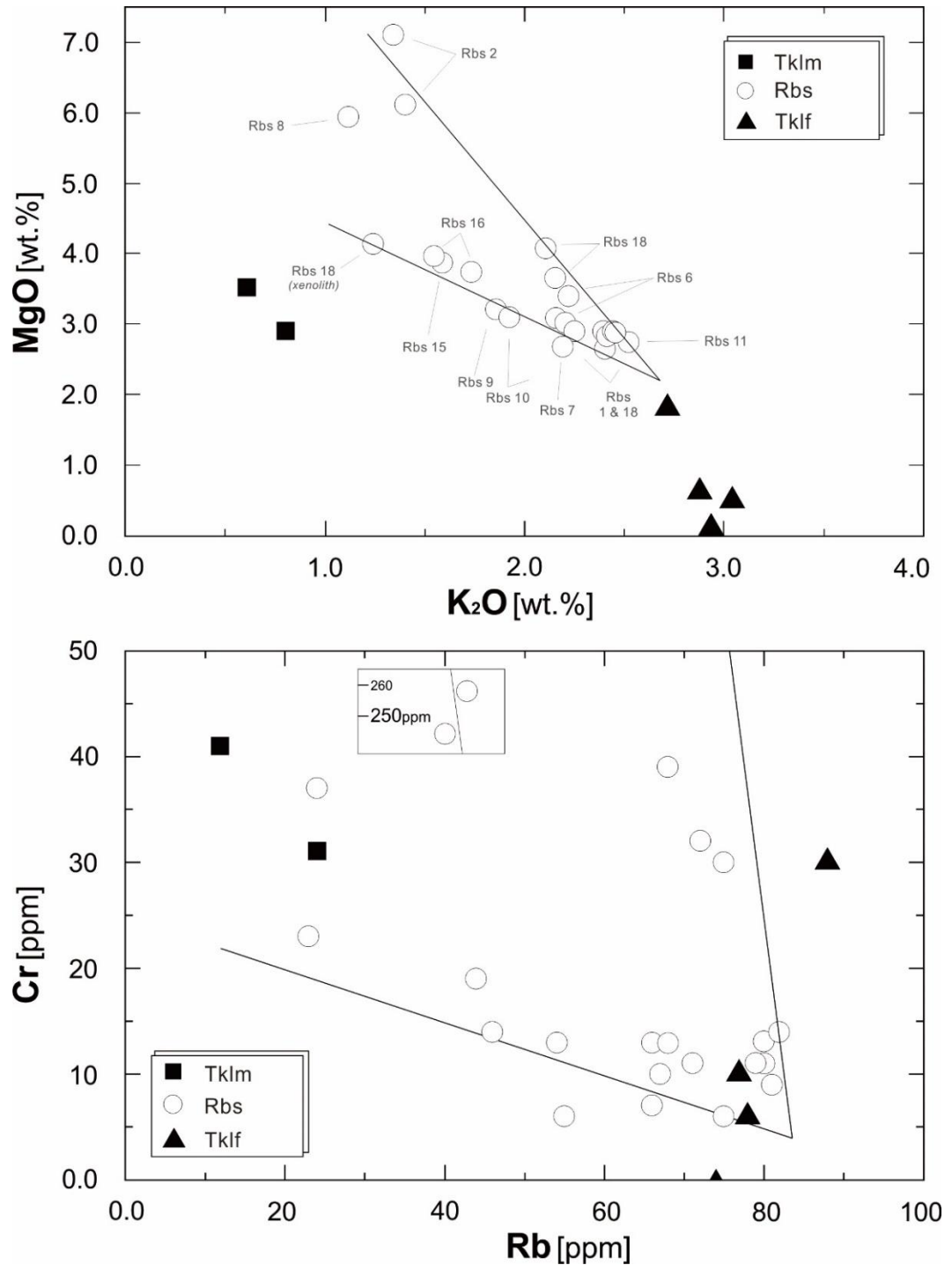


Figure 11. Tangkil and Rajabasa volcanic rocks plotted in K₂O vs MgO and Rb vs Cr. The diagrams display two discontinuous trends from Tangkil volcano, which are not parallel with Rajabasa trends. Meanwhile, Rajabasa volcano depicts two trends that converges from high-Mg and low-Mg basalt composition to andesitic composition.

4.4 TEMPORAL CHEMICAL VARIATIONS

The temporal chemical variation of Tangkil and Rajabasa is shown in figure 12. The equivocal order of two flow units is depicted in temporal chemical variations with the parallel ages (Rbs 1 – Rbs 2; Rbs 7 – Rbs8; Rbs 9 – Rbs 10). Before *c.* 4.3 Ma, Tangkil volcano was initiated by the eruption of dacite and rhyolite lavas (Tklf). In this period, SiO₂ and Na₂O+K₂O initially increased, and then, decreased. Opposite trends are apparent in CaO and MgO. At *c.* 4.3 Ma, Tangkil volcano changed its eruption products from dacite/rhyolite to basalt (Tkml). The two samples from Tkml show a slight increase in CaO and MgO and a decrease in SiO₂ and Na₂O+K₂O. The Al₂O₃ contents from Tklf and Tkml do not change through time, 16 wt% and 20 wt%, respectively.

Then at *c.* 0.31 Ma, Rajabasa volcano started its activity by erupting basaltic andesite and andesite of which SiO₂ fluctuates from 54 wt% to 62 wt%. The majority of Rbs shows rising-falling variation in SiO₂ and MgO. The concentrations of Na₂O+K₂O comply with SiO₂, whereas those of CaO, MgO, and Al₂O₃ are contrary. Basaltic andesite and basalt are marked with spikes of CaO (9.1-10 wt%) and MgO (5.9–7.1 wt%) while differentiated andesite are produced constantly. The lavas with high-Mg basaltic andesite and basalt composition (Rbs 2 and Rbs 8) are olivine-rich rocks and originated from older Balerang cone. These Mg-rich rocks are intercalated with the differentiated andesite.

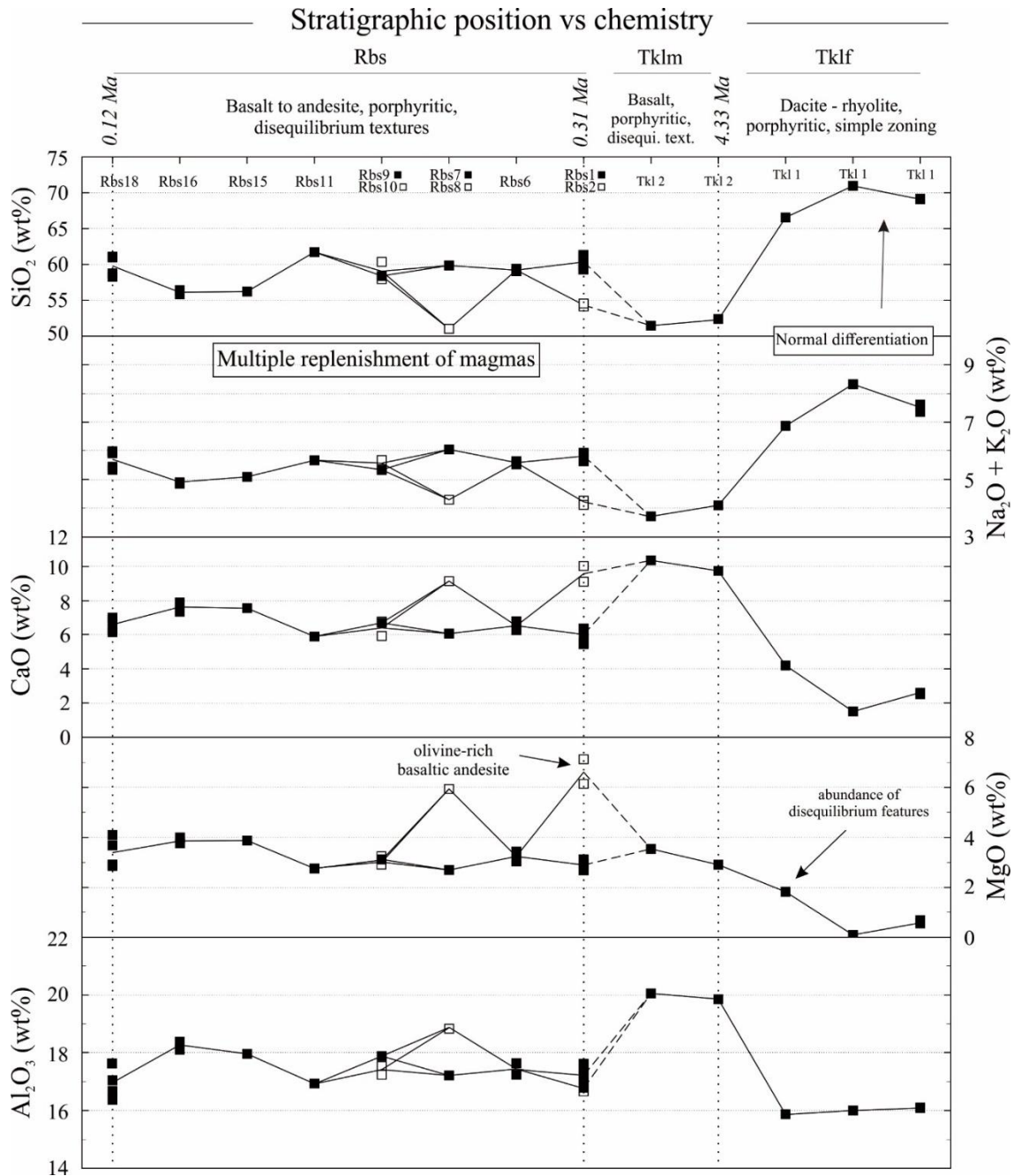


Figure 12. Temporal chemical variation of Tangkil and Rajabasa volcanic rocks. Total alkalis (Na₂O+K₂O) composition trend complies with silica (SiO₂), whereas CaO, MgO, and Al₂O₃ do not follow silica composition trend. All samples composition for each unit are plotted; continuous lines are running average from all sample in each unit to show the trend of the data.

4.5 PETROGRAPHY

4.5.1 Textures

To understand the origin of phenocrysts, lavas from Tangkil and Rajabasa volcanoes are furtherly divided into three and four series, respectively. Three series in Tangkil are Tklf, last Tklf, and Tkml; four series in Rajabasa are high-Mg basaltic andesite, low-Mg basaltic andesite, andesite, and transitional basalt. Series of last Tklf, high-Mg basaltic andesite, low-Mg basaltic andesite, and andesite are distinguished with series of Tklf, Tkml, and transitional basalt based on petrographic characteristics.

Last Tklf, high-Mg basaltic andesite, low-Mg basaltic andesite, and andesite

The last Tklf series is the youngest and the least evolved sample from Tangkil felsic rocks (figure 9). High-Mg basaltic andesite and low-Mg basaltic andesite series are the samples plotted along the steep iron-enrichment trend and the near-constant trend, respectively. Andesite series is the most evolved samples from Rajabasa, where the two trends converge at.

The samples show porphyritic texture with the phenocryst abundance ranging from 38 to 51 vol. %. Phenocrysts of plagioclase, orthopyroxene, clinopyroxene, and Fe-Ti oxides are abundant in all samples (figure 13). Additionally, some of the samples alternatively contain either a combination of biotite \pm hornblende or olivine \pm spinel as phenocrysts. Phenocryst minerals occur both as discrete crystals and glomeroporphyritic aggregates. The most common aggregates comprise orthopyroxene, clinopyroxene, plagioclase, and opaque minerals with additional of olivine, biotite, or hornblende. The groundmass texture is homogeneous and comprises plagioclase, orthopyroxene, augite, apatite, opaque, and minor glass.

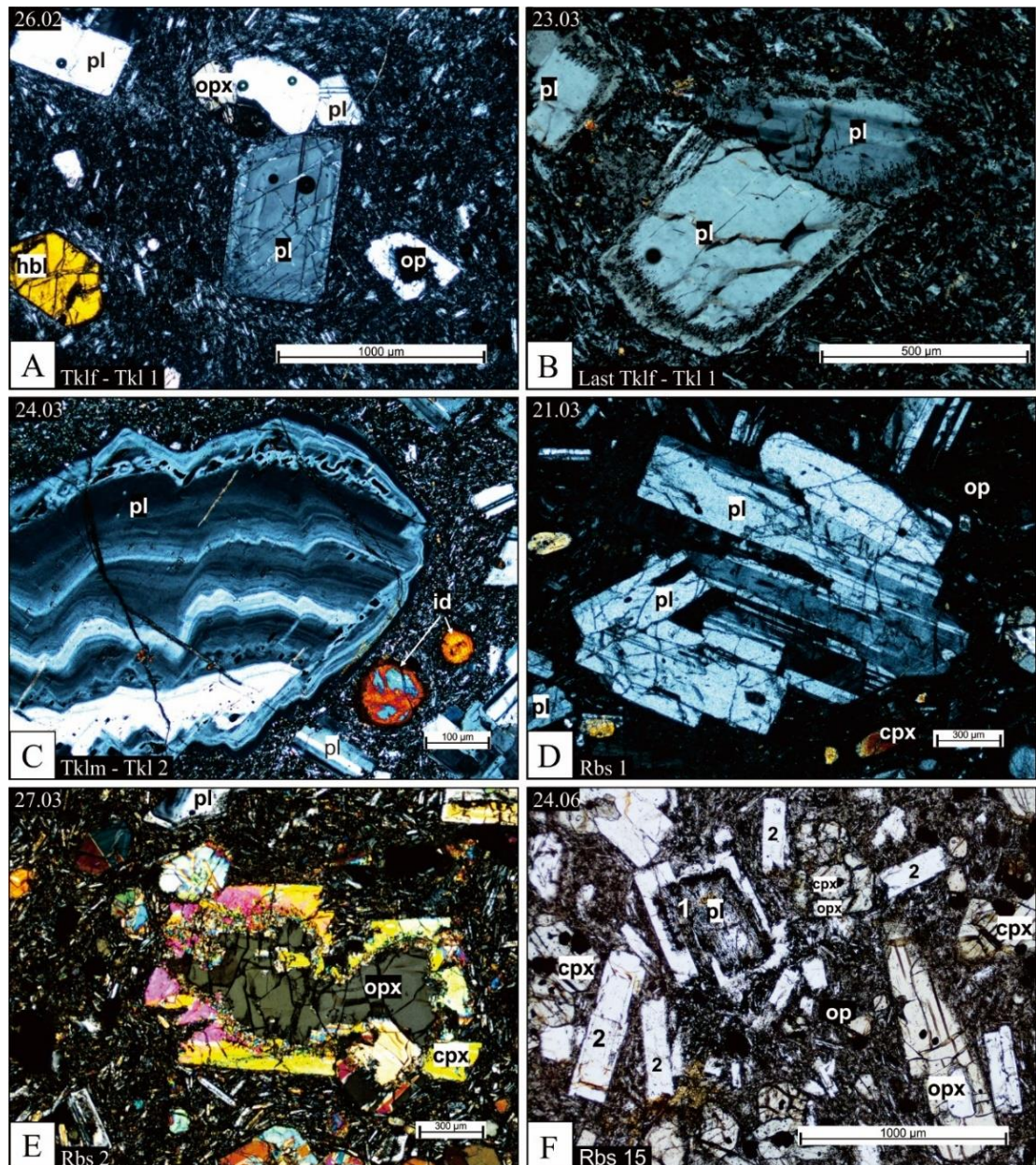


Figure 13. Representative crossed polar microphotographs of: **A)** Euhedral phenocrysts of plagioclase, fresh amphibole, and pyroxene. **B)** Subhedral plagioclase containing cellular zones in the margin of crystals **C)** Plagioclase with complex zoning and iddingsite which altered olivine. **D)** An aggregate of plagioclase phenocrysts and discrete augite crystals. **E)** Orthopyroxene mantled by clinopyroxene rim. Melt inclusions developed in resorption boundary between the 2 phases. **F)** The phenocrysts assemblages in Rbs, containing spongy cellular or sieved plagioclase crystals (type 1) and “clear” plagioclase crystals (type 2).

Plagioclase phenocrysts show subhedral to euhedral shape and the maximum crystal size is 4.3 mm. The phenocrysts are characterized by clear crystal and the presence of complex zoning and resorption textures. Resorption textures are common, shown by the unconformable or irregular surfaces between Ca-poor core and Ca-rich mantle (figure 14a) or the anhedral inner part, which is dissected by a sharp boundary, dissecting the growth bands discordantly (figure 14b). Reversely zoned plagioclase contains a subhedral Ca-poor core that is overgrown by a Ca-rich mantle (figure 15). In addition to the resorbed cores, the patchy-zoned cores and clear cores are also common. Coarsely spongy cellular zones showing resorption channels which typically occupy the entire crystal from core to rim, whereas finely spongy cellular zones (also termed as “sieved”) are overgrown by a clear and zoned rim with thickness up to 0.1 mm. Melt inclusions in the resorption channels or sieved zone commonly include glass, pyroxene, and oxide minerals. In some crystals, patchy texture is exhibited in sieved region. Complex oscillatory zoning shows multiple growth zones that are separated by high Ca/Na bands (figures 14c and 16). From core, the Ca/Na decreases outward, abruptly increases, and gradually decreases again toward the next growth band. The multiple growth zones do not develop in other minerals.

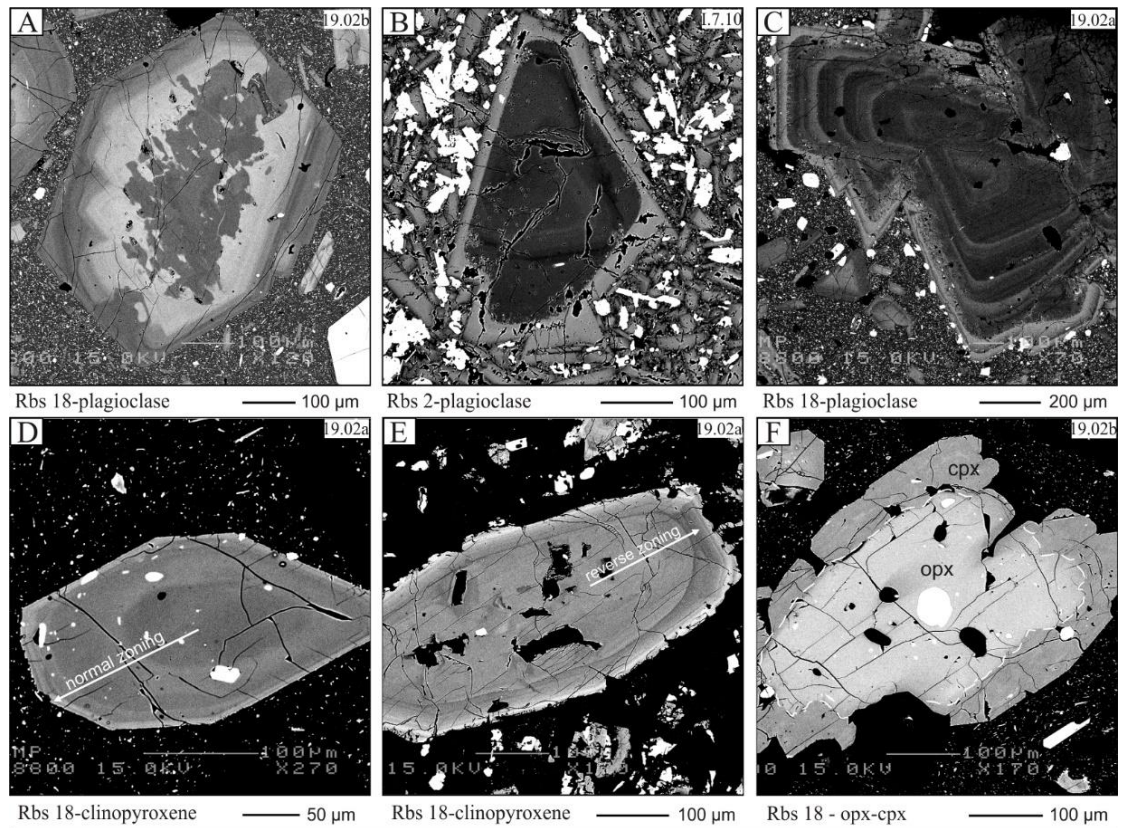


Figure 14. Back-scattered electron images of phenocrysts showing textures and compositional differences. **A)** Resorbed core with calcic-rich mantle (light shade) in plagioclase. **B)** The inner growth bands are dissected by calcic-rich plagioclase. **C)** Oscillatory (multiple) zoned plagioclase with transition between growth bands bound by calcic-rich and dissolution surfaces. Sieved zoned near the rim contains melt inclusions. **D)** Progressive normal zoning in clinopyroxene. **E)** Reverse step zoning in clinopyroxene. The transition is marked by abrupt increase in Mg# (rounded dark layer) in mantle. Core is embayed and slightly patchy. **F)** Orthopyroxene mantled by clinopyroxene rim. Darker shade in clinopyroxene reflect higher Mg#.

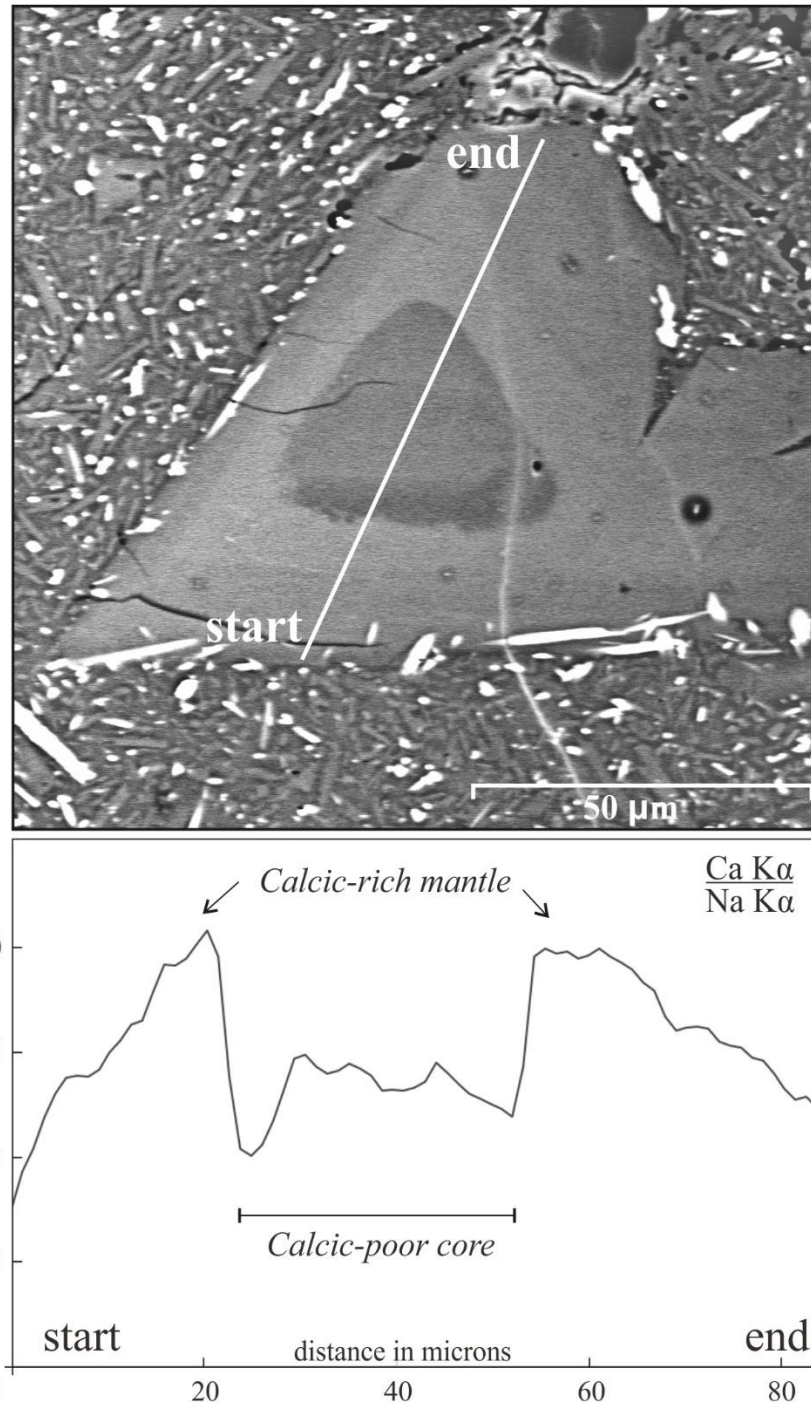


Figure 15. Step reverse zoning shown by plagioclase phenocryst from Rbs samples. Anhedral calcic-poor core (dark shade) mantled by calcic-rich (light shade) plagioclase.



Figure 16. Multiple zones of dissolution-overgrowth in plagioclase crystals.

Orthopyroxene phenocrysts are commonly more abundant and bigger (<1.5 mm) than clinopyroxene (<1 mm). Both homogeneous and zoned pyroxene phenocrysts are present (figures 14d & e). As shown in the back-scattered electron (BSE) image and line scan profiles of augite crystals in an andesite of Rbs 18 (figure 17), some clinopyroxene crystals show reverse zoning with a low Mg/Fe core and a high Mg/Fe rim (spectrum 1), whereas other coexistent clinopyroxene crystals show normal zoning with a high Mg/Fe core and a low Mg/Fe rim (spectrum 2). The BSE image (figure 14e) shows a step reverse zoning in augite of which the composition sharply changes from the Fe-rich core (low Mg/Fe) to the Mg-rich (high Mg/Fe) mantle. The Fe-rich cores are anhedral with rounded and embayed characteristics. By contrast, rounded and embayed cores do not occur in normally zoned clinopyroxene

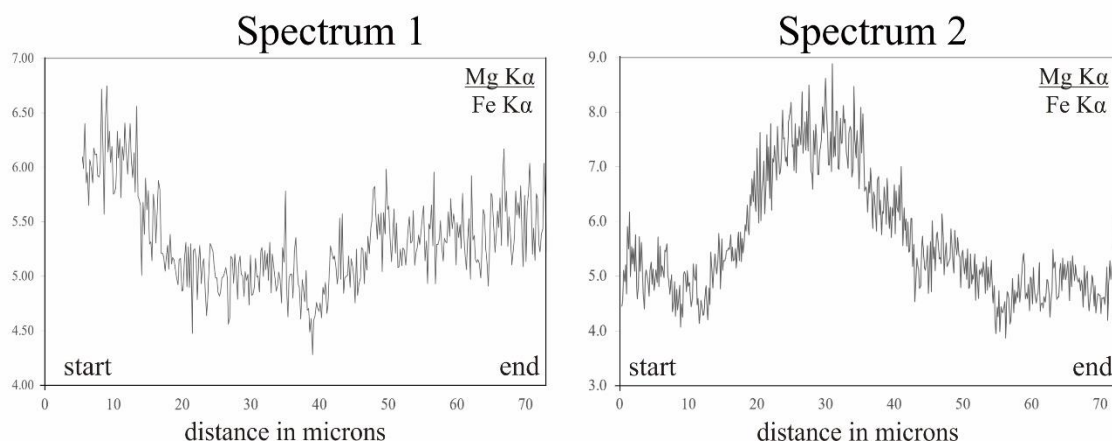
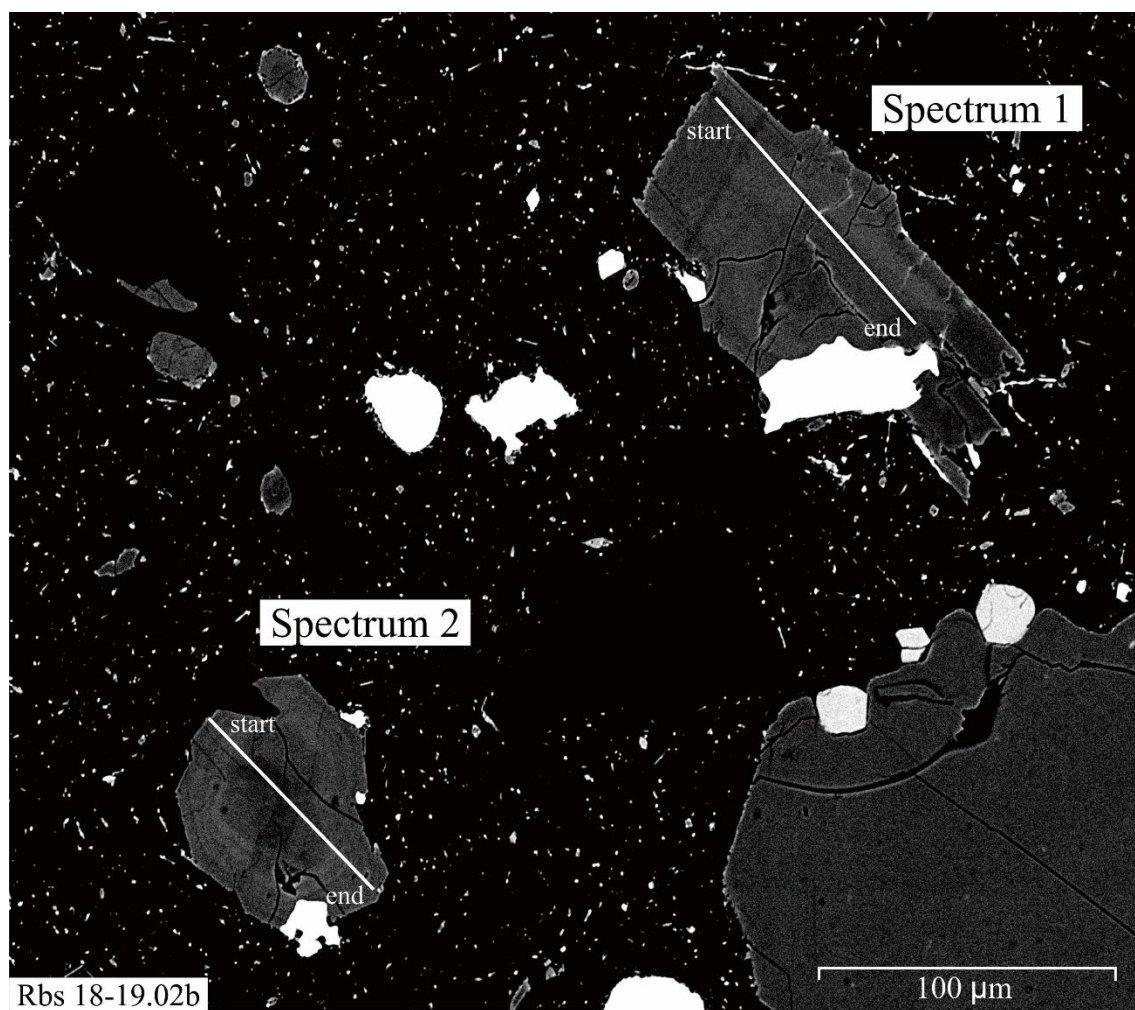


Figure 17. Reverse (spectrum 1) and normal zoning (spectrum 2) exemplified by clinopyroxene phenocrysts in Rbs and last Tklf samples. In spectrum 1, 10 μm wide growth band at rim of crystal is identified, whereas in spectrum 2 *c.* 20 μm wide of high Mg in core of crystal. Line scan resolution is 512 x 384, map dwell 500 μs , and time/frame 98.3 s.

(figure 14d). The occurrence of orthopyroxene phenocrysts that are mantled by clinopyroxene (augite) rim (figure 14f) is prevalent in the olivine-rich basaltic andesite samples (Rbs 2 in Table 3). The interfaces between two minerals often seamless without presence of inclusions.

Olivine crystals vary in size from 0.1 mm to 1.9 mm. Most olivine phenocrysts are subhedral to euhedral. The smaller, the more rounded the olivine crystals are. Olivine occurs as discrete crystals but in some cases as aggregates with clinopyroxene and plagioclase.

Tklf, Tkml, and transitional basalt

Tklf and Tkml series are the three most evolved lavas from Tangkil felsic rocks and the two basaltic lavas from Tangkil mafic rocks, respectively. Transitional basalt series is the least evolved lava from Rajabasa, plotted in between the steep and near-constant iron-enrichment trends in Miyashiro diagram (figure 9).

Tklf are slightly porphyritic dacite containing phenocrysts of plagioclase, orthopyroxene, and Fe-Ti oxides (figure 13). Tkml are porphyritic basalt containing phenocrysts of plagioclase, Fe-Ti oxides, and olivine that replaced by iddingsite (figure 13). Transitional basalt is porphyritic basalt containing phenocrysts of plagioclase, Fe-Ti oxides, clinopyroxene, and olivine. Phenocryst minerals occur only as discrete crystals, or glomerocrysts are not common. These phenocrysts embedded in a groundmass containing plagioclase, augite, pigeonite, opaque minerals, and glass.

Plagioclase phenocrysts in these samples are euhedral to subhedral and smaller than 2.5 mm. Tklf samples mostly containing clear, homogeneous, and slightly zoned plagioclase crystals. Plagioclase crystals in Tkml and transitional basalt samples

consisting of clear cores and clear overgrowth rims, with or without dusty mantle. The plagioclase crystals without sieve textures are commonly smaller (< 1.8 mm) than plagioclase with sieve textures. Oscillatory zoning which is developed in mantle or rim with subtle amplitude (less than An_5 mol.%) is common.

Clinopyroxene and orthopyroxene phenocrysts are clear, euhedral to subhedral. Augite crystals in transitional basalt sample are larger (~ 3.4 mm) than enstatite crystals in Tklf samples (< 0.8 mm). Augite crystals are slightly zoned, while enstatite crystals are mostly homogeneous and few normally zoned. The phenocrysts of clinopyroxene do not coexist with orthopyroxene.

4.5.2 Mineral chemistry

Plagioclase

For Tangkil, the plagioclase phenocrysts in last Tklf series exhibit normal and reverse zoning, and only normal zoning in Tkln (figure 20). The last Tklf series contain normally zoned plagioclase with cores of An_{86-91} and the other is normal and reversely zoned with cores of An_{30-44} . Figure 18a shows two distinct plagioclase compositions, calcic plagioclase and sodic plagioclase, within a sample. Calcic plagioclase usually shows embayed cores, and the embayment disappears in lower anorthite mantle part. Rims of some low anorthite cores are similar in composition (An_{64} to An_{71}) with rims of high anorthite cores. The exterior of sodic core is resorbed (sieved) and mantled with calcic plagioclase. The Tklf mostly containing normally zoned and homogeneous plagioclase with cores composition range from An_{30} to An_{54} . Some plagioclase with cores lower than An_{40} , however, show slightly higher anorthite rim, which means reversely zoned. Crystal clots of plagioclase (An_{55} core; An_{39} rim)

are similar in composition with the discrete phenocrysts (figure 19). Some mantle and rim parts show oscillatory zoning with low amplitude (less than An_5 mol.%) (figure 21). On the other hand, the cores of normally zoned plagioclase in Tklm exhibit widely varying compositions of An_{54-91} with rims compositions of An_{47-49} or An_{55-58} . High anorthite cores and low anorthite rims plagioclase usually contains sieve or patchy mantles (figure 21).

For Rajabasa, the plagioclase phenocrysts in all series exhibit normal and reverse zoning, except for the only normal zoning in transitional basalt series (figure 23). The high-Mg and low-Mg basaltic andesite series contain normally zoned plagioclase with cores of An_{83-90} and An_{70-78} , respectively; whereas the reversely zoned with cores of $An_{<53}$. Compared to high-Mg basalt, the composition of calcic plagioclase phenocrysts from low-Mg basalt is less anorthite and that of sodic plagioclase is about the same. Rim compositions of normally zoned plagioclase in the two series are similar with the core compositions of the reverse zoning, and vice versa. Plagioclase in andesite series show normal zoning with cores of $An_{\sim 90}$ and An_{66-79} and also reverse zoning with cores of An_{40-56} . The cores of normal zoning in andesite series are similar in composition with the calcic cores from high-Mg basalt (An_{83-90}) and low-Mg basalt (An_{73-78}). The compositions of the reversely zoned sodic plagioclase cores from andesite series are similar with the reversely zoned sodic plagioclase cores from high-Mg basalt and low-Mg basalt series ($An_{\sim 56}$). These all series also contain homogeneous plagioclase phenocrysts. On the other hand, plagioclase in transitional basalt series contain only normally zoned plagioclase with varying composition of An_{66} to An_{91} . Rim compositions vary from An_{45} to An_{70} . The compositions between

cores and rims are distinct. The petrographic characteristics of plagioclase crystals are summarized in figure 22.

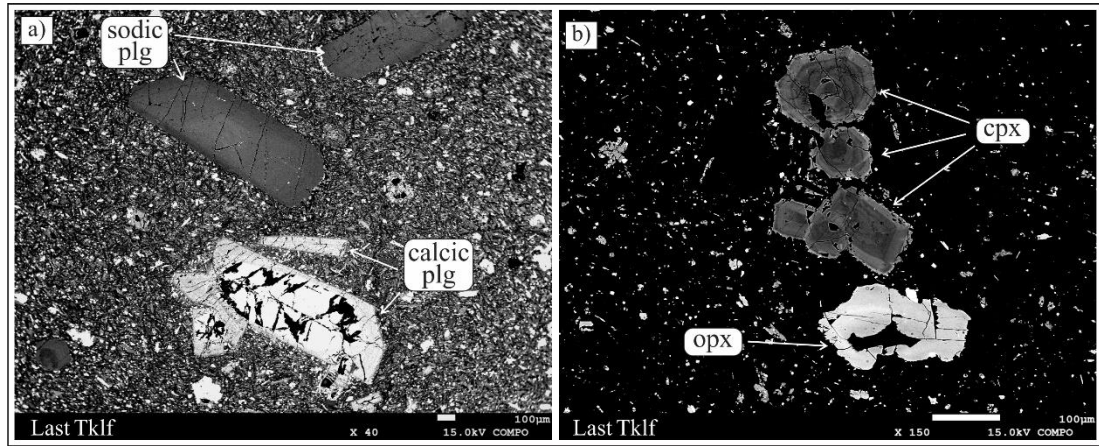


Figure 18. An BSEI image showing bimodal compositions in plagioclase (a) and pyroxene (b) phenocrysts from last Tklf samples.

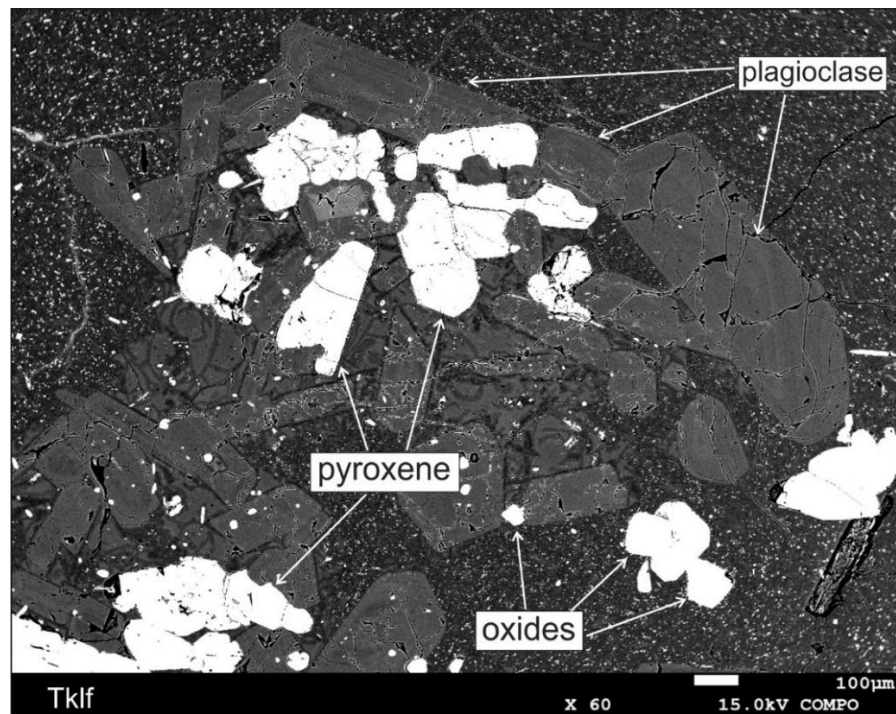


Figure 19. An BSEI image showing crystal clots in Tklf samples. The clots contain plagioclase (An_{39-55}), enstatite (Mg_{66}), magnetite, and glass.

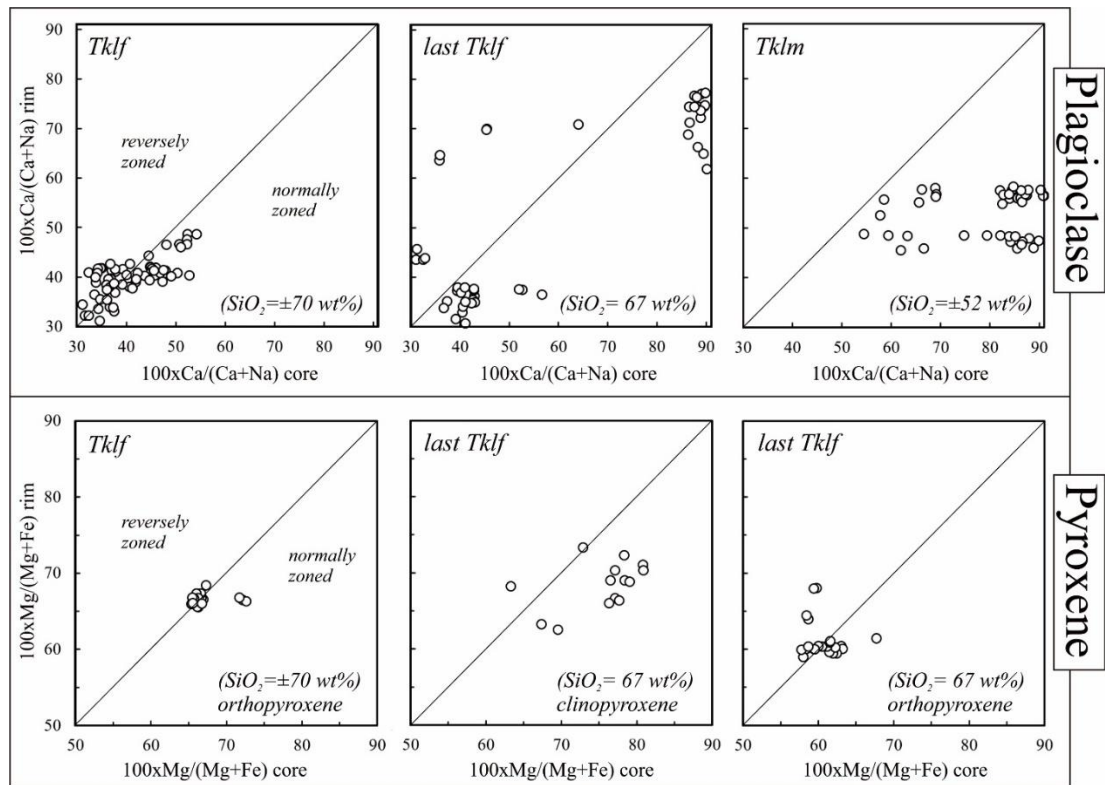


Figure 20. Core-rim relationship of An-number [100xCa/(Ca+Na)] and Mg-number [100xMg/(Mg+Fe)] in plagioclase and pyroxene phenocrysts in Tangkil samples.

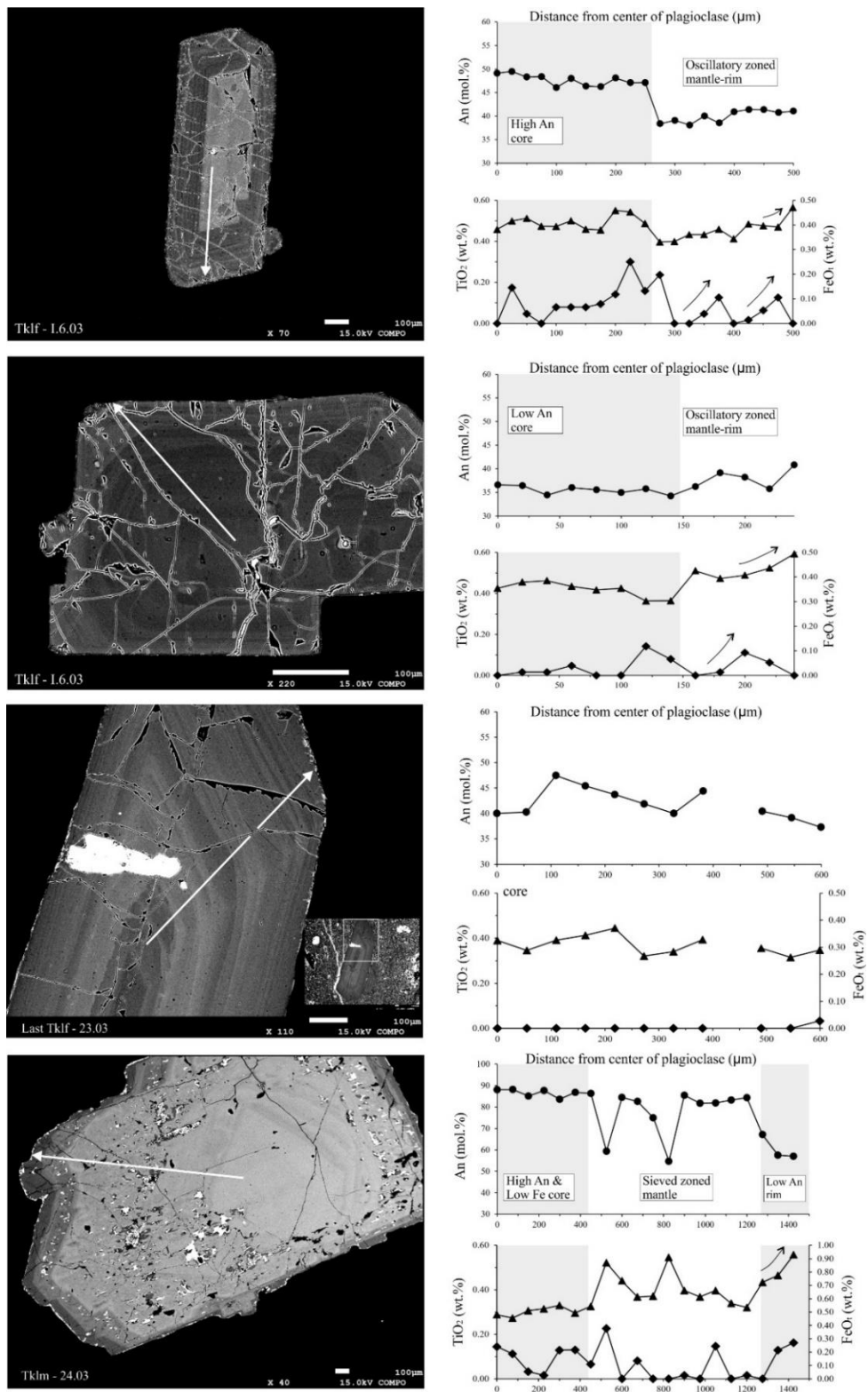


Figure 21. Profiles of electron microprobe traverse of plagioclase crystals from Tangkil. The compositions of An-number, TiO₂, and FeO^(t) are shown. The Tklf contain oscillatory zoning plagioclase with low amplitude.

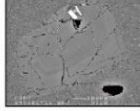
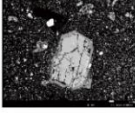
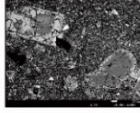
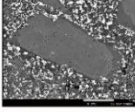
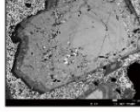
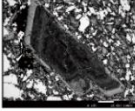
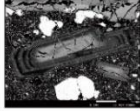
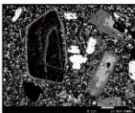
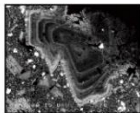
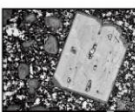
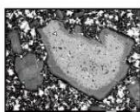
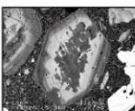
	Series	Characteristics		
Tangkil	Tklf	<ul style="list-style-type: none"> Crystals are clear and show euhedral to subhedral faces Most of crystal are homogeneous or slightly zoned Some show oscillatory zoning with subtle amplitude 		
	last Tklf	<ul style="list-style-type: none"> Resorbed and sieved low-An core is overgrown by high-An rim Calcic plagioclase crystals are euhedral Contains resorbed cores and cellular zones by An-rich clear rim 		
	Tklm	<ul style="list-style-type: none"> Subhedral crystals show resorption like rounded edges and sieved Calcic cores contain dusty zone, patchy zone, and clear crystal. Clear calcic cores mantled by patchy and sieved zoned plagioclase 		
Rajabasa	High-Mg basaltic andesite	<ul style="list-style-type: none"> Low-An concentric zoning is dissected by calcic rim The outer band of low-An core is resorbed, overgrown by An-rich Calcic plagioclase crystals are euhedral Multiple zones of dissolution-overgrowth texture 		
	Low-Mg basaltic andesite	<ul style="list-style-type: none"> Low-An concentric zoning is dissected by calcic rim Calcic plagioclase crystals are euhedral High-An cores are usually patchy (sodic An₅₂₋₅₂) and corroded Multiple zones of dissolution-overgrowth texture 		
	Transitional basalt	<ul style="list-style-type: none"> Sodic plagioclase (An₆₅₋₇₀) shows oscillatory zoning Sieved calcic cores mantled by sodic (An₆₅₋₇₀) oscillatory zoning Clear calcic cores are euhedral, rimmed with normal zoning 		
	Andesite	<ul style="list-style-type: none"> Complex zoning, where cores are diverse in composition Sodic cores are resorbed, overgrown by calcic plagioclase Multiple zones of dissolution-overgrowth texture 		

Figure 22. Summary of textural and compositional characteristics in plagioclase crystals from all series.

Pyroxenes

The discrete pyroxenes phenocrysts in all series show the coexistence of normal and reverse zoning, except for the homogeneous or slight zoning in Tklf and transitional basalt series (figures 20 and 23). In the last Tklf series, the reversely zoned augite cores are Mg₆₃, and the normally zoned augite cores are Mg₆₇₋₈₂. The normally zoned augite is more common than reversely zoned augite. Enstatite phenocrysts show a cluster in Mg₅₈₋₆₄ cores, with rim compositions varies (Mg₅₈₋₆₈). The Tklf series contain homogeneous enstatite (Mg₆₄₋₆₈) and does not contain clinopyroxene. Crystal clots of enstatite (Mg₆₆) are similar in composition with the discrete phenocrysts (figure 19).

A wide variation of compositions is exhibited in pyroxene phenocrysts from high-Mg basaltic andesite, low-Mg basaltic andesite, and andesite series (figure 23). In high-Mg basaltic andesite, pyroxene phenocrysts include diopside (Mg₈₂₋₈₇ core) and augite (Mg₇₃₋₈₄ core), and homogeneous enstatite (Mg₆₃₋₇₁ core). Most of diopside exhibits normal zoning, while augite shows reverse zoning. Some diopside and augite phenocrysts show homogeneous composition. In low-Mg basaltic andesite, augite crystals show both normal and reverse zoning, with the most magnesian cores are Mg₇₅₋₇₈. Enstatite crystals show only reverse zoning (Mg₆₂₋₇₃ core). In andesite, augite is homogeneous (Mg₇₅₋₇₇), which is similar in composition with augite phenocrysts from high-Mg basaltic andesite and low-Mg basaltic andesite. Likewise, the compositions of reversely zoned enstatite (Mg₆₁₋₆₉) are similar with enstatite compositions from the two series. The enstatite also shows normal zoning (Mg₆₈₋₇₆ core). In transitional basalt, augite crystals are slightly zoned, with composition close to Mg_{~75}.

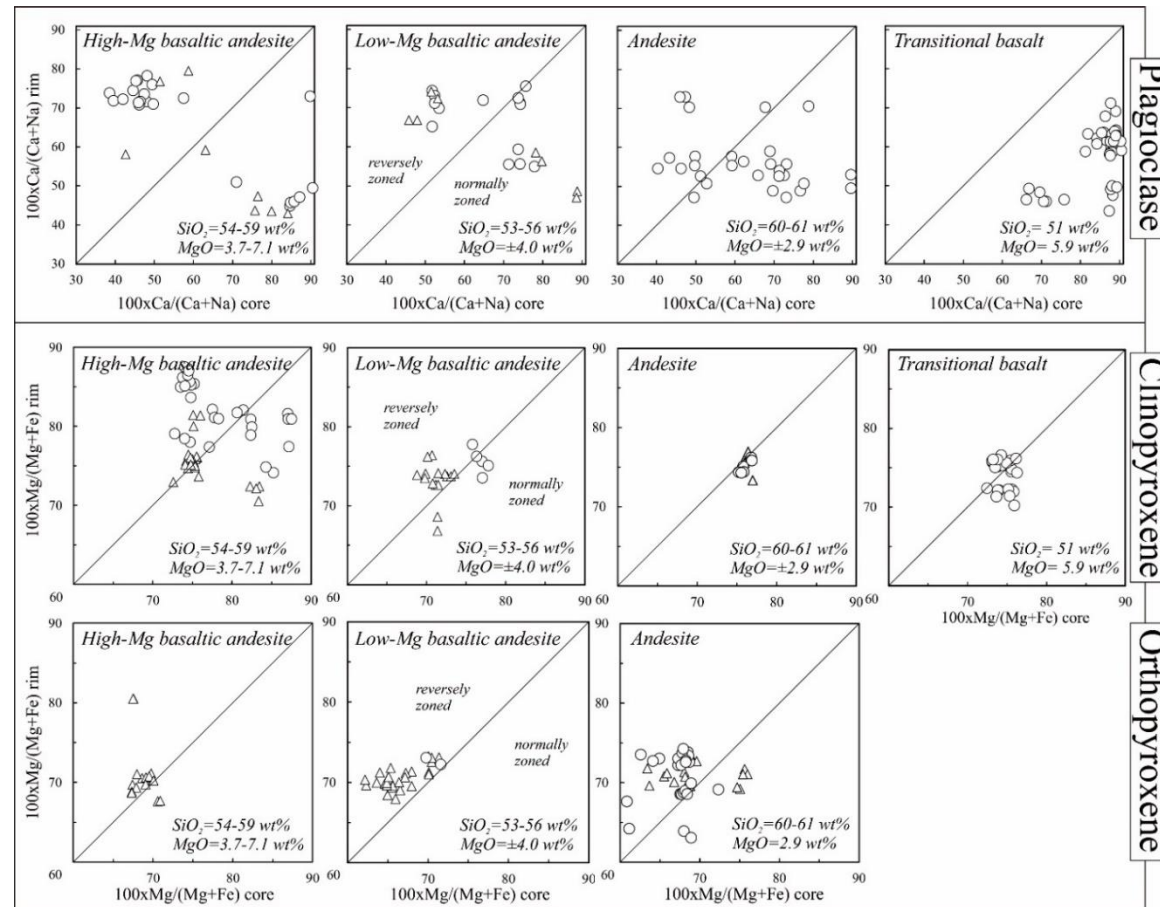


Figure 23. Core-rim relationship of An-number [100xCa/(Ca+Na)] and Mg-number [100xMg/(Mg+Fe)] in plagioclase and pyroxene phenocrysts in Rajabasa samples. Symbol of triangle (Δ) is for more evolved sample from the series.

Orthopyroxene mantled by clinopyroxene

The core-rim compositional variations are indicated in orthopyroxene mantled by clinopyroxene crystals (figure 24). This texture occurred in all Rajabasa series samples (high-Mg basaltic andesite, low-Mg basaltic andesite, andesite) but transitional basalt samples. High-Mg basalt samples contain enstatite (Mg_{65-68}) mantled by diopside (Mg_{80-87}) (figure 25). On the other hand, low-Mg basalt and andesite samples contain enstatite (Mg_{68-72}) mantled by augite (Mg_{67-78}) (figure 25). The orthopyroxene core compositions are mostly less magnesian (Mg_{65-72}) than the clinopyroxene mantle compositions (Mg_{67-87}). The clinopyroxene (that mantled orthopyroxene) exhibit various compositions; Mg_{80-87} for high-Mg basaltic andesite and Mg_{74-78} for low-Mg basaltic andesite and andesite series. These compositions are similar with the compositions of the discrete clinopyroxene rims (figure 23).

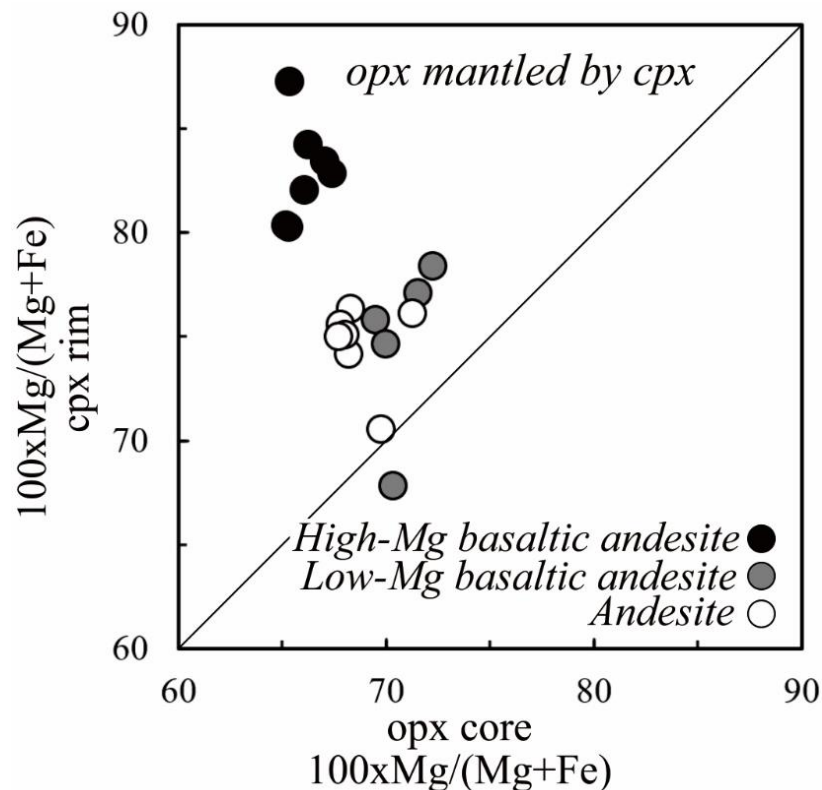


Figure 24. Core-rim relationship in Mg-number [100xMg/(Mg+Fe)] for orthopyroxene mantled by clinopyroxene crystals from three different samples and series in Rajabasa. Orthopyroxene is mostly mantled by more magnesian clinopyroxene.

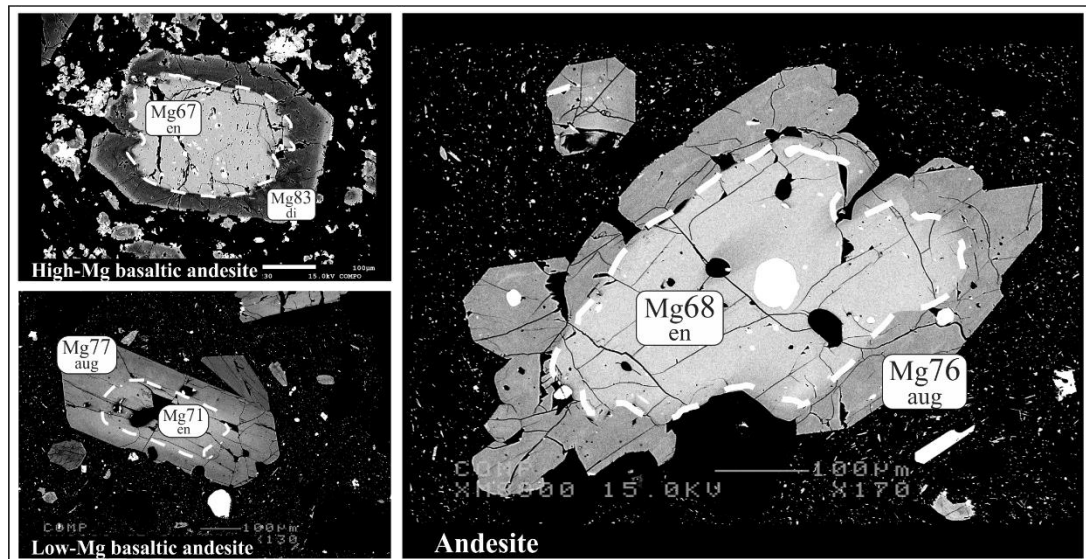


Figure 25. The crystals of orthopyroxene mantled by clinopyroxene as shown in BSEI images. The Mg-number compositional contrast is most evident in high-Mg basaltic andesite samples.

Olivine

Olivine phenocrysts show variations of core-rim compositions in Mg-number and correlated with NiO (figure 26). Olivine phenocrysts show normal zoning with magnesian cores and less magnesian rims. Concentration of NiO in olivine is ~0.32 wt% in high-Mg basaltic andesite, ~0.07 wt% in low-Mg basaltic andesite, and ~0.03 wt% in andesite, from the most to the lowest magnesian cores. Olivine phenocrysts in transitional basalt series contain the lowest magnesian cores (Fo₇₂₋₇₃) with NiO of ~0.08 wt%. High NiO contents in olivine phenocrysts is consistent with the high concentration of Ni (*c.* 95-114 ppm) and Cr (*c.* 250 ppm) in high-Mg basalt rock samples. Some olivine phenocrysts in andesite samples are rimmed by augite with similar Mg-number composition (Fo/Mg₇₃₋₇₄) (figure 27).

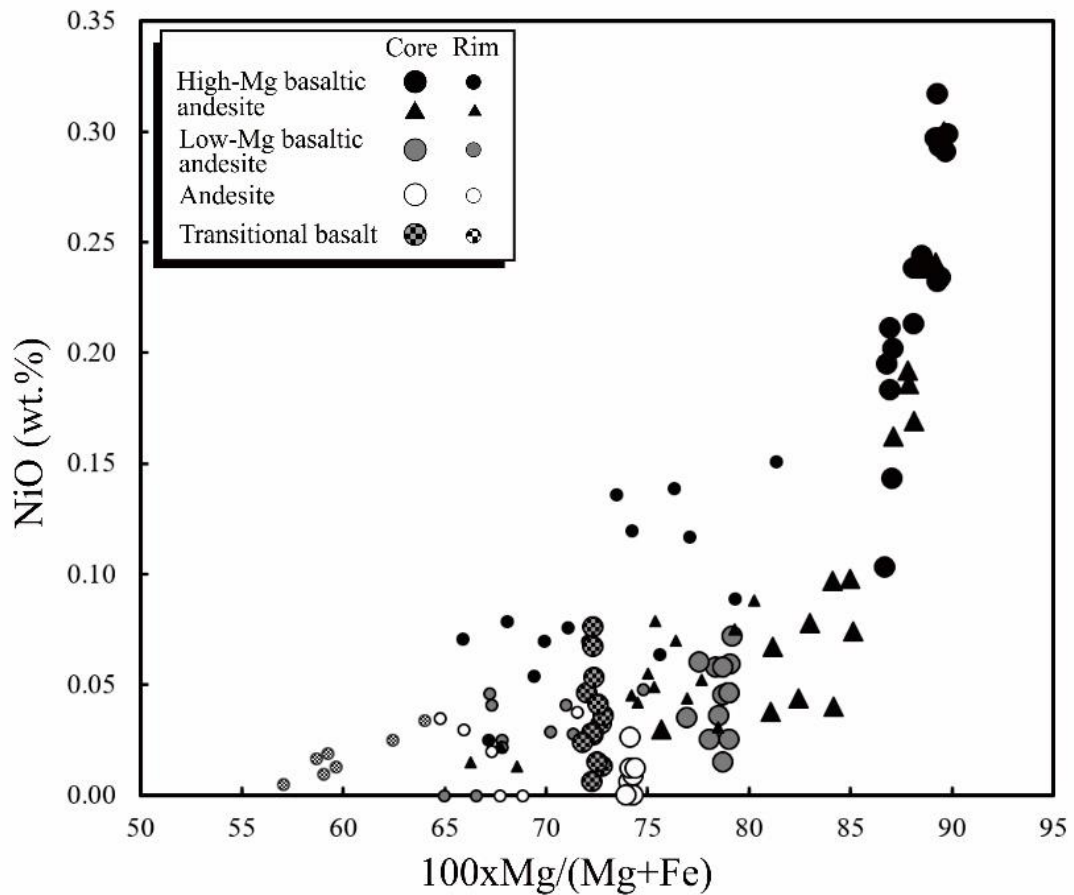


Figure 26. Compositional variation of Mg-number [$100 \times \text{Mg}/(\text{Mg} + \text{Fe})$] vs NiO in olivine phenocrysts in Rajabasa samples. The olivine phenocrysts from high-Mg basaltic andesite are considerably higher in NiO contents compared to other series.

Spinel and Fe-Ti oxides

Microphenocrysts of chromian spinel often occur as inclusion in magnesian olivine (Fo_{82-90}) (figure 27) and rarely in pyroxene and plagioclase. They are present only in high-Mg basaltic andesite samples. The spinels are chromium-rich, in terms of $\text{Cr}/(\text{Cr} + \text{Al}) = 0.51-0.55$. These values can be equilibrated with arc peridotite compositions in olivine-spinel mantle array (OSMA) by Arai (1994) (figure 27). The Cr-spinels exhibit slight normal zoning with cores are more chromium-rich than rims. Fe-Ti oxide minerals occur as abundant titanomagnetite and rare ilmenite.

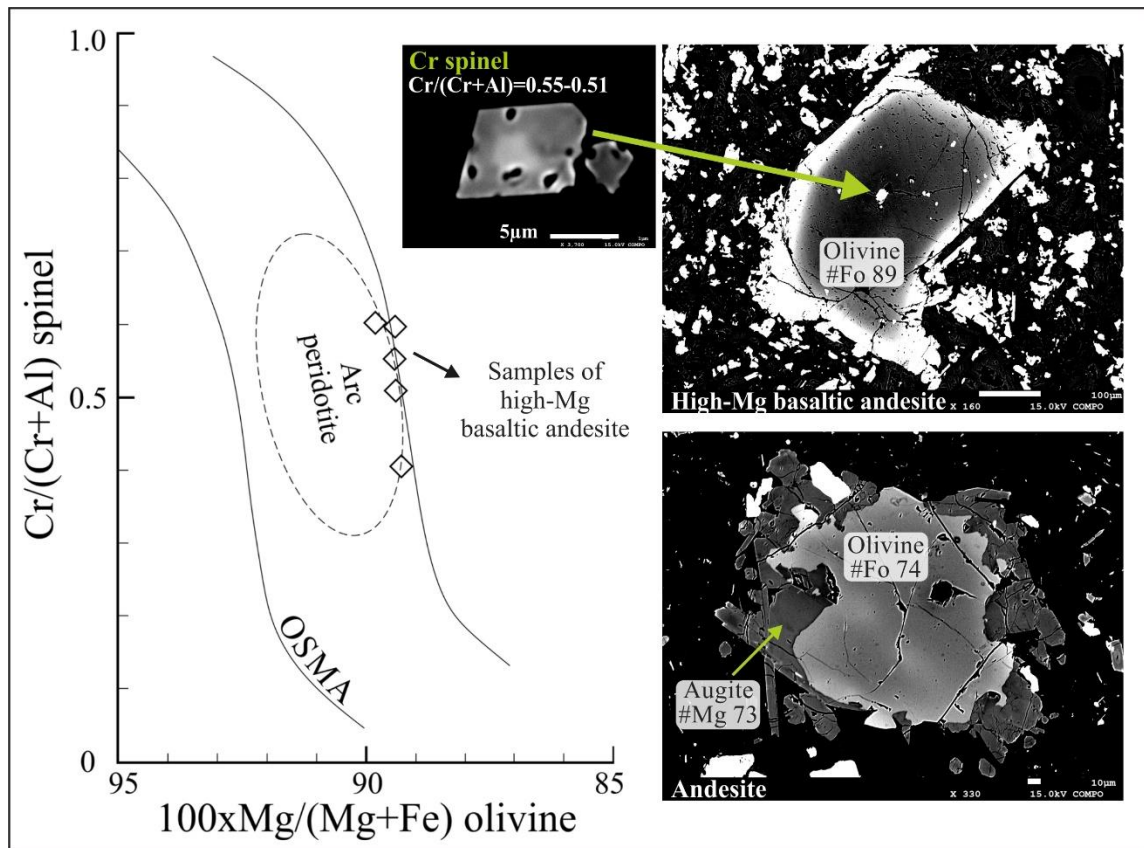


Figure 27. The compositions of olivine-hosted microphenocryst spinel in term of $\text{Cr}/(\text{Cr}+\text{Al})$ and their plot in olivine-spinel mantle array (Arai, 1994).

Groundmass

Compositions of groundmass of plagioclase and pyroxenes in samples from Tangkil series are similar to that of phenocrysts. Groundmass of plagioclase and pyroxene from Rajabasa samples vary in composition and some are distinct with the phenocryst compositions. In high-Mg basaltic andesite, low-Mg basaltic andesite, and andesite samples, some groundmasses of plagioclase or pyroxene are more calcic or magnesian than the phenocrysts. In transitional basalt, augite groundmass is less magnesian than augite phenocrysts. Pyroxene groundmass from all Rajabasa series in most cases show a common composition at Mg_{-71} . Groundmass composition is provided later in discussion.

CHAPTER V

DISCUSSION

5.1 THE VOLCANISM OF TANGKIL AND RAJABASA

This study elucidated the history of volcanism in Tangkil and Rajabasa volcanoes. The volcanism was commenced by the eruption of Tangkil volcano. The early activity of Tangkil is characterized by felsic magma (Tklf), whereas the later activity at *c.* 4.3 Ma is characterized by mafic magma (Tkfm). Then, the volcanic activity was halted. After termination of the activity of Tangkil volcano, it took *c.* 4 Ma to resume volcanic activity at Rajabasa volcano. The ages of commencement and cessation of Rajabasa volcanism are at *c.* 0.3 Ma and *c.* 0.1 Ma, respectively. The activity of Rajabasa is characterized by major intermediate and minor mafic lavas. The most mafic samples (olivine-rich basaltic andesites of Rbs 2 and basalts of Rbs 8) are produced by the older eruption center of Balerang cone (figure 8).

The volcanism in the area is likely to be affected by the tectonic setting. The clockwise rotation of Sumatra relative to Java which preceded the activity of Rajabasa has started since at least 2.0 Ma (Ninkovich, 1976; Nishimura et al., 1986). The changes of volcanic center from Tangkil to Rajabasa and eruption center from Balerang cone to Rajabasa cone is parallel with the major NW-SE fault zone in Sumatra (Sumatra Fault System). This crustal scale strike-slip faulting may have provided different paths for the magma to rise. A similar idea has been suggested by Bronto et al. (2012), who presumed that the change of eruption center in Rajabasa volcano was controlled by a deep fracture. A number of studies have also proposed a similar influence of strike-slip faulting on volcanism (e.g. Fytikas and Vougioukalalis, 1993; Piper and Perissoratis, 2003; Pe-Piper et al., 2005).

5.2 OPEN SYSTEM MAGMATIC PROCESS

Implications of mineral texture and zoning in plagioclase phenocrysts

Open system magmatic processes are indicated by petrographic evidence for the rocks from the last Tklf and high-Mg basaltic andesite, low-Mg basaltic andesite, and andesite. This evidence includes resorbed textures in plagioclase, such as dissected zoning, irregular and patchy core, as well as cellular or sieved texture with melt inclusions (figures 14a-c). The resorbed textures in plagioclase reflect changes in magmatic condition experienced during crystal growth (e.g. Humphreys et al., 2006).

Partial dissolution of plagioclase can be caused by heating, hydration of melt, decompression, or a combination of these processes (e.g. Tsuchiyama, 1985; Nakamura and Shimakita, 1998; Nelson and Montana, 1992). Once in a reservoir, the differentiation of magma continued by cooling, convection, decompression, and recharge of new magmas.

Partial dissolution of crystal exterior is characterized with overgrowth of Ca-rich plagioclase on the crystal surface (figures 14b and 15). This texture is consistent with the experimental results of Nakamura and Shimakita (1998), who invoked dissolution-recrystallization origin.

Anorthite zonation represents the history of ambient magmatic conditions as diffusion rate of NaSi-CaAl is low relative to timescales of magmatic event. The irregular or sieved cores/mantles and clear euhedral rims are formed under different conditions and stages. Dissolution textures were formed by one or combination processes of heating, hydration or decompression. Then, the recrystallization of higher Ca/Na mantle/rim progressed after the dissolution process

Implications of mineral texture and zoning in pyroxene phenocrysts

The resorption-overgrowth texture in pyroxene crystals also represents open system processes. Anhedral and rounded cores in pyroxene suggest resorption process (figure 14e). The resorbed cores are only developed in reversely zoned clinopyroxene. The Fe-rich cores are characterized by embayed morphology and unconformable interfaces with mantle, indicating resorption of Fe-rich pyroxene. The dissolution surface in pyroxene develops in response to an external factor such as temperature increase above their liquidus, compositional change (including oxygen fugacity), or decompression.

The resorbed core is overgrown by a less evolved (higher Mg/Fe) mantle or rim, implying resorption-overgrowth was induced by a change in ambient magma composition from low Mg/Fe to high Mg/Fe (mafic) composition. The Mg-rich mantle shows normal zoning with polygonal growth bands (figures 14d, e), indicating progressively evolving composition of melt during cooling.

The coexistence of augite-mantled orthopyroxene with clear euhedral orthopyroxene, as well as normal and reverse zoning of clinopyroxene in the same sample reflect wide variation (figure 14f). The texture of orthopyroxene mantled by augite can be explained by heating and compositional change of melt (e.g. Gerlach and Grove, 1982), where the orthopyroxene was resorbed first, then overgrown by augite.

Repetitive changes of T, H₂O, or chemical composition

Of the two types of plagioclase and pyroxene, resorption of evolved core and overgrowth of less evolved mantle can be accounted for by a temperature rise, influx of volatile (to reduce T of liquidus and change equilibrium composition), or change of chemical composition of ambient magma to higher MgO/FeO and higher CaO/Na₂O. The multiple zones of dissolution-overgrowth textures in plagioclase crystals (i.e. figures 14c and 16) indicate that the changes of magmatic condition in T, H₂O, or chemical composition were repetitive. Lack of multiple dissolution-overgrowth layers in other

minerals implies faster chemical diffusion rate than that in plagioclase (Grove et al., 1984; Morse, 1984).

Indication of magma mixing

Magma mixing is indicated by whole-rock chemistry diagrams (e.g. figures 10 & 11). Fractional crystallization trends are concave-upward in diagrams of MgO vs SiO₂. Two linear trends on the diagram of K₂O vs MgO (figure 28), except for a transitional endmember of Rbs 8, indicate the mixing of two mafic endmembers with a felsic endmember.

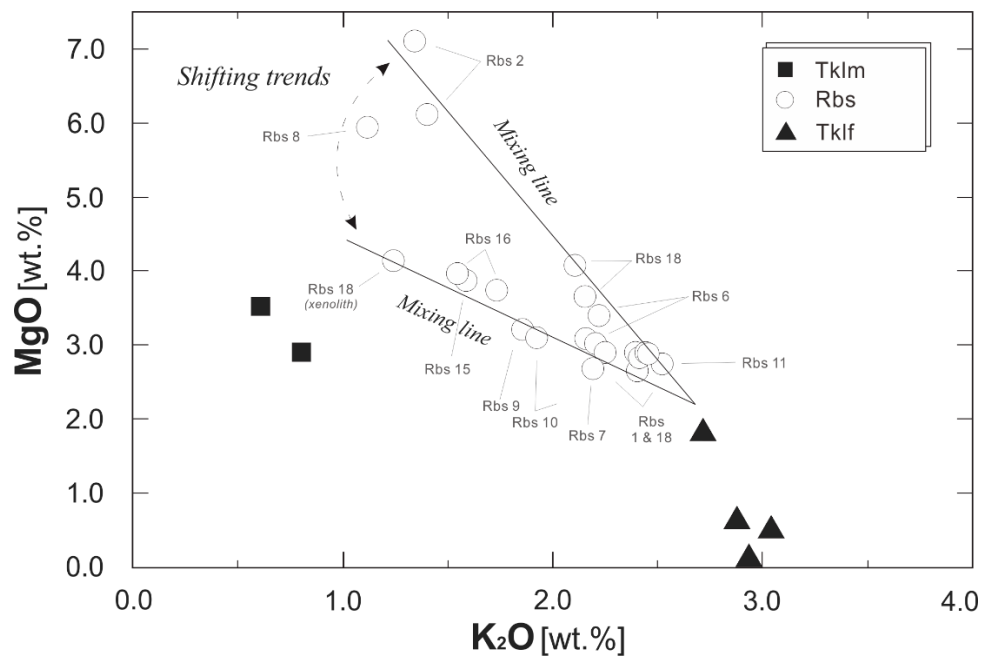


Figure 28. The mixing process is indicated by the two linear trends on K₂O vs MgO diagram. The change of magmatic activity from the two mafic endmembers is indicated by the shifting trend.

MELTS software (Ghiorso and Sack, 1995; Gualda et al., 2012) is used to evaluate and modelling the fractional crystallization trends. Composition of 50 wt% SiO₂ for both

mafic endmembers was assumed and that of other elements was determined by extrapolating the trend of the elements to the assumed SiO₂ content; the total obtained for both was 100 wt%. We assumed the system does not contain free-water at liquidus, then by trial-and-error calculations water content of 2 wt.% was determined and fugacity constrained to QFM buffer. The calculation of phase relations under these conditions could produce the phenocryst assemblage of ol+sp+cpx+opx+pl (figure 29). Three individual isobaric calculations (at 1, 2, and 3 kbar) show that no model result of fractional crystallization resembles the data for each mafic endmember trend, although at lower pressure (1 kbar) the simulated curves approximate the observed trends (figure 30). Other calculated phase relations diagrams are provided in appendix (E: MELTS calculation).

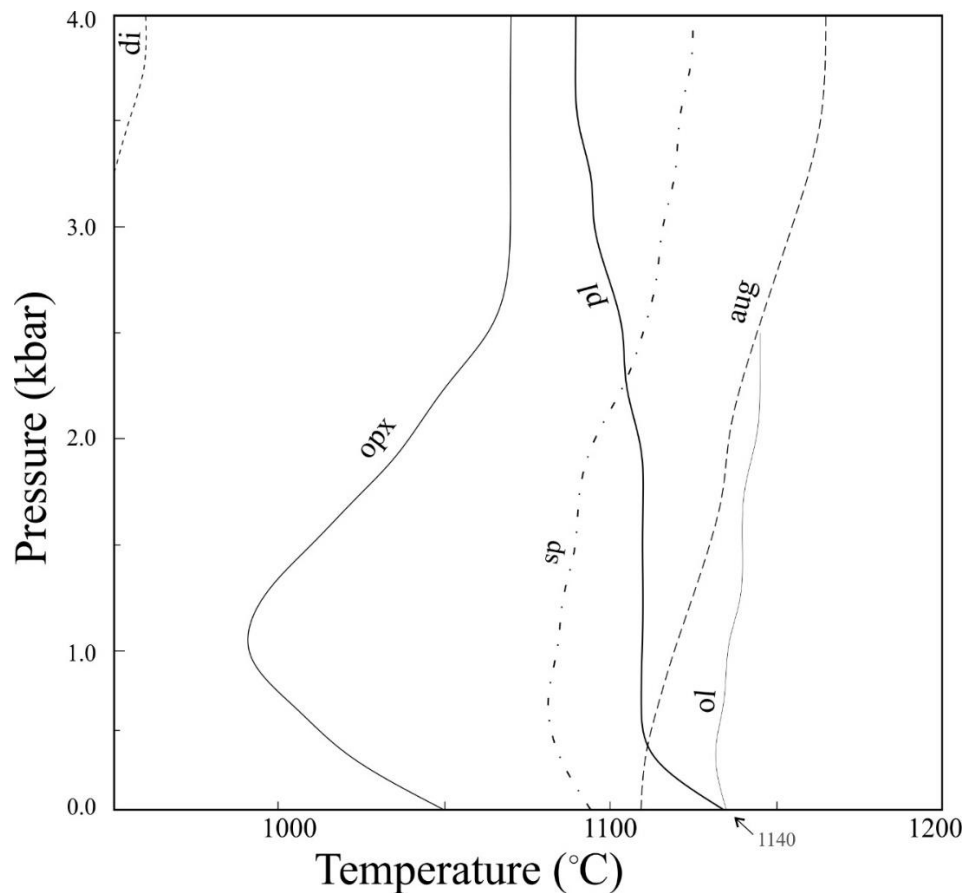


Figure 29. Phase relations of the low-Mg basalt endmember in T - P space calculated with MELTS.

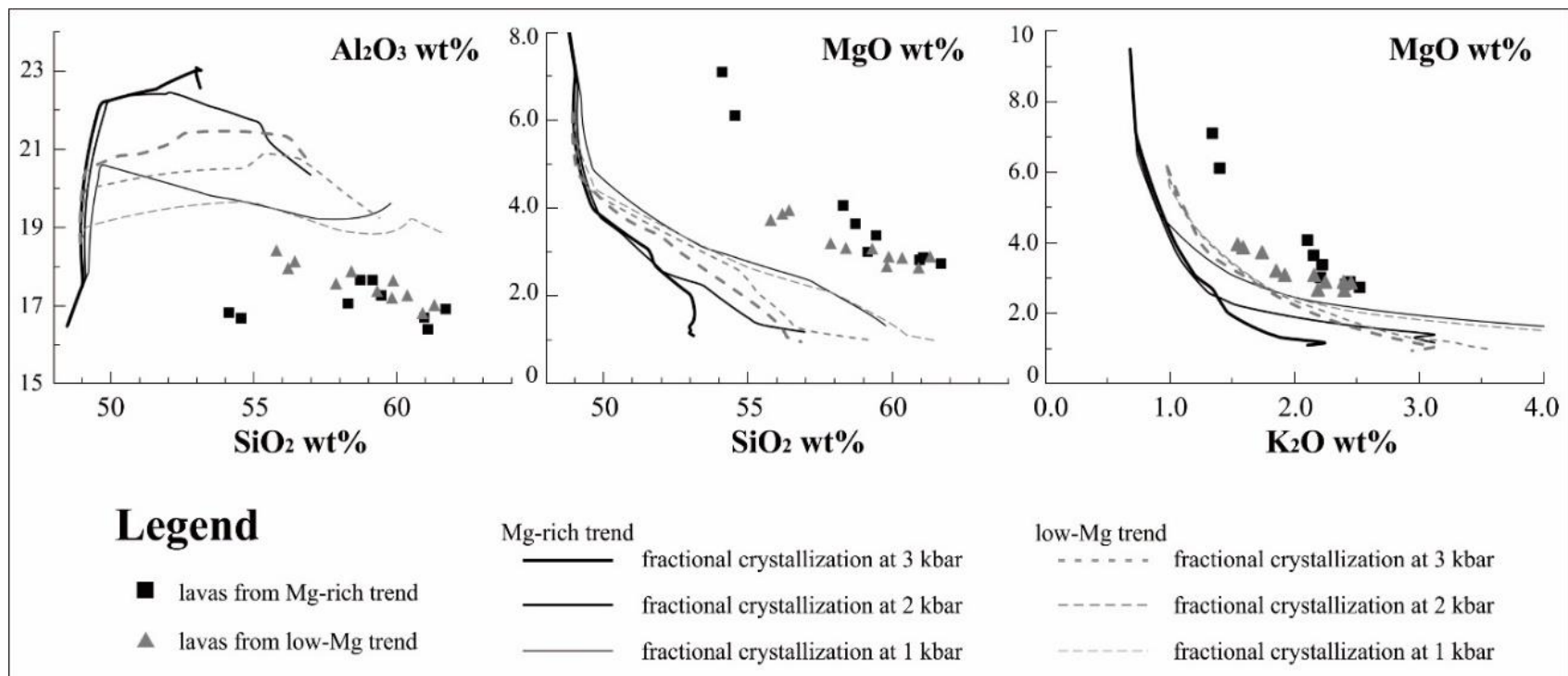


Figure 30. Modelling of major elements fractional crystallization with MELTS presented on Harker diagrams for Rajabasa. The parameters used in calculation are described in the text. Lines of fractional crystallization with pressures of 1, 2, and 3 kbar are shown. Samples of 19.02a and I.8.01 were excluded from calculation.

In figure 12, the spikes of CaO and MgO indicate that the recharges of high-Mg mafic endmember are sporadic, whereas the recharges of low-Mg mafic endmember are common during the entire lifetime of Rajabasa. The last Tklf also underwent recharge of mafic magma, indicated by whole-rock compositional variation of low-SiO₂, high-MgO, -Ni, and -Cr (figure 12), and by the mineral textures of plagioclase and pyroxenes shown above.

Repeating recharges

The evidence of repetitive magma recharges is also represented by the fluctuating temporal whole-rock chemical variation which shows that differentiated andesite is intercalated with Mg-rich rocks (figure 12). This variation can be produced by multiple replenishment of the evolved magma reservoir with mafic magma. Belkin et al. (1993), Villemant et al. (1993), and Gertisser and Keller (2003a) found similar variation and suggested a multiple replenishment into a pre-existing magma reservoir. Based on the petrographical and geochemical evidence, we conclude repeating magma recharges during the magmatic evolution of Rajabasa.

Endmember magmas

For the magma system at Rajabasa, at least three endmember magmas are identified: (1) Mg-rich, medium-K basalt magma; (2) low-Mg, medium-K basalt magma; and (3) high-K andesite magma (figures 9 and 11). The high-Mg, medium-K basalt magma is a primitive magma with high Cr (>250 ppm) and Ni (>114 ppm)

contents. Another basalt magma (2) is more differentiated, indicated by lower MgO, Cr, and Ni contents. The composition of the felsic endmember of Rajabasa volcano is determined by the intersection of the two linear trends at an andesitic composition of ~2.2 wt% MgO and ~62 wt% SiO₂ (figure 11). As discussed above, the Mg-rich medium-K basalt magma and the low-Mg medium-K basalt magma repeatedly injected into the high-K andesite magma (figure 28).

Tangkil involves bimodal magma system of basalt and felsic magma. The felsic endmember of Tklf is more evolved, > 71 wt% SiO₂ and < 0.1 wt% MgO, than the felsic endmember of Rajabasa (figure 11). The last Tklf could be a product of mixing between the felsic endmember and a mafic endmember.

The lavas of Tkln from Tangkil and of transitional basalt are different in compositional or textural characteristics from other series (table 4). Compared to other series, these rocks are plotted in tholeiitic field in Miyashiro diagram (1974) (figure 9) and more enriched in iron (FeO). Phenocrysts in these lavas do not show resorption-overgrowth texture, a feature that is usually associated with open-system magmatic process. Although the plagioclase crystals from Tkln series exhibit sieved texture (figure 31), none of them show overgrowth of less evolved plagioclase composition. The sieve texture without less evolved overgrowth is possibly formed by decompression process alone (Nelson and Montana, 1992). It means that the other processes (temperature rise or hydration) might not needed. These rocks are therefore suggested to be the products of fractional crystallization of mantle-derived basaltic magmas, with or without assimilation of crustal melts.

Table 4. Different characteristics in lava samples among Tangkil and Rajabasa series.

Characteristics	Tangkil		Rajabasa	
	Tklm	Tklf & last Tklf	Transitional basalt	Other three series
Mineral assemblages	pl + ol	pl + cpx + opx + hbl	pl + ol + cpx	pl + ol + cpx + opx + hbl/bt
Iron contents	$\text{FeO}^{\text{t}} > 9 \text{ wt\%}$	$\text{FeO}^{\text{t}} \leq 4 \text{ wt\%}$	$\text{FeO}^{\text{t}} > 9 \text{ wt\%}; \text{Al \& Ti} \gg$	$\text{FeO}^{\text{t}} \leq 8 \text{ wt\%}; \text{Al \& Ti} \ll$
Compositional zoning in plagioclase	Normal zoning	Normal and reverse zoning	Normal zoning	Normal and reverse zoning
Compositional zoning in pyroxene	Narrow compositional range	Wide compositional range	Narrow compositional range	Wide compositional range
Notable textures in plagioclase	Euhedral; sieved & patchy	Anhedral to euhedral; dissolution-overgrowth	Euhedral; sieved & patchy	Anhedral to euhedral; dissolution-overgrowth
Fe-Mg partitioning of olivine and pyroxene	-	-	Almost equilibrium	Disequilibrium

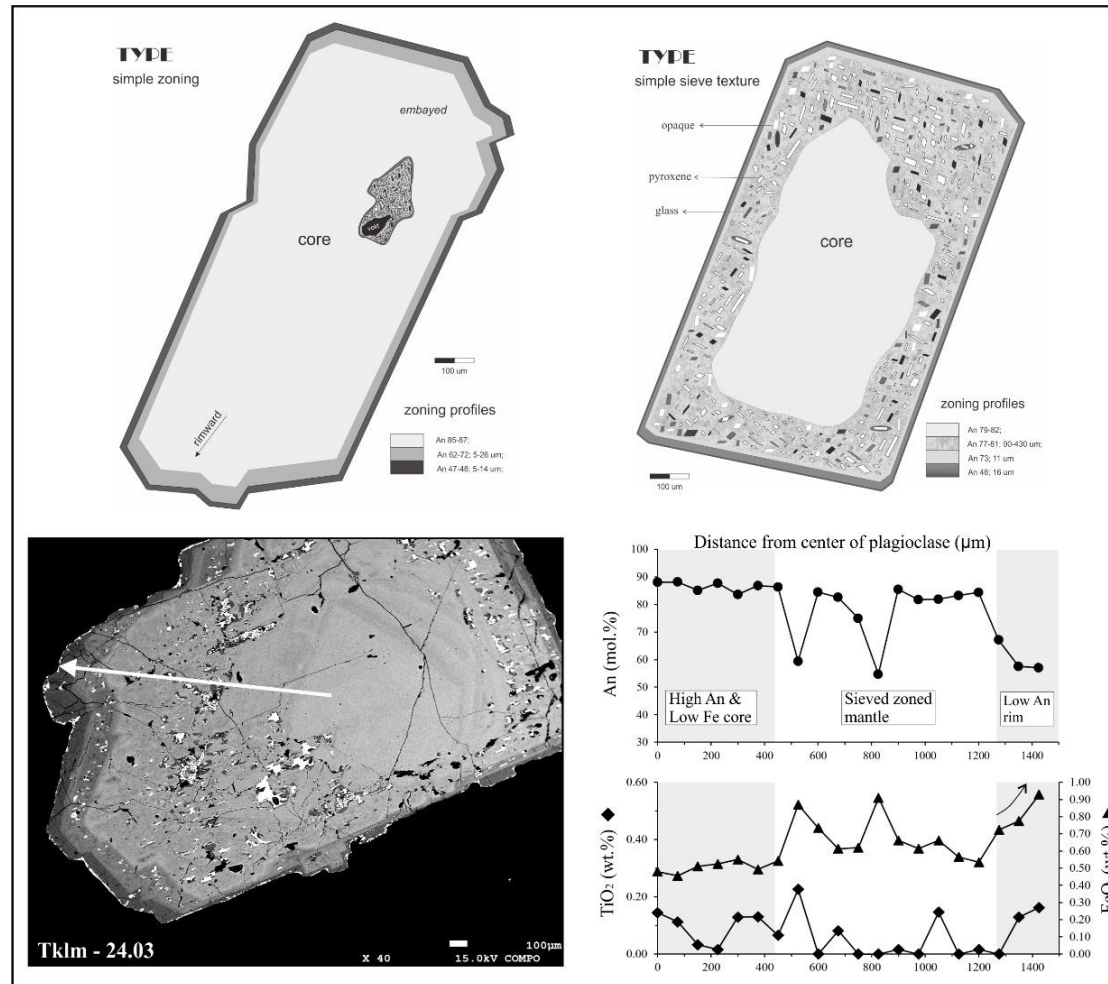


Figure 31. Textural and compositional characteristics of plagioclase crystals from Tklm samples.

5.3 THE ORIGIN OF PHENOCRYSTS

Core-rim compositional variations of phenocrysts in the high-Mg basaltic andesite, low-Mg basaltic andesite, and andesite also suggest various origins and correlation between series. Anorthite and magnesium zonation represent the history of ambient magmatic compositions, where a higher number correspond to less evolved composition and hotter magmatic condition.

The composition of plagioclase phenocrysts in andesite overlaps with those in high-Mg basaltic andesite (An₉₀ and An₅₀) and low-Mg basaltic andesite (An₇₈ and An₅₃) (figure 32). The Mg-number of augite phenocrysts are in equilibrium with that of olivine phenocrysts (figure 33), indicating that the crystals were formed in the same condition where the $K_D(\text{Fe-Mg})^{\text{ol-aug}}$ for Mg-Fe is nearly one during early crystallization.

For these reasons, we concluded that the endmember of Mg-rich, medium-K basalt magma produced plagioclase (An_{~90}), augite (Mg_{~87}), olivine (Fo_{~90}), and chromian spinel; the endmember of low-Mg, medium-K basalt magma produced plagioclase (An_{~78}), augite (Mg_{~78}), enstatite (Mg_{~77}), and olivine (Fo_{~79}); the endmember of high-K andesite magma formed plagioclase (An_{~56}), augite (Mg_{~77}), enstatite (Mg_{~69}), olivine (Fo_{~75}), and hornblende/biotite (figure 34).

The repetitive recharges of the basalt magmas to andesite magma generate the mineral textures and zonings observed in high-Mg basaltic andesite, low-Mg basaltic andesite, and andesite samples. The clinopyroxene that mantled orthopyroxene formed during the final stage of crystallization after mixing as their mantle and rim are same in composition with that of the discrete clinopyroxene phenocrysts (figures 23 and 24).

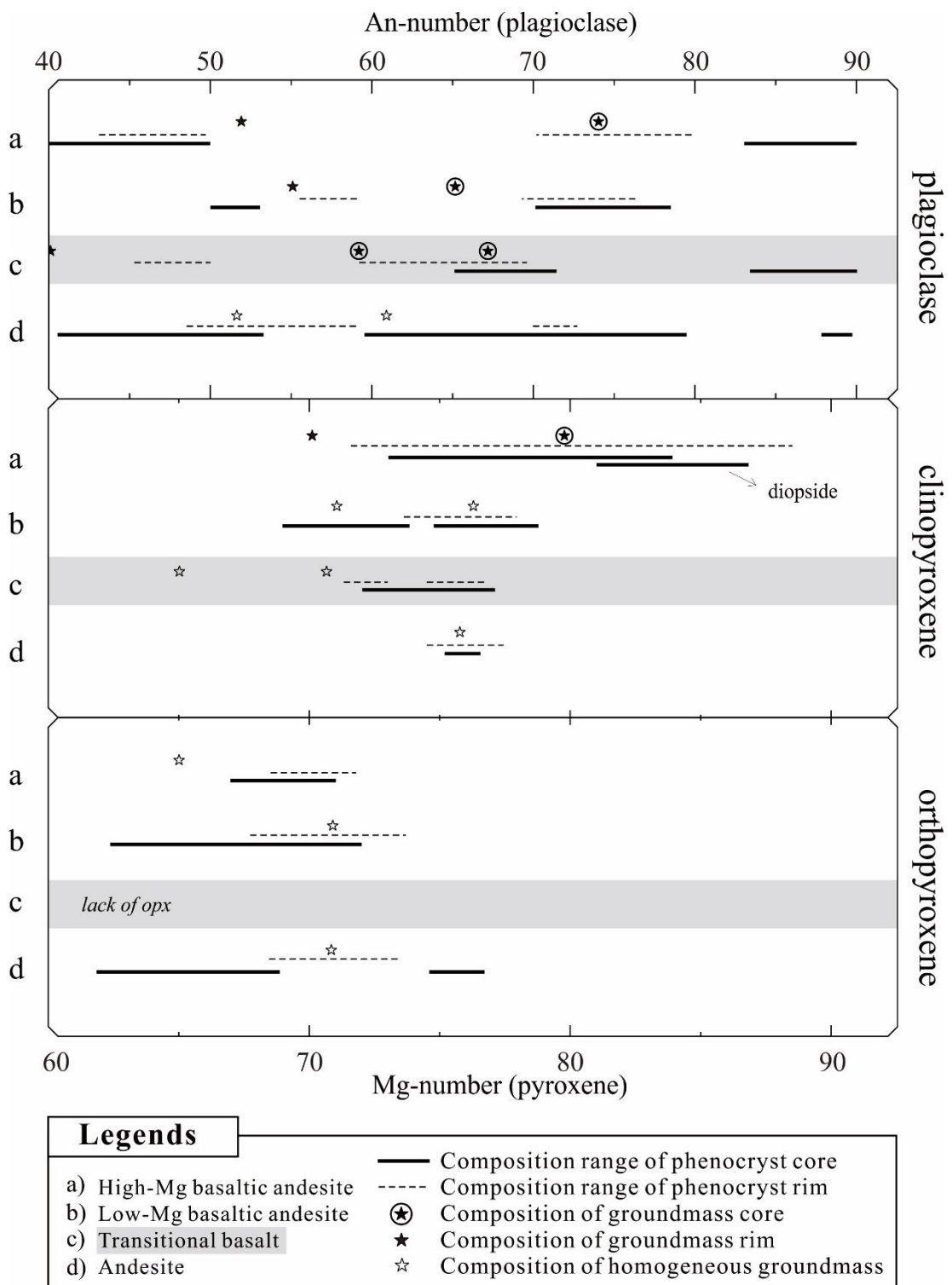


Figure 32. The schematic diagram of compositional relation between series in Rajabasa used for identification of endmember magmas composition.

That texture could be produced as orthopyroxene from original melt was compositionally out of equilibrium with a new melt and instead of dissolving it started to re-crystallize clinopyroxene.

The presence of hornblende and biotite changed temporally and seem to be affected by temperature conditions in the felsic endmember reservoir (figure 8). The andesite magma stayed fixed in composition (at *c.* 62 wt% SiO₂), but its temperature condition may change the mineral assemblage. Biotite and hornblende were not present when the reservoir was heated by mafic injections. Biotite and hornblende crystallize in a relatively low-T andesitic magma. Biotite and hornblende crystallized when the reservoir was cool, while they were not present when the reservoir was heated by mafic influxes or the temperature was still high (like in early period).

Plagioclase phenocrysts in last Tklf show bimodal composition, suggesting contributions of different endmember magmas. The sodic plagioclase (An_{~53}) did not equilibrate with mafic endmember magmas, as well as the calcic plagioclase (An_{~90}) with felsic endmember magmas. The basalt magma formed plagioclase (An_{~90}) and augite (Mg_{~82}); the rhyolite magma produced plagioclase (An_{~53}) and enstatite (Mg_{~64}) (figure 34). The similar compositions between pyroxene rims and pyroxene groundmass (Mg_{~65}) implies that their crystallization took place at the same stage.

Unlike the iron enrichment trend of last Tklf which is linear with Tklf, that with Tkml is discontinuous (figure 9). The plagioclase in Tklf is similar in composition with the sodic plagioclase in last Tklf, thus indicating the origin from a similar evolved magma with An_{~56}. On the other hand, though the composition of most calcic plagioclase in Tkml and last Tklf are similar, they were nevertheless formed in different magmatic condition.

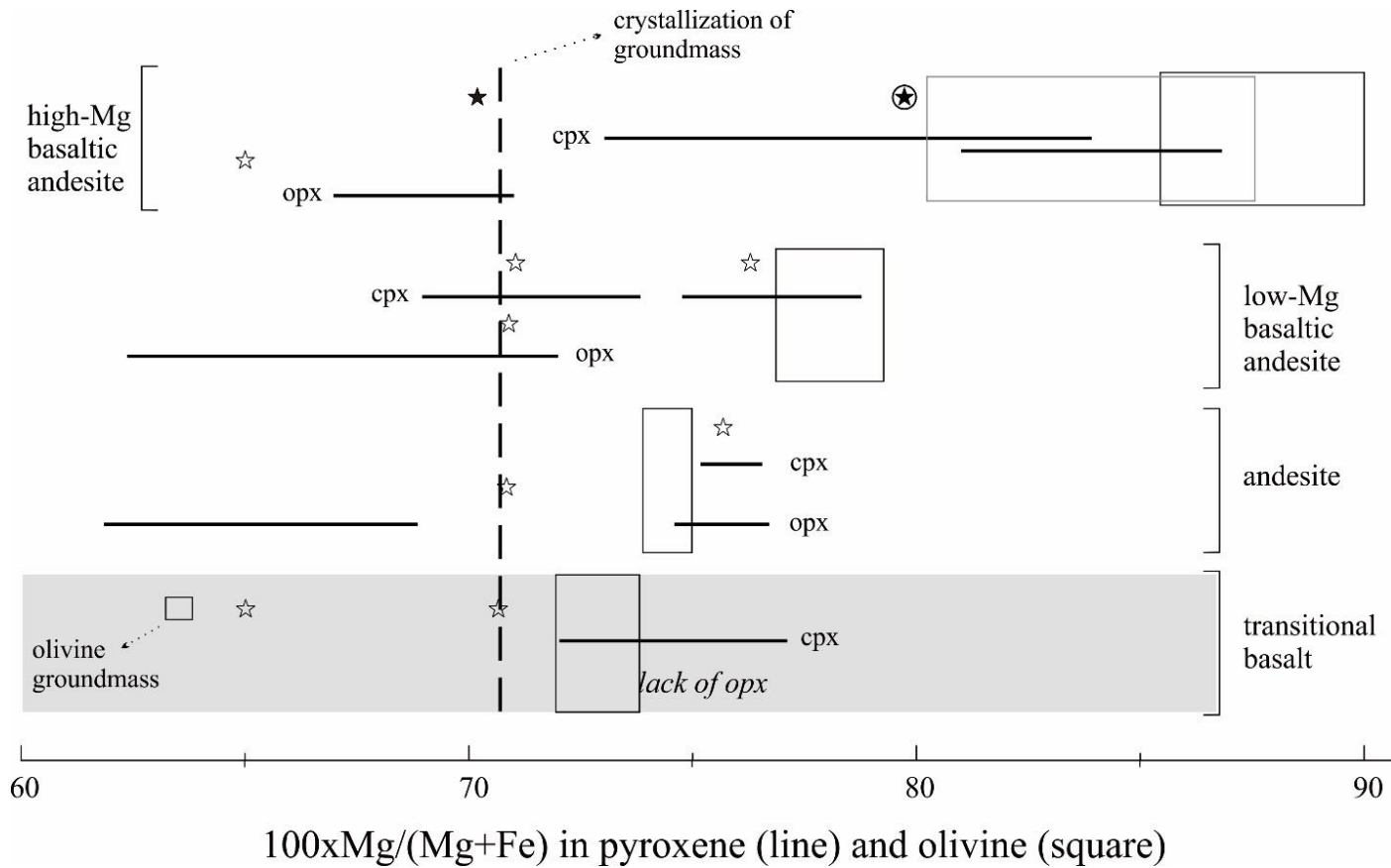
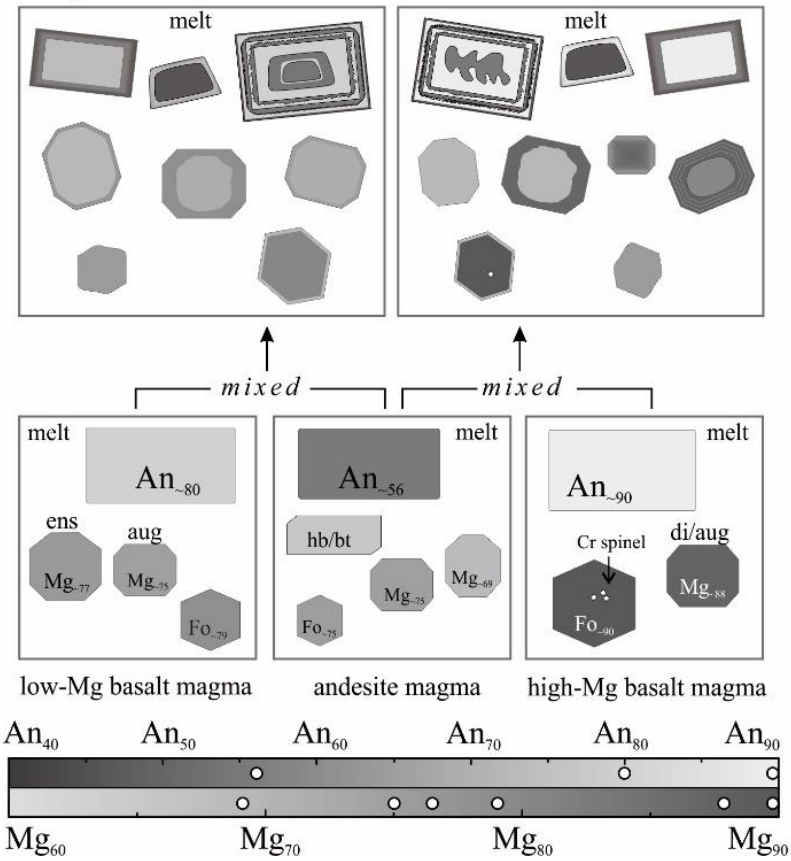


Figure 33. This schematic diagram shows resembling values of Mg-number [$100xMg/(Mg+Fe)$] in olivine and pyroxene phenocrysts in Rajabasa samples. Cores of olivine in samples from high-Mg basaltic andesite, low-Mg basaltic andesite, and andesite can be equilibrated with the most magnesian clinopyroxene from the same series. Star symbols correspond to composition of pyroxene groundmass.

Rajabasa



Tangkil

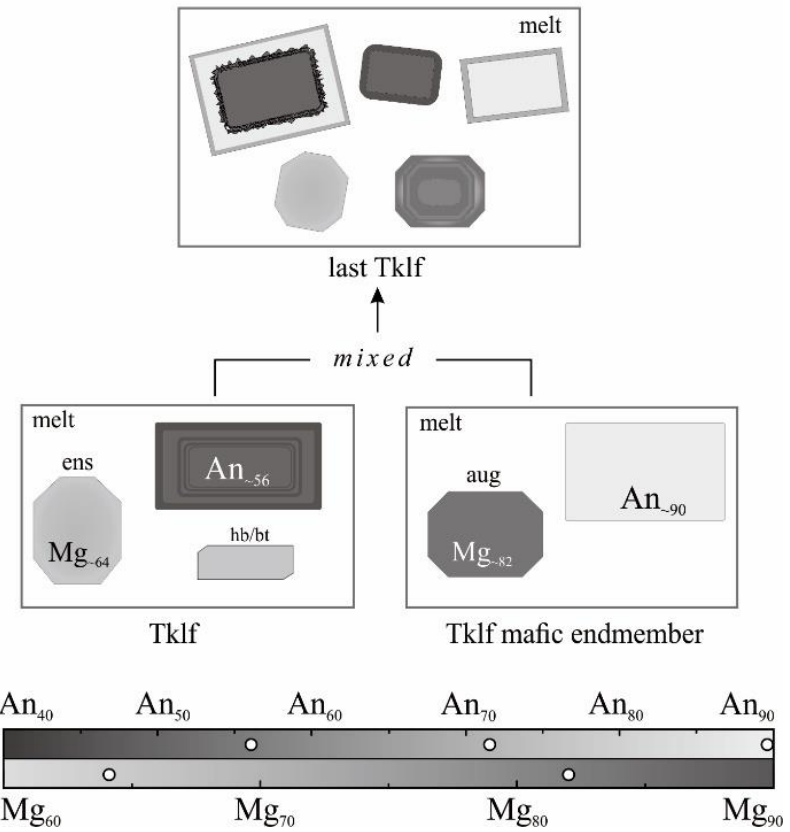


Figure 34. The origin of phenocrysts deduced from compositional correlation between series. The bar below represents the scale of anorthite/magnesium-number.

5.4 MAGMA PLUMBING AND EVOLUTION SYSTEM

The thermobarometry calculation yielded variations of T - P (table 5) which indicate multiple crystallization origins. In high-Mg and low-Mg basalt magmas, the evolved equilibrium mineral pairs were not found, and their T estimates of less evolved pairs are higher than T estimates of evolved pairs in andesite. The T estimate of high-Mg basalt magma is higher (avg. 1174 °C) than that of low-Mg basalt magma (avg. 972 °C), and that of andesite magma (avg. 932 °C). It should be noted that the series of high-Mg basalt, low-Mg basalt, and andesite exhibit a wide range of temperatures within series. The various temperatures for the andesite condition are consistent with the mineral assemblages. As informed earlier, the andesite endmember magma shows a variety of mineral assemblages, some contain biotite and hornblende, but others are olivine rich. It implies that during evolution of the andesite magma reservoir, the temperatures were variable. The biotite- or hornblende-bearing samples have relatively low T estimates. Groundmass of pyroxenes share a common Mg-number in all series, namely Mg₇₁, suggesting they were formed in the last stage of crystallization with T estimate of 920 °C.

For Tangkil, phenocrysts in last Tklf show a distinct of T estimates (avg. 934 and avg. 1069 °C) that implies different conditions of magmas. The felsic magmas from Tklf and last Tklf series show similar T estimates of 924-934 °C, thus together with textural and zoning evidence discussed above they are assumed to be a same magma. The mafic magma from last Tklf is avg. 1069 °C.

Similarly, variations in the depths calculated for crystallization of phenocrysts suggest multiple levels of magma storage (table 5). The magma storage regions beneath Tangkil and Rajabasa are deeper than 11 km but above sub-Moho level (figure 35). Based on Harjono et al (1989), the lithological units in these regions are diorite or gabbro until sub-Moho level at 22 km. Result of crystallization depth of clinopyroxene or olivine phenocrysts in high-Mg basaltic andesite magma confirmed the presence of a magma storage with depth of *c.* 25 km, which is equivalent to the mantle depth. The magnesian olivine (Fo₋₉₀) with 0.32 wt% NiO (figure 26) can be equilibrated to that from mantle

Table 5. Geothermobarometer calculation results for Tangkil and Rajabasa volcanoes. Values of *T* and *P* are given as average and range.

Group	Series	Minerals pairs	Model	T (°C)	P (kbar)	Depth (km)
Tangkil	Tklf	Plagioclase-hornblende	Holland & Blundy (1994)	924 (919-928)	3.9* (3.6-4.3)	14.6*
	Last Tklf	Two pyroxenes	Putirka (2008)	934 (933-937)	3.9 (3.6-4.3)	14.6
			Brey & Kohler (1990)	945 (945-947)	-	-
	Last Tklf	Two pyroxenes	Putirka (2008)	1069 (1057-1081)	4.7 (4.2-5.2)	17.4
			Brey & Kohler (1990)	1066 (1063-1069)	-	-
	Tklm	-	-	-	-	-
Tklf groundmass	Two pyroxenes	Putirka (2008)	920	3.3	12.6	
Rajabasa	High-Mg basalt	Clinopyroxene-melt	Putirka (2008)	1174 (1167-1179)	7.1 (6.6-7.4)	25.2
		Olivine-melt	Putirka et al. (2007)	1224	-	-
	Low-Mg basalt	Two pyroxenes	Putirka (2008)	972 (945-989)	5.1 (3.1-6.4)	18.8
			Brey & Kohler (1990)	967 (940-997)	-	-
	Andesite	Two pyroxenes	Putirka (2008)	932 (915-953)	3 (2-4.2)	11.5
			Brey & Kohler (1990)	925 (900-952)	-	-
	Transitional basalt	Clinopyroxene only	Putirka (2008)	1185 (1175-1190)	4.3 (3.1-5.9)	16.0
		Clinopyroxene-melt	Neave & Putirka (2017)	1143 (1142-1144)	5.9 (5.8-6.1)	21.6
Groundmass	Two pyroxenes	Brey & Kohler (1990)	980 (966-994)	2.1 (1.5-2.7)	8.4	

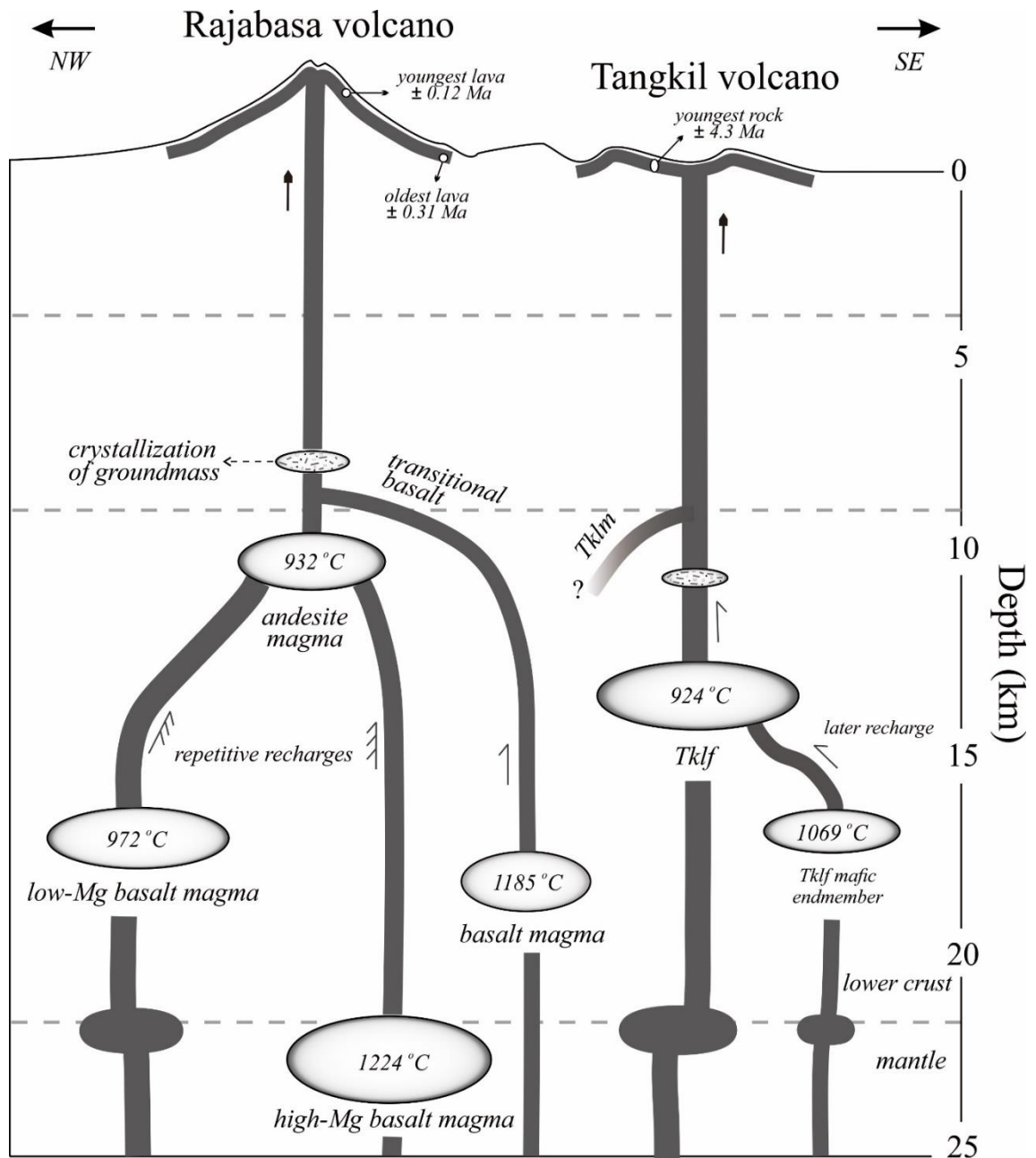


Figure 35. Schematic illustration of the magma plumbing system beneath Tangkil and Rajabasa volcanoes based on thermobarometry calculation. It shows that the main magma storage region is at mid- to low-crustal level, while only high-Mg basalt magma from Rajabasa resides at upper mantle. The temporal data is also shown.

(Takahashi, 1986). Likewise, the source composition of olivine-spinel equilibrates with a mantle material of arc peridotite (Arai, 1987) (figure 27).

In summary, magma plumbing system beneath Tangkil and Rajabasa involves interaction of several mafic and single felsic endmember magmas during its evolution. The storage region and condition of the magmas are varying, from hot and deep primitive magmas to colder and shallower evolved magma.

Tangkil magmatism was initially sourced from rhyolite magma at mid-crustal level. Then at later stage, relatively deeper and hotter basalt magma injected and mixed with the rhyolite magma. This process results to bimodal compositions and crystallization temperatures in plagioclase phenocrysts. Ascent of another primary basalt magma took place at *c.* 4.33 Ma and this magma unmixed with other magmas. The narrow compositional range in their solely normally zoned phenocrysts is consistent with the limited mineral assemblages. Since then, Tangkil volcano ceased its activity.

Rajabasa magmatism was originated from four distinct magmas and they were active during Upper Pliocene. During its evolution, the upper mantle-origin high-Mg basalt magma and the lower crust-origin low-Mg basalt replenished repetitively the middle crust-origin andesite magma. The hotter crystallization temperatures accord with deeper level of emplacement. This process is recorded in phenocrysts which have various crystallization temperatures. A vast array of temperature is consistent with the variety of mineral assemblages, where some andesite rocks contain biotite and hornblende while others are rich in olivine. It implies that the temperature was variable during the long evolution of andesite magma. At one occasion, though, basalt magma ascent and did not mix with the other three magmas (Rbs 8). Similar to the unmixed basalt from Tangkil, this basalt contains limited mineral assemblages and solely normally zoned phenocrysts with a narrow compositional range.

For the similar range of rock composition (51-62 wt% SiO₂), the magma plumbing system in Rajabasa is coincident with that in Anak Krakatau (Dahren et al., 2012), whose main magmas emplaced at mid-crustal level (7-12 km) and some in crustal-mantle interface level (23-28 km) (figure 36).

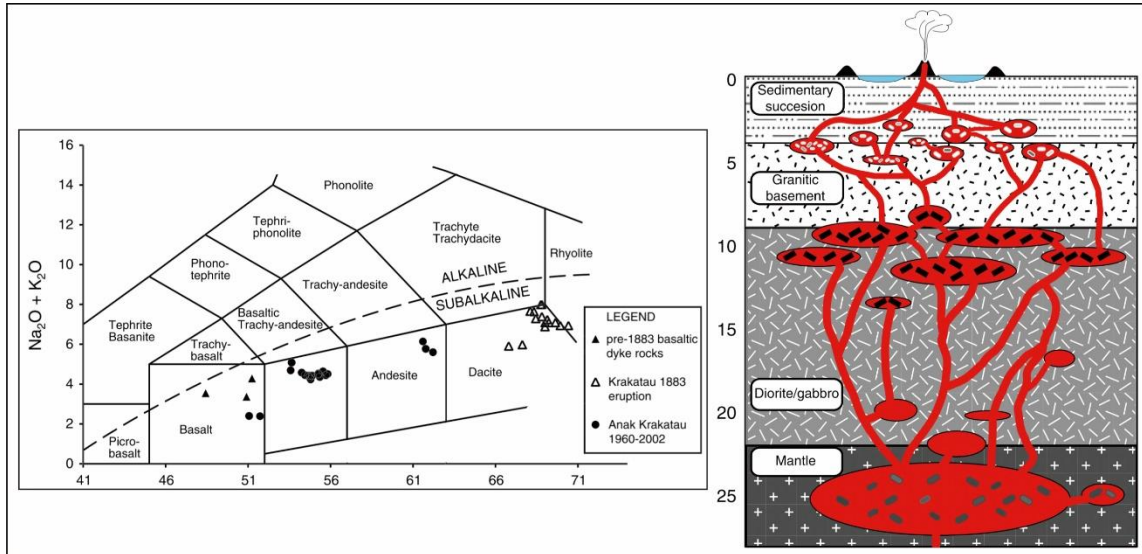


Figure 36. The magma plumbing system beneath Krakatau (Dahren et al., 2012) and the plotting of whole-rock composition (Camus et al., 1987; Mandeville et al., 1996) on TAS diagram.

CHAPTER VI

SUMMARY AND CONCLUSIONS

SUMMARY AND CONCLUSIONS

The volcanostratigraphic result combined with age dating analysis reveals: the volcanism in Tangkil commenced at before *c.* 4.3 Ma and characterized by felsic (Tklf) and mafic (Tkln) rocks; the commencement and cessation of Rajabasa volcanism are at *c.* 0.3 Ma and *c.* 0.1 Ma, respectively and characterized by intermediate lavas (Rbs).

The plagioclase and pyroxene phenocrysts from the last Tklf, Tkln, and Rbs show resorbed-overgrowth texture, a feature that can be caused by temperature rise, volatile influx, or compositional change of ambient magma. The repetitive changes of magmatic condition are indicated by the multiple zones of dissolution-overgrowth textures in plagioclase phenocryst as well as the fluctuating trend in the temporal whole-rock variation.

In the Rbs magma system, at least three different endmember magmas were involved: Mg-rich, medium-K basalt magma; low-Mg, medium-K basalt magma; and high-K andesite magma. The mixing of magmas is indicated by two-linear trends on whole-rock chemistry diagrams and MELTS. The felsic endmember composition of Rajabasa is ~62 wt% SiO₂ and ~2.2 wt% MgO; Tangkil is > 71 wt% SiO₂ and < 0.1 wt% MgO. Major element modelling by MELTS show that the observed trends are different with the fractional crystallization trends.

The mineral assemblages in Rbs reflect the features of the three endmember magmas. Olivine phenocrysts are originated from mafic endmember magmas, whereas biotite and hornblende are crystallized from felsic endmember magma. The repeated injections of the Mg-rich medium-K basalt and the low-Mg medium-K basalt into the high-K andesite magma changed the temperature conditions in the felsic endmember reservoir that can affect the mineral assemblage of biotite and hornblende.

The existence of multiple endmember magmas is also shown by variations in *P-T* estimates for the crystallization of phenocrysts. Most of the magma storage regions beneath Tangkil and Rajabasa are at mid- to low-crustal levels (11 to 21 km), except high-Mg basalt magma. The mantle-derived origin of high-Mg basalt is confirmed by whole-

rock and olivine-spinel composition. This magma is *c.* 1224 °C and 25 km, deeper than sub-Moho level at 22 km.

This study shows that the evolution of magma system and processes are reflected in the temporal petrological variations. But why the magmas mixed together during the activity of Rajabasa whereas they did not in Tangkil, remains a question.

REFERENCES

REFERENCES

- Amma-Miyasaka, M. and Nakagawa, M., 2003. Evolution of deeper basaltic and shallower andesitic magmas during the AD 1469–1983 eruptions of Miyake-Jima volcano, Izu–Mariana arc: inferences from temporal variations of mineral compositions in crystal-clots. *Journal of Petrology*, 44(12), pp.2113-2138.
- Anderson, J.L., 1996. Status of thermobarometry in granitic batholiths. *Earth and Environmental Science Transactions of the Royal Society of Edinburgh*, 87(1-2), pp.125-138.
- Andi Mangga, S., Amirudin, Suwarti, T., Gafoer, S., and Sidarto, 1994. *Geology of the Tanjungkarang Quadrangle, Sumatra*. Geological Research and Development Centre, Bandung, p.19.
- Arai, S., 1994. Characterization of spinel peridotites by olivine-spinel compositional relationships: review and interpretation. *Chemical geology*, 113(3-4), pp.191-204.
- Barber, A.J., Crow, M.J. and Milsom, J. eds., 2005. *Sumatra: Geology, resources and tectonic evolution*. Geological Society of London.
- Barker, A.K., Holm, P.M., Peate, D.W. and Baker, J.A., 2009. Geochemical stratigraphy of submarine lavas (3–5 Ma) from the Flamengos Valley, Santiago, southern Cape Verde islands. *Journal of Petrology*, 50(1), pp.169-193.
- Belkin, H.E., Kilburn, C.R. and de Vivo, B., 1993. Sampling and major element chemistry of the recent (AD 1631–1944) Vesuvius activity. *Journal of Volcanology and Geothermal Research*, 58(1-4), pp.273-290.
- Borgia, A., Poore, C., Carr, M.J., Melson, W.G. and Alvarado, G.E., 1988. Structural, stratigraphic, and petrologic aspects of the Arenal-Chato volcanic system, Costa

- Rica: evolution of a young stratovolcanic complex. *Bulletin of Volcanology*, 50(2), pp.86-105.
- Bronto, S., Asmoro, P., Hartono, G. and Sulistiyono, S., 2012. Evolution of Rajabasa Volcano in Kalianda Area and Its Vicinity, South Lampung Regency. *Indonesian Journal on Geoscience*, 7(1), pp.11-25.
- Brey, G.P. and Köhler, T., 1990. Geothermobarometry in four-phase lherzolites II. New thermobarometers, and practical assessment of existing thermobarometers. *Journal of Petrology*, 31(6), pp.1353-1378.
- Camus, G., Gourgaud, A. and Vincent, P.M., 1987. Petrologic evolution of Krakatau (Indonesia): implications for a future activity. *Journal of Volcanology and Geothermal Research*, 33(4), pp.299-316.
- Carn, S.A. and Pyle, D.M., 2001. Petrology and geochemistry of the Lamongan Volcanic Field, East Java, Indonesia: primitive Sunda Arc magmas in an extensional tectonic setting?. *Journal of Petrology*, 42(9), pp.1643-1683.
- Dahren, B., Troll, V.R., Andersson, U.B., Chadwick, J.P., Gardner, M.F., Jaxybulatov, K. and Koulakov, I., 2012. Magma plumbing beneath Anak Krakatau volcano, Indonesia: evidence for multiple magma storage regions. *Contributions to Mineralogy and Petrology*, 163(4), pp.631-651.
- Darmawan, I.G.B., Setijadji, L.D. and Wintolo, D., 2015. Geology and Geothermal System in Rajabasa Volcano South Lampung Regency, Indonesia (Approach to Field Observations, Water Geochemistry and Magnetic Methods). *Geology*, 19, p.25.
- Dempsey, S., 2013. *Geochemistry of volcanic rocks from the Sunda Arc* (Doctoral dissertation, Durham University).

- Diament, M., Harjono, H., Karta, K., Deplus, C., Dahrin, D., Zen Jr, M.T., Gerard, M., Lassal, O., Martin, A. and Malod, J., 1992. Mentawai fault zone off Sumatra: A new key to the geodynamics of western Indonesia. *Geology*, 20(3), pp.259-262.
- Fytikas, M. and Vougioukalakis, G., 1993. Volcanic structure and evolution of Kimolos and Polyegos (Milos island group). *Bull. Geol. Soc. Greece*, 28, pp.221-237.
- Foden, J.D., 1983. The petrology of the calcalkaline lavas of Rindjani volcano, east Sunda arc: a model for island arc petrogenesis. *Journal of Petrology*, 24(1), pp.98-130.
- Gardner, M.F., Troll, V.R., Gamble, J.A., Gertisser, R., Hart, G.L., Ellam, R.M., Harris, C. and Wolff, J.A., 2012. Crustal differentiation processes at Krakatau volcano, Indonesia. *Journal of Petrology*, 54(1), pp.149-182.
- Gerlach, D.C. and Grove, T.L., 1982. Petrology of Medicine Lake Highland volcanics: Characterization of endmembers of magma mixing. *Contributions to Mineralogy and Petrology*, 80(2), pp.147-159.
- Gertisser, R. and Keller, J., 2000. The geochemical evolution of Merapi Volcano (Central Java): medium-K and high-K associations. *Abstract IAVCEI General Assembly, Bali*, p. 150.
- Gertisser, R. and Keller, J., 2003a. Temporal variations in magma composition at Merapi Volcano (Central Java, Indonesia): magmatic cycles during the past 2000 years of explosive activity. *Journal of Volcanology and Geothermal research*, 123(1-2), pp.1-23.
- Gertisser, R. and Keller, J., 2003b. Trace element and Sr, Nd, Pb and O isotope variations in medium-K and high-K volcanic rocks from Merapi Volcano, Central Java, Indonesia: evidence for the involvement of subducted sediments in Sunda Arc magma genesis. *Journal of Petrology*, 44(3), pp.457-489.
- Ghiorso, M.S. and Sack, R.O., 1995. Chemical mass transfer in magmatic processes IV. A revised and internally consistent thermodynamic model for the interpolation and

extrapolation of liquid-solid equilibria in magmatic systems at elevated temperatures and pressures. *Contributions to Mineralogy and Petrology*, 119(2-3), pp.197-212.

Gill, R., 2010. *Igneous rocks and processes: a practical guide*. John Wiley & Sons.

Grove, T.L., Baker, M.B. and Kinzler, R.J., 1984. Coupled CaAl-NaSi diffusion in plagioclase feldspar: Experiments and applications to cooling rate speedometry. *Geochimica et Cosmochimica Acta*, 48(10), pp.2113-2121.

Gualda, G.A., Ghiorso, M.S., Lemons, R.V. and Carley, T.L., 2012. Rhyolite-MELTS: a modified calibration of MELTS optimized for silica-rich, fluid-bearing magmatic systems. *Journal of Petrology*, 53(5), pp.875-890.

Hall, R., 2009. Indonesia, geology. *Encyclopedia of Islands*, Univ. California Press, Berkeley, California, pp.454-460.

Hamilton, W.B., 1979. *Tectonics of the Indonesian region* (No. 1078). US Govt. Print. Off..

Harjono, H., Diament, M., Nouaili, L. and Dubois, J., 1989. Detection of magma bodies beneath Krakatau volcano (Indonesia) from anomalous shear waves. *Journal of volcanology and geothermal research*, 39(4), pp.335-348.

Harjono, H., Diament, M., Dubois, J., Larue, M. and Zen, M.T., 1991. Seismicity of the Sunda Strait: evidence for crustal extension and volcanological implications. *Tectonics*, 10(1), pp.17-30.

Hasibuan, R.F., 2014. *Geologi dan studi distribusi rekahan pada batuan vulkanik kuartar Gunung Rajabasa dan sekitarnya, Kabupaten Lampung Selatan, Provinsi Lampung* (Undergraduate Thesis, Institute Technology of Bandung).

- Higgins, M.D., Voos, S. and Vander Auwera, J., 2015. Magmatic processes under Quizapu volcano, Chile, identified from geochemical and textural studies. *Contributions to Mineralogy and Petrology*, 170(5-6), p.51.
- Holland, T. and Blundy, J., 1994. Non-ideal interactions in calcic amphiboles and their bearing on amphibole-plagioclase thermometry. *Contributions to mineralogy and petrology*, 116(4), pp.433-447.
- Huchon, P. and Le Pichon, X., 1984. Sunda Strait and central Sumatra fault. *Geology*, 12(11), pp.668-672.
- Humphreys, M.C., Blundy, J.D. and Sparks, R.S.J., 2006. Magma evolution and open-system processes at Shiveluch Volcano: Insights from phenocryst zoning. *Journal of Petrology*, 47(12), pp.2303-2334.
- Innocenti, S., del Marmol, M.A., Voight, B., Andreastuti, S. and Furman, T., 2013. Textural and mineral chemistry constraints on evolution of Merapi Volcano, Indonesia. *Journal of Volcanology and Geothermal Research*, 261, pp.20-37.
- Itaya, T., Nagao, K., Inoue, K., Honjou, Y., Okada, T. and Ogata, A., 1991. Argon isotope analysis by a newly developed mass spectrometric system for K–Ar dating. *Mineralogical journal*, 15(5), pp.203-221.
- Jarrard, R.D., 1986. Terrane motion by strike-slip faulting of forearc slivers. *Geology*, 14(9), pp.780-783.
- Katili, J.A., 1975. Volcanism and plate tectonics in the Indonesian island arcs. *Tectonophysics*, 26(3-4), pp.165-188.
- Kusumasari, B.A., 2011. *Geologi Daerah Waymuli dan Sekitarnya Serta Geokimia Fluida Panas Bumi di Gunung Rajabasa, Kabupaten Lampung Selatan, Provinsi Lampung* (Undergraduate Thesis, Institute Technology of Bandung).

- Kopp, H., Flueh, E.R., Klaeschen, D., Bialas, J. and Reichert, C., 2001. Crustal structure of the central Sunda margin at the onset of oblique subduction. *Geophysical Journal International*, 147(2), pp.449-474.
- Le Bas, M., Maitre, R.L., Streckeisen, A., Zanettin, B. and IUGS Subcommittee on the Systematics of Igneous Rocks, 1986. A chemical classification of volcanic rocks based on the total alkali-silica diagram. *Journal of petrology*, 27(3), pp.745-750.
- Le Maitre, R.W., Bateman, P., Dudek, A., Keller, J., Lameyre, J., Le Bas, M.J., Sabine, P.A., Schmid, R., Sorensen, H., Streckeisen, A. and Woolley, A.R., 1989. A classification of igneous rocks and glossary of terms. Recommendations of the IUGS Subcommittee on the Systematics of Igneous rocks. *London: Blackwell Scientific Publications*.
- Longpré, M.A., Troll, V.R. and Hansteen, T.H., 2008. Upper mantle magma storage and transport under a Canarian shield-volcano, Teno, Tenerife (Spain). *Journal of Geophysical Research: Solid Earth*, 113(B8).
- Malod, J.A. and Kemal, B.M., 1996. The Sumatra margin: oblique subduction and lateral displacement of the accretionary prism. *Geological Society, London, Special Publications*, 106(1), pp.19-28.
- Malod, J.A., Karta, K., Beslier, M.O. and Zen Jr, M.T., 1995. From normal to oblique subduction: Tectonic relationships between Java and Sumatra. *Journal of Southeast Asian Earth Sciences*, 12(1-2), pp.85-93.
- Mandeville, C.W., Carey, S. and Sigurdsson, H., 1996. Magma mixing, fractional crystallization and volatile degassing during the 1883 eruption of Krakatau volcano, Indonesia. *Journal of Volcanology and Geothermal Research*, 74(3-4), pp.243-274.
- McCaffrey, R., 1991. Slip vectors and stretching of the Sumatran fore arc. *Geology*, 19(9), pp.881-884.

- Métrich, N., Vidal, C.M., Komorowski, J.C., Pratomo, I., Michel, A., Kartadinata, N., Prambada, O., Rachmat, H. and Surono, 2017. New Insights into Magma Differentiation and Storage in Holocene Crustal Reservoirs of the Lesser Sunda Arc: the Rinjani–Samalas Volcanic Complex (Lombok, Indonesia). *Journal of Petrology*, 58(11), pp.2257-2284.
- Miyashiro, A., 1974. Volcanic rock series in island arcs and active continental margins. *American journal of science*, 274(4), pp.321-355.
- Morse, S.A., 1984. Cation diffusion in plagioclase feldspar. *Science*, 225(4661), pp.504-505.
- Nagao, K. and Itaya, T., 1988. K-Ar age determination. *Memoir of Geological Society of Japan*, 29, pp.5-21.
- Nagao, K., Nishido, H., Itaya, T. and Ogata, K., 1984. An age determination by K-Ar method. *Bulletin of the Hiruzen Research Institute, Okayama University of Science*, 9, pp.19-38.
- Nakamura, M. and Shimakita, S., 1998. Dissolution origin and syn-entrapment compositional change of melt inclusion in plagioclase. *Earth and Planetary Science Letters*, 161(1-4), pp.119-133.
- Nazarwin., 1994. *Laporan Pemantauan Gunung Api Rajabasa dan Tinjauan Aspek-Aspek Geologinya di Daerah Kabupaten Lampung Selatan, Propinsi Lampung*, Kantor Wilayah Departemen Pertambangan dan Energi Provinsi Sumatra Selatan, Palembang.
- Neave, D.A. and Putirka, K.D., 2017. A new clinopyroxene-liquid barometer, and implications for magma storage pressures under Icelandic rift zones. *American Mineralogist*, 102(4), pp.777-794.

- Nelson, S.T. and Montana, A., 1992. Sieve-textured plagioclase in volcanic rocks produced by rapid decompression. *American Mineralogist*, 77(11-12), pp.1242-1249.
- Newhall, C.G., 1979. Temporal variation in the lavas of Mayon Volcano, Philippines. *Journal of Volcanology and Geothermal Research*, 6(1-2), pp.61-83.
- Nier, A.O., 1950. A redetermination of the relative abundances of the isotopes of carbon, nitrogen, oxygen, argon, and potassium. *Physical Review*, 77(6), pp.789-793.
- Ninkovich, D., 1976. Late Cenozoic clockwise rotation of Sumatra. *Earth and Planetary Science Letters*, 29(2), pp.269-275.
- Nishimura, S., 1980. Geological survey around Krakatau, Indonesia (1). *Tsukumo Earth Science, Kyoto Univ*, 15, pp.1-10.
- Nishimura, S., Abe, E., Nishida, J.I., Yokoyama, T., Dharma, A., Hehanussa, P. and Hehuwat, F., 1984. A gravity and volcanostratigraphic interpretation of the Lake Toba region, North Sumatra, Indonesia. *Tectonophysics*, 109(3-4), pp.253-272.
- Nishimura, S., Nishida, J.I., Yokoyama, T. and Hehuwat, F., 1986. Neo-tectonics of the Strait of Sunda, Indonesia. *Journal of Southeast Asian earth sciences*, 1(2), pp.81-91.
- Norini, G., GropPELLI, G., Capra, L. and De Beni, E., 2004. Morphological analysis of Nevado de Toluca volcano (Mexico): new insights into the structure and evolution of an andesitic to dacitic stratovolcano. *Geomorphology*, 62(1-2), pp.47-61.
- Pe-Piper, G., Piper, D.J. and Perissoratis, C., 2005. Neotectonics and the Kos Plateau Tuff eruption of 161 ka, South Aegean arc. *Journal of Volcanology and Geothermal Research*, 139(3-4), pp.315-338.
- Piper, D.J.W. and Perissoratis, C., 2003. Quaternary neotectonics of the South Aegean arc. *Marine Geology*, 198(3-4), pp.259-288.

- Prosser, J.T. and Carr, M.J., 1987. Poás volcano, Costa Rica: geology of the summit region and spatial and temporal variations among the most recent lavas. *Journal of volcanology and geothermal research*, 33(1-3), pp.131-146.
- Putirka, K.D., Perfit, M., Ryerson, F.J. and Jackson, M.G., 2007. Ambient and excess mantle temperatures, olivine thermometry, and active vs. passive upwelling. *Chemical Geology*, 241(3-4), pp.177-206.
- Putirka, K.D., 2008. Thermometers and barometers for volcanic systems. *Reviews in mineralogy and geochemistry*, 69(1), pp.61-120.
- Reubi, O. and Nicholls, I.A., 2004. Variability in eruptive dynamics associated with caldera collapse: an example from two successive eruptions at Batur volcanic field, Bali, Indonesia. *Bulletin of volcanology*, 66(2), pp.134-148.
- Steiger, R. and Jäger, E., 1977. Subcommittee on geochronology: convention on the use of decay constants in geo- and cosmochemistry. *Earth and planetary science letters*, 36(3), pp.359-362.
- Susilohadi, S., Gaedicke, C. and Djajadihardja, Y., 2009. Structures and sedimentary deposition in the Sunda Strait, Indonesia. *Tectonophysics*, 467(1-4), pp.55-71.
- Suswati, Haerani, N. and Sutawidjaja, I. S., 2001. Laporan Pemetaan Geologi Gunung Api Rajabasa, Lampung. *Pusat Vulkanologi dan Mitigasi Bencana Geologi (PVMBG)*, no. 05-2517L, 72 (Unpublished).
- Takahashi, E., 1986. Melting of a dry peridotite KLB-1 up to 14 GPa: Implications on the origin of peridotitic upper mantle. *Journal of Geophysical Research: Solid Earth*, 91(B9), pp.9367-9382.
- Takahashi, R. and Nakagawa, M., 2015. Evolution and eruption processes of a highly porphyritic silicic magma system: Petrology of the historical eruptive stage of Hokkaido-Komagatake Volcano, Japan. *Journal of Petrology*, 56(6), pp.1089-1112.

- Toya, N., Ban, M. and Shinjo, R., 2005. Petrology of Aoso volcano, northeast Japan arc: temporal variation of the magma feeding system and nature of low-K amphibole andesite in the Aoso-Osore volcanic zone. *Contributions to Mineralogy and Petrology*, 148(5), pp.566-581.
- Tsuchiyama, A., 1985. Dissolution kinetics of plagioclase in the melt of the system diopside-albite-anorthite, and origin of dusty plagioclase in andesites. *Contributions to Mineralogy and Petrology*, 89(1), pp.1-16.
- Tsukui, M., 1985. Temporal variation in chemical composition of phenocrysts and magmatic temperature at Daisen volcano, southwest Japan. *Journal of volcanology and geothermal research*, 26(3-4), pp.317-336.
- Van Bemmelen, R.W., 1949. The Geology of Indonesia, Government Printing Office. *Nijhoff, The Hague*.
- Villemant, B., Trigila, R. and DeVivo, B., 1993. Geochemistry of Vesuvius volcanics during 1631–1944 period. *Journal of Volcanology and Geothermal Research*, 58(1-4), pp.291-313.
- Waters, L.E. and Lange, R.A., 2015. An updated calibration of the plagioclase-liquid hygrometer-thermometer applicable to basalts through rhyolites. *American Mineralogist*, 100(10), pp.2172-2184.
- Wibowo, H.E., 2017. *Petrological and Geochemical Study of Sundoro Volcano, Central Java, Indonesia: Temporal Variation in Differentiation and Source Processes in the Growth of an Individual Volcano* (Doctoral dissertation, Hokkaido University).
- Widiyantoro, S. and van der Hilst, R., 1996. Structure and evolution of lithospheric slab beneath the Sunda arc, Indonesia. *Science*, 271(5255), pp.1566-1570.
- Widiyantoro, S. and van der Hilst, R., 1997. Mantle structure beneath Indonesia inferred from high-resolution tomographic imaging. *Geophysical Journal International*, 130(1), pp.167-182.

Yagi, K., 2006. Manual of mineral separation for K–Ar age dating. *Engineering Geology of Japan, 0,*” *The special issue of 10th anniversary of Hiruzen Institute for Geology and Chronology*”, pp.19-25

APPENDICES

APPENDICES

Appendix A. Location and description of samples

Table A.1 Tangkil and Rajabasa volcanic rocks

Table A.2 Krakatau and Sebesi volcanic rocks

Appendix B. K-Ar dating results

Table B.1 Result of potassium analysis

Table B.2 Result of K-Ar dating

Appendix C. Whole-rock chemistry (major and trace element) data

Table C.1 Tangkil and Rajabasa volcanic rocks

Table C.2 Krakatau and Sebesi volcanic rocks

Appendix D. Mineral chemistry

Table D.1 Tangkil mineral data

Table D.2 Rajabasa mineral data

Appendix E. MELTS calculation